



Cite this: *J. Mater. Chem. A*, 2021, 9, 19317

## Layered electrode materials for non-aqueous multivalent metal batteries

Ahiud Morag  and Minghao Yu \*

The global transition to clean energy production accelerates the necessity for efficient energy storage solutions. Lithium-ion batteries (LIBs), developed considerably over the past three decades, have been widely applied in portable electronics and electric vehicles. Nevertheless, the application of LIBs in large-scale energy storage applications is restricted by the Li resource scarcity, high-cost raw materials, and severe safety issues, which thus triggers the development of new battery chemistries beyond  $\text{Li}^+$ . In this regard, multivalent metal batteries (MVMBs, e.g., Zn, Mg, and Al batteries) are promising alternatives owing to the advantages brought by the direct use of corresponding metals as anodes, such as high elemental abundance, low anode redox potential, multielectron redox capability, and facile metal stripping and plating chemistry. However, MVMBs suffer from the lack of available cathodes for efficiently accommodating multivalent metal ions (i.e.,  $\text{Zn}^{2+}$ ,  $\text{Mg}^{2+}$ , and  $\text{Al}^{3+}$ ), which originates from the strong electrostatic interactions between charge carrier ions and cathodes. Promising cathode candidates for MVMBs to address this challenge are layered electrode materials, whose structures can be engineered with versatile approaches to regulate the charge-storage behaviour. Here, layered electrode materials used for non-aqueous MVMB cathodes are thoroughly reviewed. We first introduce the cell configurations and the thus-far developed anode–electrolyte–cathode chemistries for non-aqueous MVMBs. Recent progress in the exploration of layered materials for non-aqueous MVMBs is subsequently summarized. Emphasis is put on examining the employed structure engineering strategies and their effects on both the intrinsic properties and electrochemical behaviours of layered electrode materials. Finally, perspectives on the challenges and future directions in this research field are provided with aspects to the cathode structure engineering, performance assessment, and device demonstration.

Received 6th May 2021  
Accepted 9th July 2021

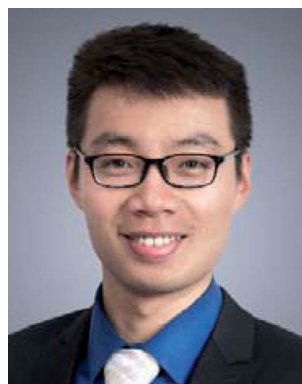
DOI: 10.1039/d1ta03842g

rsc.li/materials-a

Center for Advancing Electronics Dresden (cfaed) & Faculty of Chemistry and Food Chemistry, Technische Universität Dresden, Mommsenstrasse 4, 01062 Dresden, Germany. E-mail: minghao.yu@tu-dresden.de



Ahiud Morag received his PhD degree in interdisciplinary studies from Ben Gurion University of the Negev, Israel, in June 2019. In October 2019, he joined Prof Xinliang Feng's group at Technische Universität Dresden (TU Dresden) as a post-doctoral research associate. His research mainly focuses on the development of novel cathodes and electrolytes for non-aqueous magnesium and aluminum multivalent metal batteries.



Minghao Yu received his PhD degree in Material Physics and Chemistry from Sun Yat-sen University in June 2017. In March 2019, he became a research group leader of the Chair for Molecular Functional Materials at Technische Universität Dresden. His research interests focus on the development of advanced functional materials for applications of energy storage (supercapacitors and metal-ion batteries) and conversion (electrocatalysis and metal-air batteries).

### 1. Introduction

Global warming is pushing towards the transition from traditional fossil fuels to clean energy resources like solar, wind, and tidal energies.<sup>1,2</sup> However, the intermittent nature of these clean

and cheap energy resources restricts their direct utilization, which imposes a strong demand for high-performance energy storage technologies.<sup>3–5</sup> Among existing electrochemical energy storage technologies, lithium-ion batteries (LIBs) represent the most commercially successful one, and they have been implemented in diverse applications, such as portable electronics and electric vehicles.<sup>6,7</sup> However, the severe safety issues of LIBs, limited Li resource in the earth crust (20 ppm, 0.002%), and the increasing demand for cheap energy storage solutions motivate the development of new battery chemistries relying on cheap and abundant elements. In this context, multivalent metal batteries (MVMBs) are proposed as promising alternatives, which directly employ resource-abundant and low-cost multivalent metals (*e.g.*, Zn, Mg, and Al) as anodes.<sup>8–16</sup> Typically, multivalent metal anodes present low stripping/plating potentials (−0.76, −2.37, and −1.66 V *vs.* standard hydrogen electrode (SHE) for Zn, Mg, and Al, respectively), which are beneficial for the construction of high-voltage and high-energy storage devices (Fig. 1). Importantly, Zn, Mg, and Al are the 24th, 8th, and 3rd most abundant elements in the Earth's crust, respectively. These metal anodes can deliver high specific capacities due to their multielectron redox capability (820, 2206, and 2981 mA h g<sup>−1</sup> for Zn, Mg, and Al, respectively). Meanwhile, the high mass densities of multivalent metals empower the corresponding anodes with impressive volumetric capacities (5849, 3834, and 8047 Ah L<sup>−1</sup> for Zn, Mg, and Al, respectively). Interestingly, the partial compatibility of multivalent metals (especially Zn) with water-based electrolytes inspired researchers to develop aqueous MVMBs. Aqueous electrolytes enable the fabrication of low-cost and safe MVMBs with fast cation-storage kinetics of the cathodes.<sup>17,18</sup> However, aqueous MVMBs suffer from low voltage windows (normally less than 1.8 V) due to the narrow stable potential windows of water-based electrolytes. Moreover, water in electrolytes would lead to the formation of passivation layers on metal anodes, which can inhibit the stripping/plating of Mg and Al and accelerate the dendrite growth of Zn. By contrast, multivalent metals show negligible passivation or dendrite growth in non-

aqueous electrolytes, providing the metal stripping/plating process with high coulombic efficiency.<sup>19–24</sup> Additionally, non-aqueous electrolyte displays substantially higher potential window than aqueous electrolytes, enabling the use of many cathode materials with high redox potentials. All these features allow non-aqueous MVMBs to be promising candidates to abreast with LIBs as leading energy storage technologies.

However, the construction of practical non-aqueous MVMBs is hindered by severe challenges induced by the multivalent metal ions as charge carriers for cathodes. Multivalent metal ions display large charge densities, resulting from the multivalent nature and the small ionic radii (0.74, 0.72, and 0.53 Å for Zn<sup>2+</sup>, Mg<sup>2+</sup>, and Al<sup>3+</sup> compared with 0.76 Å for Li<sup>+</sup>). It further leads to the strong electrostatic interactions between charge carrier ions and cathodes during the charge/discharge of non-aqueous MVMBs. Consequently, most well-recognized metal oxide cathodes for LIBs stand inappropriate for non-aqueous MVMB cathodes.<sup>25–31</sup> In this sense, cathode structures for non-aqueous MVMBs should be re-designed at the atomic level to enable facile Zn<sup>2+</sup>, Mg<sup>2+</sup>, and Al<sup>3+</sup> storage.

As promising cathode candidates for non-aqueous MVMBs, natural layered materials are a class of materials with strong atom bonding in the basal plane and weak van der Waals (vdW) interaction between layers. These materials are equipped with versatile physical, chemical, electronic properties, as well as broad structural diversity.<sup>32–35</sup> Particularly, layered materials are appealing for energy storage, as they exhibit some intrinsic advantages over non-layered materials. For example, compared with non-layered materials, layered materials depicted higher accessibility of exposed active sites, enabling higher specific capacities and better ion diffusion kinetics.<sup>36–38</sup> However, some layered materials suffer from phase transition during electrochemical processes and poor stability in the ambient environment.<sup>39</sup> Thus far, a variety of layered materials have been explored as cathodes for MVMBs, including layered transition metal oxides (TMOs),<sup>32,40</sup> transition metal dichalcogenides (TMDs),<sup>41–43</sup> graphite,<sup>44,45</sup> and two-dimensional (2D) covalent organic frameworks (COFs).<sup>46</sup> Pristine layered materials as non-aqueous MVMB cathodes generally exhibit limited electrochemical performance.<sup>47</sup> Importantly, the weak vdW interaction between the stacked layers enables layered materials with diverse possibilities for rational structure engineering, such as exfoliation into 2D nanoflakes, interlayer expansion with guest molecules, and hybrid structure construction (Fig. 2).<sup>48</sup> These structure engineering strategies are highly desired for layered materials to tailor their intrinsic properties (*e.g.*, electronic structure, conductivity, and redox capability) and electrochemical behaviours (*e.g.*, ion desolvation energy, solid-state ion diffusion kinetics, charge-storage mechanism) for multivalent metal ion storage.

In this review, the latest development of layered materials for non-aqueous MVMB cathodes is reviewed. We first summarize the typical configurations of non-aqueous MVMBs in terms of the developed electrolytes, typical anode–electrolyte–cathode chemistries, and possible charge carrier ions. Next, a comprehensive overview of state-of-the-art layered materials used for

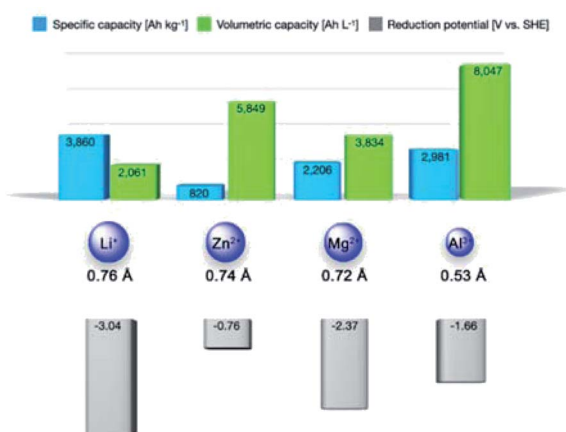


Fig. 1 Specific capacities, volumetric capacities, ionic radii, and stripping/plating potentials of various metal ions.



Fig. 2 Schematic illustration of the review content, including the cell configuration of non-aqueous MVMBs, layered cathode materials, and structure engineering methods.

non-aqueous MVMBs is carried out by emphasizing the strategies applied to tailor the structures of layered materials. Emphatic efforts are devoted to analysing the induced changes in the intrinsic properties and electrochemical behaviours of layered materials upon the structure regulation. Finally, perspectives on the current challenges and future directions of layered materials for non-aqueous MVMBs are presented.

## 2. Cell configurations of non-aqueous MVMBs

Contrasting to Li-metal anodes, Zn-, Mg-, and Al-metal anodes can be easily processed and show no aggressive dendrite growth in non-aqueous electrolytes during battery operation.<sup>49</sup> Although multivalent metals can be directly used as anodes, their stripping/plating reactions are not the simple  $M^{x+} + xe^- \rightarrow M$  reaction. Exact reaction mechanisms on multivalent metal anodes are introduced in this section. Additionally, according to the different cathode chemistry, non-aqueous MVMBs can be briefly categorized into cation ‘rocking-chair’ cells and dual-ion cells. In ‘rocking-chair’ cells, cation released from cathodes and metal plating on anodes occur during the charge of cells, while cation storage in cathodes and metal stripping on anodes occur during the discharge of cells. The electrolyte concentration in the ‘rocking-chair’ cells keeps constant during the cell operation. In dual-ion cells, anions serve as charge carrier ions for cathodes, which are stored/released in/from cathodes during the charge/discharge process of cells. The charge process would consume ions in electrolytes, and high-concentration or large amounts of electrolytes are preferred for dual-ion cells.<sup>50</sup> In this section, we also

discuss the cathode chemistries of MVMBs with a particular focus on the different charge carrier species.

### 2.1 Zn-metal batteries

The  $Zn^{2+}/Zn$  couple has a sufficiently high redox potential of  $-0.76$  V vs. SHE, which enables the Zn stripping/plating reaction to be feasible in either alkaline or close-to-neutral aqueous electrolytes. Moreover, the use of water-based electrolytes brings the advantages of low cost, high safety, high ionic conductivity, and easy-to-manufacture feature.<sup>51</sup> Thereby, dominant researches of Zn-metal batteries (ZMBs) are focused on aqueous systems. Aqueous ZMBs are not covered in this review, and interested readers are directed to recent comprehensive reviews of this field.<sup>52–57</sup> It is worth noting that aqueous ZMBs are restricted by several intrinsic drawbacks arising from the use of aqueous electrolytes. Cathode materials like  $MnO_2$  and  $VOPO_4$  suffer from dissolution in water, resulting in fast capacity degradation during cycling.<sup>58,59</sup> Additionally, Zn-metal anodes in aqueous electrolytes exhibit severe side reactions (e.g., hydrogen evolution, ZnO formation) and Zn dendrite growth, which further lead to the electrolyte decomposition, irreversible Zn consumption, low stripping/plating coulombic efficiency, and safety issues.<sup>60</sup>

Non-aqueous electrolytes based on ionic liquid, acetonitrile (AN) or carbonate solvents with Zn salts (e.g., zinc bis(trifluoromethylsulfonyl)imide ( $Zn(TFSI)_2$ ),  $Zn(CF_3SO_3)_2$  ( $Zn(OTf)_2$ ),  $Zn(ClO_4)_2$ ,  $Zn(BF_4)_2$ , and  $Zn(PF_6)_2$ ) were demonstrated feasible for reversible Zn stripping and plating.<sup>24,61–66</sup> These electrolytes offer much wider voltage windows than aqueous electrolytes. For example, Han *et al.*<sup>64</sup> showed that both AN and propylene carbonate (PC), dissolving different Zn salts (e.g.,  $Zn(TFSI)_2$ ,  $Zn(OTf)_2$ ,  $Zn(BF_4)_2$ , and  $Zn(PF_6)_2$ ), demonstrated high anodic stability of 3.8 V vs.  $Zn^{2+}/Zn$ . Wang *et al.*<sup>24</sup> developed a  $Li^+$ -containing hybrid electrolyte, exhibiting high anodic stability of 4 V vs.  $Zn^{2+}/Zn$ . The high anodic stability was achieved by adding  $LiPF_6$  to  $Zn(TFSI)_2$  in ethyl methyl carbonate (EMC). The wide voltage windows of non-aqueous Zn electrolytes are crucial for the fabrication of high-voltage and high-energy ZMBs.

According to the cathode chemistries, two possible charge storage mechanisms for non-aqueous ZMBs are presented in Fig. 3. The first one relies on the  $Zn^{2+}$  ‘rocking-chair’ mechanism. The high energy barrier of  $Zn^{2+}$  desolvation on the cathode surface accounts for the large charge-transfer resistance of these ZMBs.<sup>61,66,67</sup> The second mechanism is based on dual-ion cells, involving Zn plating/stripping on the anode and anion storage/release on the cathode. The charge-transfer resistance of anion storage is considerably lower than that of  $Zn^{2+}$  storage, enabling the excellent rate performance of ZMBs.<sup>24,68</sup> So far, several cathode materials with the  $Zn^{2+}$ -storage mechanism were reported for non-aqueous ZMBs, including  $MnO_2$ ,<sup>66</sup> vanadium oxide,<sup>61,65</sup> and  $VOPO_4$ .<sup>69</sup> On the other hand, graphite-based cathodes, exhibiting anion intercalation/deintercalation, were used for constructing dual-ion ZMBs.<sup>23,24,68</sup> Anions, such as  $PF_6^-$ ,  $TFSI^-$ , and  $OTf^-$  can be used as charge carriers for cathodes, providing ZMBs with high operation



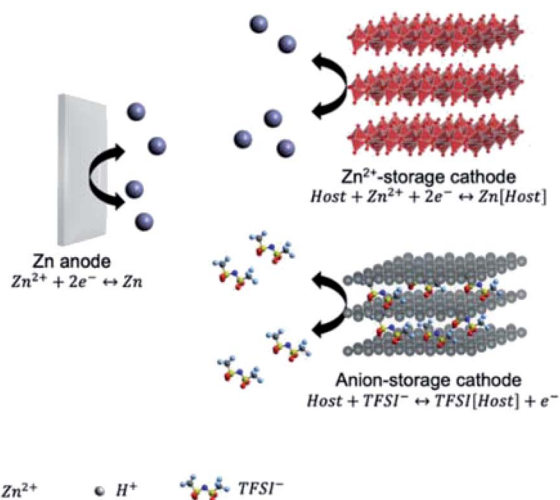


Fig. 3 Schematic illustration showing the charge storage mechanism of ZMBs.

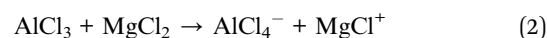
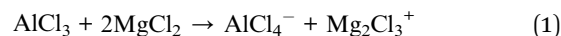
voltages and high energy densities. Overall, compared with aqueous ZMBs, non-aqueous ZMBs benefit from high anodic stability and dendrite-free Zn stripping and plating.

## 2.2 Mg-metal batteries

The Mg metal surface would be passivated in most solvents by an  $\text{Mg}^{2+}$  non-conducting layer, preventing the electrochemical Mg plating. In detail, electrolytes comprised of conventional solvents and Mg salts, such as  $\text{Mg}(\text{TFSI})_2$  or  $\text{Mg}(\text{ClO}_4)_2$  in AN or carbonate solvents, are not suitable for Mg-metal batteries (MMBs),<sup>70</sup> because these electrolytes tend to form ionic-insulating passivation layers (e.g.,  $\text{MgO}$ ,  $\text{MgCl}_2$ , and  $\text{Mg}_x\text{ClO}_y$ ) on Mg metal. Grignard reagents (e.g.,  $\text{EtMgBr}$ , and  $\text{Mg}(\text{BR}_4)_2$ , where R = butyl, phenyl) dissolved in ethers were presented as the first suitable electrolytes for the facile Mg stripping/plating.<sup>70–72</sup> However, Grignard reagent-based electrolytes show low anodic stability ( $<1.5$  V vs.  $\text{Mg}^{2+}/\text{Mg}$ ).<sup>72,73</sup> In 2000, Aurbach with his colleagues reported the MMB electrolyte,  $\text{Mg}(\text{AlCl}_2\text{-BuEt})_2$ , with high anodic stability.<sup>74</sup> The electrolyte was prepared by mixing  $\text{MgR}_2$  (R is butyl or ethyl) and  $\text{AlCl}_2\text{R}/\text{AlCl}_3$  in tetrahydrofuran (THF). The reaction between  $\text{RMgCl}$  and  $\text{R}_x\text{AlCl}_{3-x}$  produced  $\text{R}_x\text{AlCl}_{4-x}^-$  and active Mg-containing cations (e.g.,  $\text{MgCl}^+$  and  $\text{Mg}_2\text{Cl}_3^+$ ).<sup>75–78</sup> Importantly, the  $\text{Mg}(\text{AlCl}_2\text{BuEt})_2$  electrolyte exhibited a large electrochemical window of 2.5 V vs.  $\text{Mg}^{2+}/\text{Mg}$ , superior to electrolytes without the addition of  $\text{AlCl}_3$  (e.g.,  $\text{Mg}(\text{BPh}_2\text{Bu}_2)_2$  and  $\text{BuMgCl}$ ). Moreover, all phenyl complex (APC) electrolytes, the most commonly used electrolytes for MMBs, can be obtained by substituting the alkyl group of  $\text{RMgCl}$  with the phenyl group. These APC electrolytes can demonstrate wide stable potential windows of more than 3 V vs.  $\text{Mg}^{2+}/\text{Mg}$ .<sup>79</sup> Recent studies revealed that reducing the  $\text{R}_x\text{AlCl}_{4-x}^-$  concentration and increasing the  $\text{AlCl}_4^-$  concentration further improved the anodic stability of electrolytes. The low HOMO level of  $\text{AlCl}_4^-$  played an important role in improving the potential window. Zhao *et al.*<sup>80</sup> further improved the anodic stability of APC electrolytes by adding 1-butyl-1-

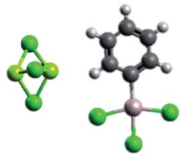
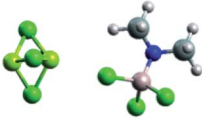
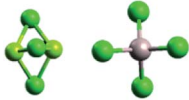
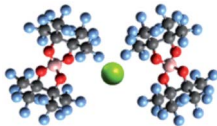
methylpiperidinium chloride ( $\text{PP}_{14}\text{Cl}$ ). The  $\text{Cl}^-$  ions reacted with  $\text{R}_x\text{AlCl}_{4-x}^-$  to produce  $\text{AlCl}_4^-$ , consequently increasing the anodic stability from 2.9 to 3.1 V vs.  $\text{Mg}^{2+}/\text{Mg}$ .

Magnesium aluminium chloride complex (MACC) dissolved in ether solvents (e.g., dimethoxyethane (DME)) represents an important type of MMB electrolytes with all-inorganic salts (e.g.,  $\text{AlCl}_3$  and  $\text{MgCl}_2$ ).<sup>81–83</sup> During the preparation of MACC electrolytes, different acid–base reactions occur depending on the ratio between  $\text{AlCl}_3$  and  $\text{MgCl}_2$ . For  $\text{MgCl}_2$  :  $\text{AlCl}_3$  ratio of 2 : 1 and 1 : 1, the dominating  $\text{Mg}_x\text{Cl}_y^{2x-y}$  species in the electrolyte are  $\text{Mg}_2\text{Cl}_3^+$  and  $\text{MgCl}^+$  through eqn (1) and (2). In these cases, Mg undergoes facile electrochemical stripping and plating due to the presence of  $\text{Mg}_x\text{Cl}_y^{2x-y}$  species. Increasing the  $\text{MgCl}_2$  :  $\text{AlCl}_3$  ratio to 1 : 2 inhibits Mg plating due to the low concentration of  $\text{Mg}_x\text{Cl}_y^{2x-y}$  species.<sup>82</sup> Moreover, when the  $\text{AlCl}_3$  :  $\text{MgCl}_2$  ratio is higher than 2 : 1, the formation of  $\text{AlCl}_2^+$  would cause severe Mg metal corrosion.<sup>84</sup> Typical MACC electrolytes require the pre-cycling process to reduce the overpotential and improve the electrochemical stripping/plating coulombic efficiency.<sup>85</sup> The pre-cycling process is termed conditioning, and would complicate the production of MMBs. Conditioning-free MACC electrolytes can be obtained by adding additional salts like  $\text{Mg}(\text{TFSI})_2$  and  $\text{Mg}(\text{hexamethyldisilazide})_2$  ( $\text{Mg}(\text{HMDS})_2$ ).<sup>84,86</sup> Besides, these Mg-salt additives can improve the water-resistance of MACC electrolytes, allowing excellent Mg plating at a water content of 2000 ppm. Electrochemical Mg plating is also feasible by completely replacing  $\text{AlCl}_3$  in MACC electrolytes with either  $\text{Mg}(\text{TFSI})_2$  or  $\text{Mg}(\text{HMDS})_2$ .<sup>87,88</sup> In the  $\text{MgCl}_2/\text{Mg}(\text{TFSI})_2$  electrolyte, salts and solvents must have high purity by removing water residue to realize the facile Mg stripping and plating. By contrast, purification is not necessary for the  $\text{Mg}(\text{HMDS})_2/\text{MgCl}_2$  electrolyte to achieve reversible Mg stripping and plating.



Chloride presence in MMB electrolytes accounts for the corrosive nature of electrolytes for common current collectors (e.g., Al and stainless steel), thus encouraging the development of chlorine-free Mg electrolytes. Mohtadi *et al.*<sup>90</sup> presented a chlorine-free electrolyte based on  $\text{Mg}(\text{BH}_4)_2$  in DME. Nevertheless, the electrolyte displayed low coulombic efficiency (67%), and the decomposition of  $\text{BH}_4^-$  lead to the low anodic stability (2.3 V vs.  $\text{Mg}^{2+}/\text{Mg}$ ) of the electrolyte. Inspired by Mohtadi's work, Tutusaus and co-workers<sup>91</sup> reported a halogen-free electrolyte with dodecaborate dianions for successful Mg stripping and plating. Impressively, the electrolyte demonstrated outstanding anodic stability of 3.8 V vs.  $\text{Mg}^{2+}/\text{Mg}$ .<sup>91</sup> Following this strategy, Luo *et al.*<sup>89</sup> synthesized Mg perfluorinated pinacolatoborate (FPB) for MMB electrolytes, which depicted outstanding anodic stability of 4.0 V vs.  $\text{Mg}^{2+}/\text{Mg}$ . However, it should be pointed out that the synthesis of boron-based Mg salts generally requires harsh conditions under inert environments. Complicated synthetic routes impose a potential risk for the practical application of these boron-

Table 1 Comparison of developed MMB electrolytes

Electrolyte name	APC <sup>79</sup>	Mg-HMDS <sup>88</sup>	MACC <sup>81,82</sup>	Mg(BR <sub>n</sub> ) <sub>2</sub> (ref. 89)
Main precursors	PhMgCl, AlCl <sub>3</sub>	Mg(HMDS) <sub>2</sub> , MgCl <sub>2</sub>	MgCl <sub>2</sub> , AlCl <sub>3</sub>	Mg(BH <sub>4</sub> ) <sub>2</sub> , C <sub>6</sub> H <sub>2</sub> F <sub>12</sub> O <sub>2</sub>
Cations and anions	 Mg <sub>x</sub> Cl <sub>y</sub> <sup>+</sup> and Ph <sub>x</sub> AlCl <sub>4-x</sub> <sup>-</sup>	 Mg <sub>2</sub> Cl <sub>3</sub> <sup>+</sup> and HMDSAAlCl <sub>3</sub> <sup>-</sup>	 Mg <sub>2</sub> Cl <sub>3</sub> <sup>+</sup> and AlCl <sub>4</sub> <sup>-</sup>	 Mg <sup>2+</sup> and B(O <sub>2</sub> C <sub>2</sub> (CF <sub>3</sub> ) <sub>4</sub> ) <sub>2</sub> <sup>-</sup>
Anodic stability	2.5 V vs. Mg <sup>2+</sup> /Mg	2.8 V vs. Mg <sup>2+</sup> /Mg	3.5 V vs. Mg <sup>2+</sup> /Mg	4.0 V vs. Mg <sup>2+</sup> /Mg
Coulombic efficiency	~100%	99%	99%	95%
Advantages	High coulombic efficiency	Good cathode compatibility	Simple synthesis, high concentration	High anodic stability
Drawbacks	Low anodic stability	Low anodic stability	Conditioning required	Complicated synthetic process

based electrolytes. A summary of the main features of developed Mg electrolytes is presented in Table 1.

With the demonstrated anode–electrolyte chemistries, searching compatible cathodes represents the main task to establish suitable full-device chemistries. The large charge density of Mg<sup>2+</sup> and its strong binding to Cl<sup>-</sup> and solvent molecules rule out many recognized cathode materials in other battery systems. The first demonstrated MMB cathode with decent performance is the Chevrel-phase Mo<sub>6</sub>S<sub>8</sub>.<sup>74</sup> Theoretical studies suggest that the Chevrel phase surface can significantly accelerate the desolvation and dissociation of Mg<sub>2</sub>Cl<sub>3</sub><sup>+</sup> in THF, reducing the dissociation energy of Mg<sub>2</sub>Cl<sub>3</sub><sup>+</sup> from 3.0 eV to 0.2 eV.<sup>92</sup> For this reason, the Chevrel phase is one of a few inorganic materials that can be used as cathodes of MMBs without structure modification or special conditions (*e.g.*, elevated temperature).

Besides, TMOs are considered promising materials for energy storage due to their high theoretical capacities and operation potentials. Apart from classic Mg<sup>2+</sup> intercalation, TMO can also store charge through the conversion mechanism.

The charge storage mechanism is determined by the type of TMOs and the nature of electrolytes.<sup>93–95</sup> However, TMO cathodes for MMBs suffer from large voltage hysteresis and sluggish intercalation kinetics. These issues can be assigned to the strong electrostatic interactions between O atoms in TMOs and Mg<sup>2+</sup>.<sup>96</sup> In addition, the compatibility of TMOs with chloride-containing electrolytes is poor, making the fabrication of MMBs with TMO cathodes a great challenge.<sup>94</sup> Another class of MMB cathodes is TMDs, which display better Mg<sup>2+</sup>-intercalation kinetics than TMOs in light of the weak electrostatic interactions between chalcogenide atoms and Mg<sup>2+</sup>. Unlike TMOs, TMDs are compatible with chloride-containing electrolytes. However, the main issue associated with TMDs is their much lower theoretical capacities and redox potentials than those of TMOs. The charge storage mechanism was shown to be either intercalation reaction or intercalation/conversion reaction with Mg<sup>2+</sup>, MgCl<sup>+</sup>, or [Mg(DME)<sub>3</sub>]<sup>2+</sup> as charge-carrier species (Fig. 4).

### 2.3 Al-metal batteries

Trivalent Al<sup>3+</sup> and the high abundance of Al resources make Al-metal batteries (AMBs) to be promising candidates for large-scale energy storage. However, electrochemical Al stripping and plating is challenging in both organic and ionic liquid electrolytes. The large charge density of Al<sup>3+</sup> induces the strong coulombic anion–cation interactions in Al salts (*e.g.*, Al(TFSI)<sub>3</sub> and Al(OTf)<sub>3</sub>), which further results in the low solubility of Al salts in common carbonate solvents. On the other hand, although ether-based solvents (*e.g.*, DME and diglyme) can dissolve Al salts, these solvents exhibit strong interactions with cations, leading to high solvation energies.<sup>97,98</sup> To achieve facile Al stripping/plating, the commonly used chemistry takes use of Al<sub>2</sub>X<sub>7</sub><sup>-</sup> (X is Cl or Br), as shown in eqn (3).<sup>99–102</sup> The Al plating chemistry was first discovered in high-temperature (140–180 °C) molten salts, such as AlCl<sub>3</sub>–LiCl and AlCl<sub>3</sub>–NaCl–KCl.<sup>100,101</sup> However, the requirement of high temperature would greatly restrict the practical application of AMBs in energy storage

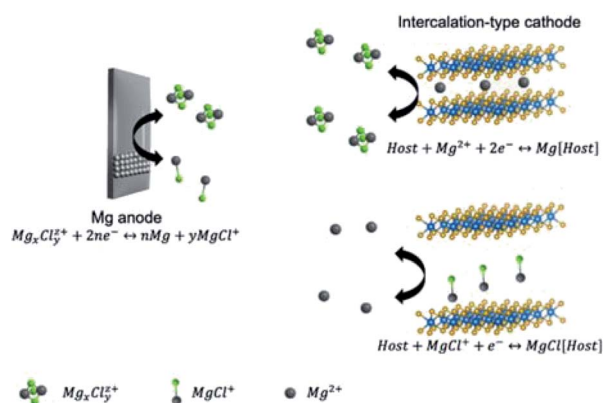
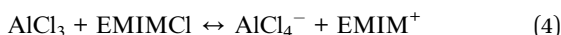
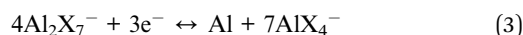
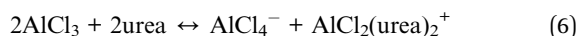


Fig. 4 Schematic illustration showing the charge storage mechanism of MMBs.

devices. To this end, room-temperature ionic liquids with low viscosity are employed for AMBs. The most commonly used ionic liquids are mixtures of  $\text{AlCl}_3$  and 1-ethyl-3-methylimidazolium chloride (EMIMCl). To achieve Al plating, the  $\text{AlCl}_3$  : EMIMCl molar ratio should be higher than 1 to ensure the presence of  $\text{Al}_2\text{Cl}_7^-$  through the reactions of eqn (4) and (5). The standard reduction potential of  $\text{Al}_2\text{Cl}_7^-$  is  $-0.7$  V vs. SHE (eqn (3)), which is almost 1.0 V higher than the direct reduction of  $\text{Al}^{3+}$  ( $-1.66$  V vs. SHE).<sup>103</sup>



Besides, mixtures of  $\text{AlCl}_3$  with amides (e.g., urea and acetamide) can serve as economical alternatives for ionic liquid-based electrolytes.<sup>104,105</sup> In these cases,  $\text{AlCl}_4^-$ ,  $\text{Al}_2\text{Cl}_7^-$ , and  $\text{AlCl}_2^+$  are formed through the reactions in eqn (5) and (6). Thermodynamically, Al plating can also be achieved through the reduction of  $\text{AlCl}_2^+$ . However, calculations showed that the large energy barrier associated with the dissociation of Al-amide bonds restricted this reaction (Fig. 5).<sup>104</sup> This fact could explain why electrochemical Al stripping/plating occurs only with the presence of  $\text{Al}_2\text{Cl}_7^-$ . While amide/ $\text{AlCl}_3$ -based electrolytes are appealing for replacing ionic liquid-based electrolytes from a cost perspective, they suffer from high viscosity and low ionic conductivity. These drawbacks result in the inferior performance of AMBs with amide/ $\text{AlCl}_3$  electrolytes, compared with AMBs with EMIMCl/ $\text{AlCl}_3$  electrolytes.<sup>105</sup>



Intercalation of large-charge-density  $\text{Al}^{3+}$  usually leads AMB cathodes to poor cyclability and low-rate capability. For example, inorganic cathode materials (e.g.,  $\text{TiO}_2$ ,<sup>29</sup>  $\text{TiS}_2$ ,<sup>106</sup>  $\text{Co}_9\text{S}_8$ ,<sup>107</sup> and  $\text{V}_2\text{O}_5$  (ref. 108)), with charge storage involving  $\text{Al}^{3+}$ , demonstrate significant capacity fading during the first few cycles. In addition to the sluggish  $\text{Al}^{3+}$  intercalation, the high dissociation energy of  $\text{Al}_2\text{Cl}_7^-$  to  $\text{Al}^{3+}$  (eqn (7)) is another important reason for the low rate capability and large charge/discharge voltage hysteresis of AMBs with  $\text{Al}^{3+}$  storage. Recently, Yang *et al.*<sup>109</sup> reported that the dissociation rate of  $\text{Al}_2\text{Cl}_6\text{Br}^-$ , prepared by mixing  $\text{AlCl}_3$  with EMIMBr, was 15-fold

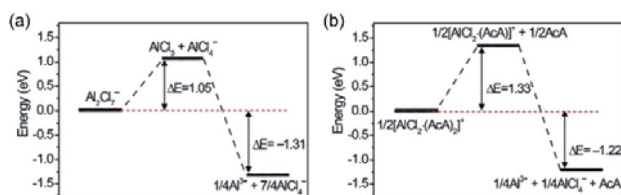


Fig. 5 Energy profiles of the dissociation reactions of (a)  $\text{Al}_2\text{Cl}_7^-$  and (b)  $[\text{AlCl}_2(\text{acetamide})_2]^+$ . Reprinted with permission from ref. 104. Copyright 2018 Elsevier.

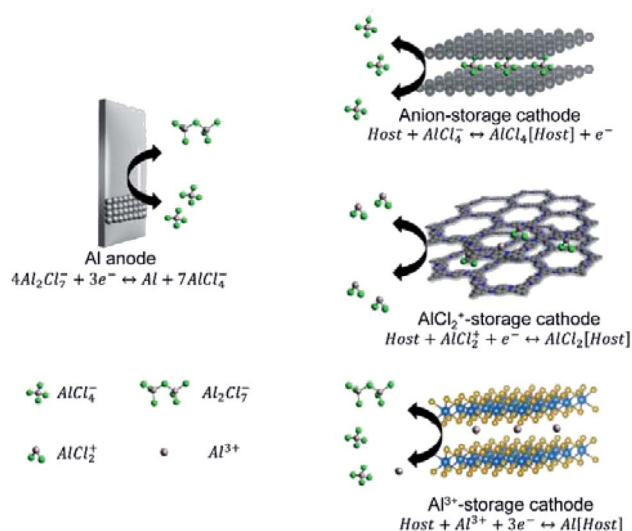
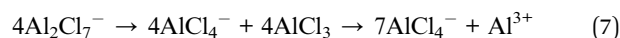


Fig. 6 Schematic illustration showing the charge storage mechanism of AMBs.

faster than that of  $\text{Al}_2\text{Cl}_7^-$ . However, the voltage window of this  $\text{Al}_2\text{Cl}_6\text{Br}^-$ -based electrolyte exhibited a narrow potential window, which was only suitable for low-potential cathodes, such as  $\text{TiS}_2$  (ref. 106) and  $\text{TiO}_2$ .<sup>29</sup> Other Al-based species, such as  $\text{AlCl}_2^+$  and  $\text{AlCl}_4^-$ , generally act as favourable charge carriers for AMB cathodes (Fig. 6).<sup>21,110,111</sup> In detail,  $\text{AlCl}_4^-$  can serve as the charge carrier for graphite and amine compounds.<sup>21,112,113</sup> On the other hand, n-type organic electrodes (e.g., pyrazine,<sup>114</sup> polyaniline,<sup>115</sup> and phenanthrenequinone<sup>110</sup>) can store charges through redox reactions with  $\text{AlCl}_2^+$ . Compared with  $\text{Al}^{3+}$ ,  $\text{AlCl}_2^+$  as the charge carrier allows cathodes with higher charge/discharge rates and better cyclability. The intercalation of  $\text{Al}^{3+}$  was disclosed to be challenging in most materials, pushing towards the development of new n-type and p-type organic materials for  $\text{AlCl}_2^+/\text{AlCl}_4^-$  storage.



### 3. Layered cathode materials for MVMBs

Layered materials present 2D topologies with flat planes, forming a bulk structure through the weak vdW interaction. They have been widely used for both cation and anion storage due to their potentially high theoretical capacities and favourable 2D ion transport channels.<sup>41,44,46</sup> Specifically, efficient cation/anion storage in layered materials can be promoted by large interlayer spacing, weak interactions between intercalating ions and host lattices, and the electronic conductivity of layered materials.<sup>116,117</sup> Therefore, both intrinsic properties of layered materials and the applied structure modification have a prominent effect on the charge storage capability. In this section, we present the current state-of-the-art layered cathode materials used for non-aqueous MVMBs. The materials in this section are divided into four major groups, layered TMOs,

TMDs, graphite-based materials, and 2D COFs. We analyse the proposed structure modification approaches and their influence on both the intrinsic physicochemical properties and the electrochemical performance enhancement of layered materials.

### 3.1 Layered transition metal oxides

TMOs include a broad class of materials with diverse structural frameworks, which exhibit excellent stability, environmental friendliness, and simple synthetic routes.<sup>117–120</sup> The multiple valence states of transition metal elements arise from the coordination of the transition metal with highly electronegative oxygen, empowering TMOs with the superior charge storage capability (e.g., superior specific capacity). In addition, the high ionic feature of M–O bonds results in relatively high electrochemical redox potentials.<sup>37</sup> However, the oxygen atoms of TMOs impose strong interactions with charge carrier ions (e.g., Zn<sup>2+</sup>, Mg<sup>2+</sup>, and Al<sup>3+</sup>), which leads to the limited ion-storage kinetics and poor structural stability of TMOs used in MVMBs.<sup>25,121</sup> In this sense, layered TMOs allow solid-state ion diffusion through the 2D interlayer space, providing efficient ion transport pathways.<sup>122</sup> Furthermore, structure modification of layered TMOs aims at weakening the interaction between intercalating ions and oxygen atoms. So far, several layered TMOs have been explored for MVMB cathodes, including manganese oxide, vanadium oxide, and vanadyl phosphate (VOPO<sub>4</sub>).

**3.1.1 Manganese oxides.** Manganese oxides have two layer-structure phases, namely,  $\epsilon$ - and  $\delta$ -phase MnO<sub>2</sub>. The  $\delta$ -phase MnO<sub>2</sub> (birnessite) is believed to provide more efficient pathways for cation diffusion than the  $\epsilon$ -phase MnO<sub>2</sub>.<sup>123</sup> Both MnO<sub>2</sub> phases are composed of Mn<sup>4+</sup> ions surrounded by six oxygen atoms, creating [MnO<sub>6</sub>] octahedral units. The [MnO<sub>6</sub>] units are linked *via* edge corners to form the layer structure.<sup>124–127</sup> Birnessite MnO<sub>2</sub> exhibits an interlayer distance of 7.24 Å, with a crystal water layer between two [MnO<sub>6</sub>] octahedral layers. It is promising battery cathode material in light of the high specific capacity (308 mA h g<sup>-1</sup> for Mn<sup>3+</sup>/Mn<sup>4+</sup> transition), nontoxicity, and low cost.

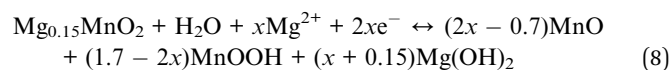
Due to the high specific capacity of MnO<sub>2</sub>,<sup>58</sup> extensive researches have been conducted to use MnO<sub>2</sub> as cathodes for aqueous ZMBs. Recently, Han *et al.*<sup>66</sup> studied the charge storage performance of the  $\delta$ -MnO<sub>2</sub> cathode using Zn(TFSI)<sub>2</sub> in AN as the electrolyte.  $\delta$ -MnO<sub>2</sub> was prepared by the reaction between KMnO<sub>4</sub> and MnSO<sub>4</sub>, displaying a nanofloret-like morphology with an interlayer spacing of 7 Å. The Zn<sup>2+</sup>-intercalation mechanism of  $\delta$ -MnO<sub>2</sub> nanoflorets was studied using *ex situ* X-ray diffraction (XRD) and scanning transmission electron microscopy energy dispersive X-ray spectroscopy (STEM-EDS). After the first discharge, the (001) and (002) peak intensity of  $\delta$ -MnO<sub>2</sub> was significantly decreased, indicating the loss of long-range order in the layer direction. This was caused by the structural transformation of  $\delta$ -MnO<sub>2</sub> to the non-layered polymorph. The structural change caused the specific capacity increase to 123 mA h g<sup>-1</sup> at 12.3 mA g<sup>-1</sup> during the first 20 cycles. After 30 cycles, the specific capacity started to decay,

reaching 55 mA h g<sup>-1</sup> after 125 cycles. The decrease was attributed to the severe electrolyte decomposition and the formation of the passivation layer on the anode.

MnO<sub>2</sub> was also studied as the cathodes of MMBs in light of its high redox potential *vs.* Mg<sup>2+</sup>/Mg. However, Mg<sup>2+</sup> intercalation into layered MnO<sub>2</sub> was not feasible with the electrolyte consisting of anhydrous Mg(ClO<sub>4</sub>)<sub>2</sub> in AN.<sup>128</sup> Therefore, the water-containing electrolyte was prepared using Mg(ClO<sub>4</sub>)<sub>2</sub>·xH<sub>2</sub>O with the H<sub>2</sub>O : Mg<sup>2+</sup> ratio of 6. After the addition of water, Mg<sup>2+</sup> intercalation was improved from a ratio of <0.2 Mg<sup>2+</sup> per Mn for anhydrous Mg(ClO<sub>4</sub>)<sub>2</sub> to a ratio of 0.7 Mg<sup>2+</sup> per Mn (Fig. 7a). Interestingly, cycling with the water-containing electrolyte acted as an activation step of MnO<sub>2</sub>. The activated MnO<sub>2</sub> maintained the good Mg<sup>2+</sup>-storage performance in the anhydrous electrolyte. The authors claimed that, during the discharge/charge cycling in the water-containing electrolyte, a slight structure re-orientation occurred, causing the activation of MnO<sub>2</sub>. However, due to the low crystallinity of the sample, the exact phase transition was not detected.

To further understand the role of water in MnO<sub>2</sub>, Sun *et al.*<sup>95</sup> investigated Mg<sup>2+</sup> intercalation into Mg<sub>0.15</sub>MnO<sub>2</sub>·0.9H<sub>2</sub>O (Fig. 7b). Using Karl Fischer titration, it was disclosed that water molecules in the Mg<sub>0.15</sub>MnO<sub>2</sub>·0.9H<sub>2</sub>O structure were removed during the first 20 cycles. Remarkably, the first 20 cycles were also the cycles required for the full conditioning of the Mg<sub>0.15</sub>MnO<sub>2</sub>·0.9H<sub>2</sub>O cathode (Fig. 7c and d). The activation was also necessary for the water-containing electrolyte, suggesting that the activation is related to the structural change of Mg<sub>0.15</sub>MnO<sub>2</sub>·0.9H<sub>2</sub>O. X-ray photoelectron spectroscopy (XPS) measurements detected the existence of MnOOH, MnO, and Mg(OH)<sub>2</sub> in the electrode at different charged states (Fig. 7e). In detail, the original electrode contained 77% Mn<sup>4+</sup>, 20% Mn<sup>3+</sup>, and 3% Mn<sup>2+</sup>, which was indicative of the chemical formula Mg<sub>0.15</sub>MnO<sub>2</sub>·0.9H<sub>2</sub>O. At the discharged state, peaks corresponding to MnOOH and MnO were observed. At the charged state, MnO was still detected, indicating that the electrochemical process was partially reversible. These results indicated that the magnesianation process of Mg<sub>0.15</sub>MnO<sub>2</sub>·0.9H<sub>2</sub>O was accompanied by the conversion reaction, as shown in eqn (8). Moreover, the small specific capacity of 135 mA h g<sup>-1</sup> after 20 cycles suggested that the electrochemical charge storage reaction was limited to the surface of Mg<sub>0.15</sub>MnO<sub>2</sub>·0.9H<sub>2</sub>O.

Overall, water molecules in the electrolyte or the crystal structure of MnO<sub>2</sub> play a vital role in promoting the initial intercalation of Mg<sup>2+</sup> into MnO<sub>2</sub>. After the pre-cycling in the water-containing electrolyte, MnO<sub>2</sub> undergoes structural changes, and the water-containing electrolyte can be replaced by the anhydrous electrolyte. Since Mg metal is not stable in the water environment, water removal is an important step for the full Mg//MnO<sub>2</sub> cell.



**3.1.2 Vanadium oxides.** Orthorhombic vanadium pentoxide (V<sub>2</sub>O<sub>5</sub>) is a typical layered material with an interlayer



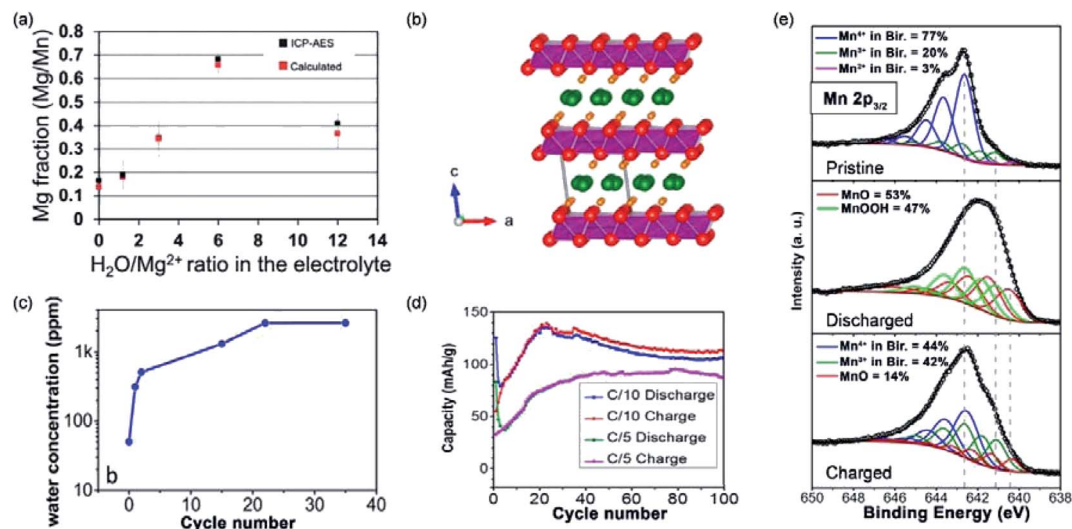


Fig. 7 (a) Inductively coupled plasma-atomic emission spectroscopy Mg : Mn ratios of  $\text{MnO}_2$  nanowire electrodes discharged at  $-0.4$  V vs. Ag/AgCl for 15 minutes in electrolytes with various  $\text{H}_2\text{O}/\text{Mg}^{2+}$  ratios and expected Mg : Mn ratios which were calculated based on the total accumulated charges. Error bars indicate 95% confidence intervals. Reproduced from ref. 128 with permission from the PCCP Owner Societies. (b) Birnessite crystal structure showing a water monolayer between the  $\text{MnO}_2$  sheets. (c) The water content of the electrolyte as determined by Karl Fischer titration, showing the full water release after 20 cycles. (d) Cycling performance of  $\text{MnO}_2 \cdot 0.9\text{H}_2\text{O}$  at C/10 and C/5. (e) Mn  $2p_{3/2}$  XPS spectra of the pristine, discharged, and charged Mg-birnessite/carbon cloth electrodes; fits are shown in colour as labelled. Reprinted with permission from ref. 95. Copyright 2016 American Chemical Society.

spacing of  $4.37 \text{ \AA}$ .<sup>129</sup> The layer is composed of  $[\text{VO}_5]$  pyramids connected *via* edge-sharing.  $[\text{VO}_5]$  pyramids show two types of bonds, namely, the  $\text{O}=\text{V}$  double bond and the  $\text{V}-\text{O}-\text{V}$  bond.<sup>130</sup> The  $\text{V}^{5+}/\text{V}^{4+}$  redox couple empowers  $\text{V}_2\text{O}_5$  with a high theoretical specific capacity of  $295 \text{ mA h g}^{-1}$ . In addition,  $\text{V}_2\text{O}_5$  displays a high redox potential of  $\sim 3.2$  V vs.  $\text{Li}^+/\text{Li}$ , making  $\text{V}_2\text{O}_5$  a promising cathode material for MVMB cathodes.<sup>131</sup>

Novák and Desilvestro,<sup>133</sup> for the first time, demonstrated the intercalation of  $\text{Mg}^{2+}$  into  $\text{V}_2\text{O}_5$  by adding water to the  $\text{Mg}(\text{ClO}_4)_2$  in AN electrolyte. The intercalation kinetics of  $\text{Mg}^{2+}$  was significantly improved through the shielding effect of water. Inspired by this study, several studies showed that the incorporation of water into the  $\text{V}_2\text{O}_5$  structure could attain a similar shielding effect. For example, An *et al.*<sup>132</sup> synthesized the  $\text{V}_2\text{O}_5 \cdot 1.4\text{H}_2\text{O}$  nanowire/graphene hybrid (denoted VOG), which presented greatly improved conductivity and  $\text{Mg}^{2+}$ -intercalation kinetics (Fig. 8a and b). VOG delivered a large specific capacity of  $330 \text{ mA h g}^{-1}$  at  $50 \text{ mA g}^{-1}$  and high capacity retention of 80% after 200 cycles. For comparison, VOG without crystal water was subsequently prepared *via* annealing. The annealed VOG exhibited a very limited  $\text{Mg}^{2+}$ -intercalation performance with a small specific capacity of  $<75 \text{ mA h g}^{-1}$  at  $100 \text{ mA g}^{-1}$  (Fig. 8c). Remarkably, XRD patterns showed only a small difference between the interlayer distance of VOG ( $11 \text{ \AA}$ ) and the annealed VOG ( $10 \text{ \AA}$ ). It implied that, compared with the expanded interlayer spacing, the shielding effect of water molecules played the dominant role in promoting the  $\text{Mg}^{2+}$ -storage kinetics (Fig. 8d). Significantly, water molecules were located at the interstitial sites of  $\text{V}_2\text{O}_5 \cdot 1.4\text{H}_2\text{O}$ , and kept confined within the  $\text{V}_2\text{O}_5$  lattice during charge/discharge, even at elevated temperatures.<sup>132,134</sup> It thereby explained the excellent

capacity retention of VOG over the prolonged cycling ( $100 \text{ mA h g}^{-1}$  after 200 cycles at  $1 \text{ A g}^{-1}$ ).

Metal atom incorporation into  $\text{V}_2\text{O}_5$  interlayers (*e.g.*, Mg, Mn, or Na)<sup>135–139</sup> represents another effective strategy to promote the stability of layered  $\text{V}_2\text{O}_5$ . For instance, Mg incorporation was achieved through electrochemically discharging  $\text{V}_2\text{O}_5$  nanowires to  $0.2$  V vs.  $\text{Mg}^{2+}/\text{Mg}$ .<sup>136</sup> Near edge X-ray absorption fine

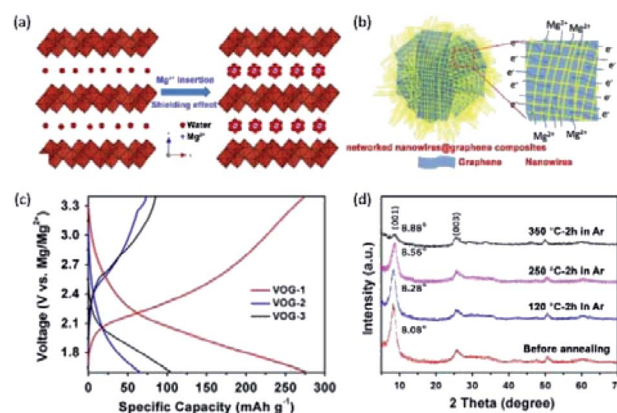


Fig. 8 (a) Shielding effect of water in  $\text{V}_2\text{O}_5 \cdot x\text{H}_2\text{O}$ . The strong polarization of divalent  $\text{Mg}^{2+}$  could be significantly reduced by solvating with crystal water molecules. (b) Schematic illustration of the  $\text{V}_2\text{O}_5 \cdot x\text{H}_2\text{O}$ /graphene nanocomposite with bi-continuous electron/ion transport pathways, large area of electrode–electrolyte interface, and facile strain relaxation during  $\text{Mg}^{2+}$  insertion/extraction. (c) Charge/discharge curves of hydrate  $\text{V}_2\text{O}_5 \cdot x\text{H}_2\text{O}$  (VOG-1),  $\text{V}_2\text{O}_5 \cdot x\text{H}_2\text{O}$  after heating in Ar (VOG-2) and in air (VOG-3) at  $350 \text{ }^\circ\text{C}$  for 2 h. (d) XRD spectra of  $\text{V}_2\text{O}_5 \cdot 1.35\text{H}_2\text{O}$  before and after annealing in Ar. Reprinted with permission from ref. 132. Copyright 2015 Elsevier.





Fig. 9 (a) Schematic showing the crystal structure of  $\text{Mg}_{0.3}\text{V}_2\text{O}_5 \cdot 1.1\text{H}_2\text{O}$ . (b) Charge–discharge curves of  $\text{Mg}_{0.3}\text{V}_2\text{O}_5 \cdot 1.1\text{H}_2\text{O}$ ,  $\text{V}_2\text{O}_5 \cdot x\text{H}_2\text{O}$ , and  $\text{Mg}_{0.3}\text{V}_2\text{O}_5$ . (c) Scanning electron microscope images of the  $\text{Mg}_{0.3}\text{V}_2\text{O}_5 \cdot 1.1\text{H}_2\text{O}$  single-nanowire devices. (d)  $I$ – $V$  curves of  $\text{Mg}_{0.3}\text{V}_2\text{O}_5 \cdot 1.1\text{H}_2\text{O}$ ,  $\text{V}_2\text{O}_5 \cdot x\text{H}_2\text{O}$ , and  $\text{Mg}_{0.3}\text{V}_2\text{O}_5$ . Reprinted with permission from ref. 135. Copyright 2019 Elsevier.

structure (NEXAFS) of V  $K$ -edge revealed that the edge position of the Mg-incorporated  $\text{V}_2\text{O}_5$  was close to that of  $\text{VO}_2$  standard, indicating a stoichiometry of  $\text{MgV}_2\text{O}_5$  for the Mg-incorporated  $\text{V}_2\text{O}_5$ . Moreover, the decreased intensity of the pre-edge peak suggested a local reordering of the V environment upon Mg incorporation. Significantly, the obtained  $\text{MgV}_2\text{O}_5$  electrode exhibited a high specific capacity of  $160 \text{ mA h g}^{-1}$  at  $20 \text{ mA g}^{-1}$ . Nevertheless, the electrochemical performance of pristine  $\text{V}_2\text{O}_5$  was not presented, making it difficult to quantify the contribution of Mg incorporation. Mg can also be incorporated into the crystal structure of  $\text{V}_2\text{O}_5$  during the material synthesis. Xu *et al.*<sup>135</sup> synthesized  $\text{Mg}_{0.3}\text{V}_2\text{O}_5 \cdot 1.1\text{H}_2\text{O}$  nanowires through the reaction between  $\text{V}_2\text{O}_5$  and  $\text{C}_4\text{H}_6\text{O}_4\text{Mg} \cdot 4\text{H}_2\text{O}$ . The  $[\text{MgO}_6]$  octahedra species acted as pillars and enhanced the structural stability of  $\text{V}_2\text{O}_5$ , while water molecules improved the  $\text{Mg}^{2+}$ -intercalation kinetics (Fig. 9a). The  $\text{Mg}_{0.3}\text{V}_2\text{O}_5 \cdot 1.1\text{H}_2\text{O}$  electrode delivered a high specific capacity of  $164 \text{ mA h g}^{-1}$  (Fig. 9b), which is substantially higher than those of  $\text{V}_2\text{O}_5 \cdot 1.1\text{H}_2\text{O}$  ( $114 \text{ mA h g}^{-1}$ ) and  $\text{Mg}_{0.3}\text{V}_2\text{O}_5$  ( $91 \text{ mA h g}^{-1}$ ). Impressively, the  $\text{Mg}_{0.3}\text{V}_2\text{O}_5 \cdot 1.1\text{H}_2\text{O}$  electrode also showed a superior cycling life with 80% capacity retained after 10 000 cycles at a current density of  $1 \text{ A g}^{-1}$ , which remarkably outclassed  $\text{V}_2\text{O}_5 \cdot 1.1\text{H}_2\text{O}$  and  $\text{Mg}_{0.3}\text{V}_2\text{O}_5$  (fast capacity decay over 200 cycles). The incorporation of Mg into the structure was uncovered to improve the conductivity of  $\text{Mg}_{0.3}\text{V}_2\text{O}_5 \cdot 1.1\text{H}_2\text{O}$  (Fig. 9c and d), which contributed to the superior rate performance. XRD studies further observed the slight decrease by  $0.5 \text{ \AA}$  in the interlayer spacing of  $\text{Mg}_{0.3}\text{V}_2\text{O}_5 \cdot 1.1\text{H}_2\text{O}$  after charging. This result indicated that the  $[\text{MgO}_6]$  sites as pillars alleviated the electrode structure change during the charge/discharge process, further accounting for the excellent cycle stability of  $\text{Mg}_{0.3}\text{V}_2\text{O}_5 \cdot 1.1\text{H}_2\text{O}$ .<sup>135,137</sup>

Besides, ammonium<sup>140</sup> or poly(ethylene oxide) (PEO)<sup>141</sup> incorporated between vanadium oxide layers can also promote the  $\text{Mg}^{2+}$ -intercalation kinetics. Impressively,  $\text{NH}_4\text{V}_4\text{O}_{10}$  exhibited the initial specific capacity of  $175 \text{ mA h g}^{-1}$  in the first

cycle, and the specific capacity increased to  $\sim 250 \text{ mA h g}^{-1}$  in the second cycle. The boosted specific capacity was assigned to the irreversible de-ammoniation process occurring at the first charge, which created additional sites for  $\text{Mg}^{2+}$  storage. This de-ammoniation process was identified by the irreversible oxidation peak in the first cyclic voltammetry cycle and the disappearance of the N 1s XPS peak after the first charge. Similarly, PEO-incorporated  $\text{V}_2\text{O}_5 \cdot 1.5\text{H}_2\text{O}$  displayed a superior specific capacity of  $100 \text{ mA h g}^{-1}$ , which substantially outweighed the low specific capacity of  $\text{V}_2\text{O}_5 \cdot 1.5\text{H}_2\text{O}$  ( $20 \text{ mA h g}^{-1}$  at  $10 \text{ mA g}^{-1}$ ).<sup>141</sup> In addition, the specific capacity of PEO-incorporated  $\text{V}_2\text{O}_5 \cdot 1.5\text{H}_2\text{O}$  was stabilized at  $\sim 90 \text{ mA h g}^{-1}$  after 20 cycles, in contrast to the fast capacity decay of  $\text{V}_2\text{O}_5 \cdot 1.5\text{H}_2\text{O}$  ( $4.3 \text{ mA h g}^{-1}$  after 35 cycles). The improved specific capacity of PEO-incorporated  $\text{V}_2\text{O}_5 \cdot 1.5\text{H}_2\text{O}$  was assigned to the interlayer spacing expansion from  $11.6 \text{ \AA}$  for  $\text{V}_2\text{O}_5 \cdot 1.5\text{H}_2\text{O}$  to  $12.6 \text{ \AA}$  for PEO-incorporated  $\text{V}_2\text{O}_5 \cdot 1.5\text{H}_2\text{O}$ .

The  $\text{Mg}^{2+}$ -intercalation kinetics of pristine vanadium oxide can also be improved by the charge/discharge at elevated temperatures. Rastgoo-Deylami *et al.*<sup>142</sup> showed that the capacity of  $\text{V}_3\text{O}_7 \cdot \text{H}_2\text{O}$  was boosted from  $80 \text{ mA h g}^{-1}$  to  $231 \text{ mA h g}^{-1}$  when the temperature was increased from  $25 \text{ }^\circ\text{C}$  to  $60 \text{ }^\circ\text{C}$ . Moreover, initial cycling of the electrode at the elevated temperature was also explored as an activation step for further cycling at room temperature.<sup>93</sup> To activate the cathode, commercial  $\alpha\text{-V}_2\text{O}_5$  was discharged/charged at  $110 \text{ }^\circ\text{C}$  with the electrolyte of  $0.5 \text{ M Mg}(\text{TFSI})_2$  in 1-butyl-1-methyl-pyrrolidinium TFSI ( $\text{Py}_{14}\text{TFSI}$ ). EDS and STEM analysis were used to evaluate the effect of the activation step on the structure of  $\alpha\text{-V}_2\text{O}_5$ . First, the  $\alpha\text{-V}_2\text{O}_5$  cathode after discharge at  $110 \text{ }^\circ\text{C}$  exhibited the uniform distribution of V and Mg, implying that the charge storage mechanism of  $\alpha\text{-V}_2\text{O}_5$  was high-kinetics  $\text{Mg}^{2+}$  intercalation. STEM images of  $\alpha\text{-V}_2\text{O}_5$  at the discharged state revealed the considerable delamination of  $\alpha\text{-V}_2\text{O}_5$ , which lead to the greatly reduced domain size ( $3.5 \text{ nm}$ ). The specific capacity of  $\alpha\text{-V}_2\text{O}_5$  without activation was only  $16 \text{ mA h g}^{-1}$ . Interestingly, after the temperature was increased to  $110 \text{ }^\circ\text{C}$ , the specific capacity increased to  $295 \text{ mA h g}^{-1}$ . Afterwards, the specific capacity could be stabilized at  $96 \text{ mA h g}^{-1}$  after the temperature recovered to room temperature. It should be noted that the activation step of the cathode would be a high-cost step in the battery fabrication process, thus restricting the real-life application of the assembled devices.

Although preliminary studies demonstrated the feasible  $\text{Mg}^{2+}$  storage of layered vanadium oxides in electrolytes like  $\text{Mg}(\text{TFSI})_2$  or  $\text{Mg}(\text{ClO}_4)_2$  in AN and ionic liquids, these electrolytes are generally not compatible with Mg metal anodes. To enable full  $\text{Mg}/\text{V}_2\text{O}_5$  cell, more efforts are needed to develop electrolytes compatible with both  $\text{V}_2\text{O}_5$  cathodes and Mg metal anodes.

Unlike MMB electrolytes, metal anode-compatible AMB electrolytes (*e.g.*,  $\text{AlCl}_3/\text{EMIMCl}$ ) are also suitable for oxide cathodes. AMBs composed of Al metal,  $\text{V}_2\text{O}_5$  nanowires, and  $\text{AlCl}_3/\text{EMIMCl}$  (molar ratio: 1.1) were assembled.<sup>143</sup> As revealed, the  $\text{V}_2\text{O}_5$  cathode delivered a high specific capacity of  $305 \text{ mA h g}^{-1}$  in the first cycle with a voltage plateau of around  $0.5 \text{ V}$ . The specific capacity kept  $273 \text{ mA h g}^{-1}$  after 20 cycles,

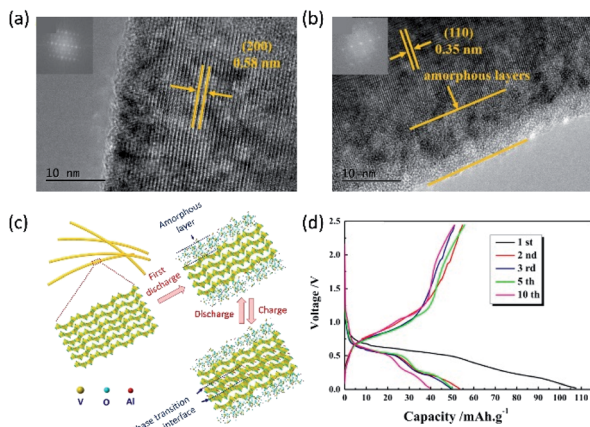


Fig. 10 (a and b) HRTEM images of the  $V_2O_5$  nanowire (a) before cycling, and (b) at the fully discharged state (insets: fast Fourier transform images). (c) Schematic diagram showing the electrochemical  $Al^{3+}$  insertion/extraction of crystallized  $V_2O_5$  nanowires. (d) Galvanostatic charge/discharge profiles of the  $V_2O_5$  nanowire cathode. Reprinted with permission from ref. 108. Copyright 2017 Elsevier.

suggesting decent capacity retention of the  $V_2O_5$  cathode. Recent studies have indicated that stainless steel exhibited nonnegligible electrochemical activity in  $AlCl_3/EMIMCl$  electrolyte.<sup>144</sup> This electrochemical activity could provide false interpretation of the obtained results. To further understand the intercalation of  $Al^{3+}$  into  $V_2O_5$ , Gu and co-workers<sup>108</sup> conducted the high-resolution TEM (HRTEM) analysis on  $V_2O_5$  nanowires at different charge/discharge stages. They found that the intercalation of  $Al^{3+}$  led to the formation of 10 nm amorphous layers on the outer shell of  $V_2O_5$  nanowires. After deintercalation of  $Al^{3+}$ , a new  $V_2O_5$  phase appeared between the outer amorphous layer and the core of nanowires (Fig. 10a–c). The structural evolution suggested that the charge storage of  $V_2O_5$  nanowires occurred only at the surface, and the charge storage mechanism was a combination of intercalation and phase transition. Furthermore, *ex situ* XPS measurements revealed that the oxidation state of V was not fully converted back to  $V^{5+}$  during the charging process. In addition, XPS also indicated the presence of Al after charging. These XPS results were consistent in several studies of AMBs with  $V_2O_5$  cathodes.<sup>108,145</sup> Due to the irreversible electrochemical process, the

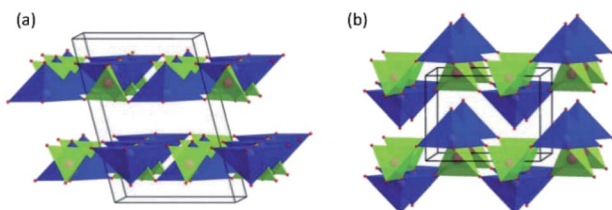


Fig. 11 Representation of (a) the  $\alpha_1$ -VOPO<sub>4</sub> structure ( $C2/m$ ,  $a = 8.73187(14)$  Å,  $b = 6.20548(5)$  Å,  $c = 6.20902(4)$  Å and  $\beta = 104.448(3)^\circ$  at 280 °C) and (b) the  $\alpha_2$ -VOPO<sub>4</sub> structure ( $P4/n$ ,  $a = 6.0156(3)$  Å,  $c = 4.4375(3)$  Å at RT). Reproduced from ref. 147 with permission from The Royal Society of Chemistry.

specific capacity of  $V_2O_5$  decayed fast during cycling, retaining only 40 mA h  $g^{-1}$  after 10 cycles (Fig. 10d). The compatibility of the AMB electrolytes with  $V_2O_5$  will motivate further investigations to improve both the  $Al^{3+}$ -intercalation kinetics and the cycling stability of  $V_2O_5$  via diverse structure engineering strategies.

**3.1.3 Vanadyl phosphate.** Layer-structure VOPO<sub>4</sub> has several phases, such as  $\alpha_1$ -,  $\alpha_2$ -,  $\gamma$ -,  $\delta$ -, and  $\omega$ -VOPO<sub>4</sub>. The common ones for electrochemical intercalation are  $\alpha_1$ -VOPO<sub>4</sub> and  $\alpha_2$ -VOPO<sub>4</sub> with a  $P4/n$  space group.<sup>146</sup> Both phases are based on the corner-sharing  $[PO_4]$  tetrahedra and strongly distorted vanadium octahedra. The difference between  $\alpha_1$ -VOPO<sub>4</sub> and  $\alpha_2$ -VOPO<sub>4</sub> is the position of oxygen atoms in vanadyl groups. The oxygen atoms of  $\alpha_1$ -VOPO<sub>4</sub> are located within the layer, while the oxygen atoms of  $\alpha_2$ -VOPO<sub>4</sub> are not in the same plane as V (Fig. 11).<sup>147</sup> VOPO<sub>4</sub> has attracted significant attention as a possible cathode material due to the large specific capacity, high redox potential, and stable cyclability.<sup>148</sup> Impressively, VOPO<sub>4</sub> can deliver a high theoretical specific capacity of 166 mA h  $g^{-1}$  for the one-electron redox couple  $V^{4+}/V^{5+}$  and 331 mA h  $g^{-1}$  for the two-electron redox couple  $V^{3+}/V^{5+}$ .<sup>149</sup> Due to the enhanced ionic character of V–O bonds when  $(PO_4)^{3-}$  anions are introduced, VOPO<sub>4</sub> possesses a much higher redox potential (3.95 V vs.  $Li^+/Li$ ) than that of  $V_2O_5$  (2–3.4 V vs.  $Li^+/Li$ ).<sup>37,150</sup>

VOPO<sub>4</sub> suffers from significant voltage decay during cycling in aqueous Zn electrolytes, which can be assigned to the decomposition of VOPO<sub>4</sub> into  $VO_x$ . Several studies suggested that low amounts of water additive would not cause the decomposition of VOPO<sub>4</sub>.<sup>59,151</sup> Recently, Wang *et al.*<sup>151</sup> compared the  $Zn^{2+}$ -storage performance of VOPO<sub>4</sub> and VOPO<sub>4</sub>·2H<sub>2</sub>O in both water-free and water-containing electrolytes. VOPO<sub>4</sub>·2H<sub>2</sub>O was synthesized by the reaction between  $V_2O_5$  and concentrated  $H_3PO_4$  under the reflux condition. Subsequently, VOPO<sub>4</sub> was prepared through the calcination of VOPO<sub>4</sub>·2H<sub>2</sub>O at 550 °C in the air. The electrochemical performance was evaluated using 0.1 M Zn(OTf)<sub>2</sub> in AN with/without water. When the water content in the electrolyte was 0.5%, the performance of VOPO<sub>4</sub> showed only slight improvement. By contrast, the specific capacity of VOPO<sub>4</sub> was increased by 3-fold, when the water content reached 1%. The performance improvement was explained by the chemical co-intercalation of free water molecules and the formation of VOPO<sub>4</sub>· $xH_2O$  (Fig. 12a), which was supported by the XRD pattern (Fig. 12b). Besides, the electrochemical performance of VOPO<sub>4</sub>·2H<sub>2</sub>O was evaluated in AN with and without 1% water. Interestingly, the addition of water to the electrolyte can apparently improve the performance of VOPO<sub>4</sub>·2H<sub>2</sub>O. The specific capacities in the water-free electrolyte are 10 and 80 mA h  $g^{-1}$  at 20 mA  $g^{-1}$  for VOPO<sub>4</sub> and VOPO<sub>4</sub>·2H<sub>2</sub>O, respectively. When 1% water was added, the specific capacities were increased to 122 and 135 mA h  $g^{-1}$  at 20 mA  $g^{-1}$  for VOPO<sub>4</sub> and VOPO<sub>4</sub>·2H<sub>2</sub>O, respectively (Fig. 12c). XRD analysis revealed that water molecules were extracted from VOPO<sub>4</sub>·2H<sub>2</sub>O to the electrolyte, thus restricting the solid-state diffusion of  $Zn^{2+}$  (Fig. 12d and e). Apart from the increase of specific capacity, VOPO<sub>4</sub>·2H<sub>2</sub>O in the water-containing electrolyte exhibited an increase of the discharge voltage by  $\sim 0.2$  V and



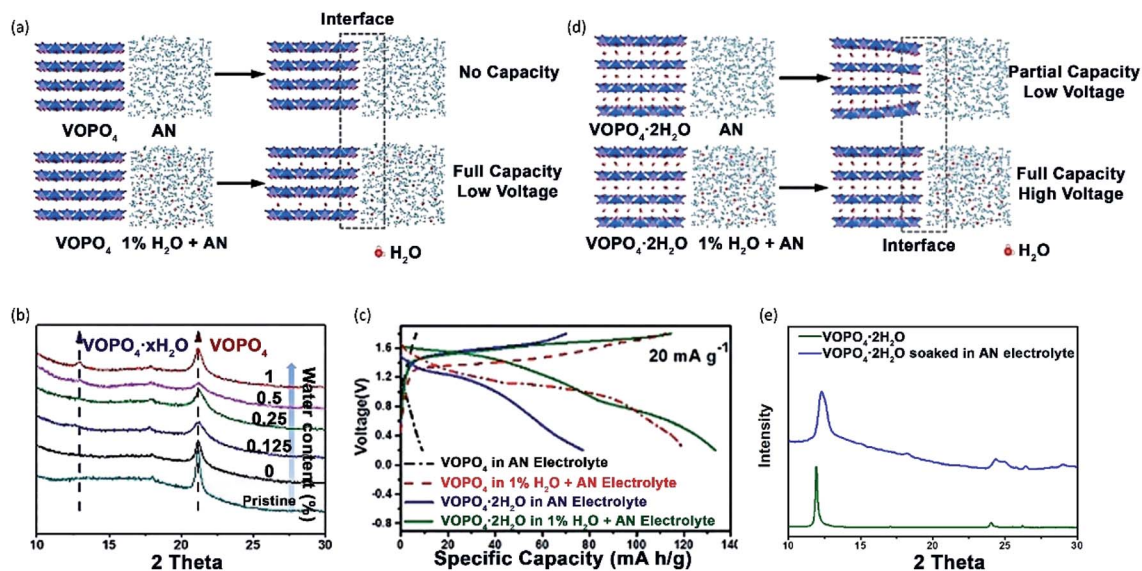


Fig. 12 (a) Schematic illustrations of  $\text{VOPO}_4$  in 0.1 M  $\text{Zn}(\text{OTf})_2$  dissolved in AN without water and with 1%  $\text{H}_2\text{O}$ . (b) XRD patterns of  $\text{VOPO}_4$  soaked in different electrolytes for 24 h. (c) The charge/discharge profiles of  $\text{VOPO}_4$  and  $\text{VOPO}_4 \cdot 2\text{H}_2\text{O}$  between 0.2 V and 1.9 V at  $20 \text{ mA g}^{-1}$ . (d) Schematic illustrations of  $\text{VOPO}_4 \cdot 2\text{H}_2\text{O}$  in 0.1 M  $\text{Zn}(\text{OTf})_2$  dissolved in AN without water and with 1%  $\text{H}_2\text{O}$ . (e) XRD patterns of the pristine  $\text{VOPO}_4 \cdot 2\text{H}_2\text{O}$  and  $\text{VOPO}_4 \cdot 2\text{H}_2\text{O}$  soaked in the electrolyte of 0.1 M  $\text{Zn}(\text{OTf})_2$  dissolved in AN for 24 h. Reprinted with permission from ref. 151. Copyright 2018 Wiley-VCH Verlag GmbH & Co. KGaA, Weinheim.

superior cycling capabilities with  $100 \text{ mA h g}^{-1}$  retained after 25 cycles at  $20 \text{ mA g}^{-1}$ .

To further improve the cyclability of  $\text{VOPO}_4$ , Verma *et al.*<sup>59</sup> synthesized a polypyrrole-incorporated  $\text{VOPO}_4$  (PPy- $\text{VOPO}_4$ ). Polypyrrole between  $\text{VOPO}_4$  layers induced the partial reduction of  $\text{V}^{5+}$  to  $\text{V}^{4+}$ , thus reducing the charge transfer resistance. The capacity retention of PPy- $\text{VOPO}_4$  was increased from 25% for the pristine  $\text{VOPO}_4$  to 90% after 30 cycles at  $30 \text{ mA g}^{-1}$ . In addition, the cyclability was further improved by adding 10% volume of water to the electrolyte, thus enabling  $\text{VOPO}_4 \cdot 2\text{H}_2\text{O}$  with pronouncedly enhanced capacity retention ( $60 \text{ mA h g}^{-1}$  after 350 cycles at  $100 \text{ mA g}^{-1}$ ). The improved stability was ascribed to the presence of polypyrrole, which prevented the distortion of the lattice structure. In contrast,  $\text{VOPO}_4 \cdot 2\text{H}_2\text{O}$  without polypyrrole suffered from the fast capacity decay caused by the extraction of crystal water.

$\text{VOPO}_4$  was also studied as the  $\text{Mg}^{2+}$ -intercalation cathodes, and their performance showed strong dependence on both the interlayer spacing of  $\text{VOPO}_4$  and the water content in the electrolyte. Ji *et al.*<sup>152</sup> studied the effect of water molecules in both the  $\text{VOPO}_4$  structure and the electrolyte on the  $\text{Mg}^{2+}$ -intercalation performance of  $\text{VOPO}_4$ . Interestingly, only when the  $\text{VOPO}_4 \cdot \text{H}_2\text{O}$  cathode with water-containing electrolyte was used, the significant capacity enhancement could be observed. Theoretical calculation indicated that the energy barrier of  $\text{Mg}^{2+}$ -intercalation was reduced from 1.56 eV for  $\text{VOPO}_4$  to 0.48 eV for  $\text{VOPO}_4 \cdot \text{H}_2\text{O}$ . Such a pronounced difference resulted in that the diffusion coefficient of  $\text{VOPO}_4 \cdot \text{H}_2\text{O}$  was  $1.2 \times 10^{18}$  times higher than that of  $\text{VOPO}_4$ . In addition, the calculated formation energies of different  $[\text{Mg}(\text{PC})_n(\text{H}_2\text{O})_{6-n}]^{2+}$  ( $n \leq 6$ ) species in the PC electrolyte without water were much more negative than those in the water-containing PC electrolyte (Fig. 13a). The difference in formation energies revealed the

immense desolvation energy of  $[\text{Mg}(\text{PC})_6]^{2+}$ . Additionally, the improved  $\text{Mg}^{2+}$ -intercalation kinetics contributed to reducing the charge/discharge mid-voltage hysteresis from 1.15 V for

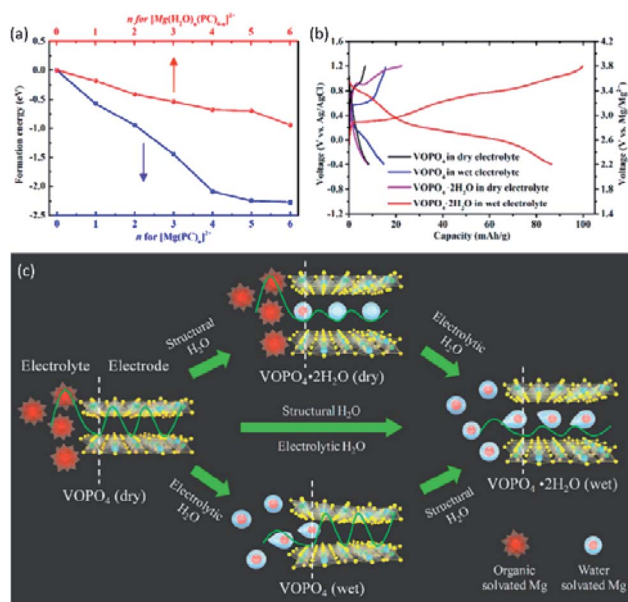


Fig. 13 (a) Formation energies of  $[\text{Mg}(\text{PC})_n]^{2+}$  and  $[\text{Mg}(\text{PC})_n(\text{H}_2\text{O})_{6-n}]^{2+}$  ( $n \leq 6$ ). (b) Voltage profiles of  $\text{VOPO}_4$  and  $\text{VOPO}_4 \cdot 2\text{H}_2\text{O}$  in the water-free (0.1 M  $\text{Mg}(\text{ClO}_4)_2$  in PC) and water-containing (0.1 M  $\text{Mg}(\text{ClO}_4)_2 \cdot 6\text{H}_2\text{O}$  in PC) electrolytes at  $5 \text{ mA g}^{-1}$  in a three-electrode cell with  $\text{Ag}/\text{AgCl}$  and active carbon as the reference and counter electrode, respectively. (c) Schematic illustrating the charge storage mechanism of  $\text{VOPO}_4 \cdot n\text{H}_2\text{O}$  in the water-free and water-containing electrolytes. The green curves indicate the activation energy barriers, and the white dash lines represent the electrode/electrolyte interface. Reprinted with permission from ref. 152. Copyright 2018 American Chemical Society.



VOPO<sub>4</sub> in the water-free electrolyte to 0.49 V for VOPO<sub>4</sub>·2H<sub>2</sub>O in the water-containing electrolyte (Fig. 13b). The average equilibrium voltages in electrolytes with various water contents were also calculated for the V<sup>5+</sup>/V<sup>4+</sup> redox stage (Mg<sub>0.5</sub>VOPO<sub>4</sub>) and the V<sup>4+</sup>/V<sup>3+</sup> redox stage (MgVOPO<sub>4</sub>). The V<sup>4+</sup>/V<sup>3+</sup> stage displayed a pronounced dependence on the water content in electrolytes compared with the V<sup>5+</sup>/V<sup>4+</sup> stage. The voltage plateau improved from 1.79 V to 2.19 V, when the water activity was increased from 10<sup>-6</sup> to 10<sup>-2</sup>. To clarify the influence of water, Fig. 13c illustrates how Mg<sup>2+</sup> intercalation into VOPO<sub>4</sub> and VOPO<sub>4</sub>·2H<sub>2</sub>O in both water-free and water-containing electrolytes.

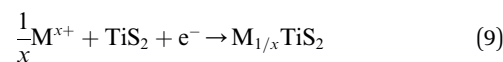
As mentioned earlier, water-containing electrolytes are not compatible with the Mg metal anode owing to the formation of the passivation layer on the Mg surface. By incorporating phenylamine molecules between VOPO<sub>4</sub> layers (denoted PA-VOPO<sub>4</sub>), efficient Mg<sup>2+</sup> intercalation in a water-free electrolyte was achieved.<sup>153</sup> PA-VOPO<sub>4</sub> was prepared by the exfoliation and self-assemble of VOPO<sub>4</sub>·2H<sub>2</sub>O nanosheets in a phenylamine solution (Fig. 14a). Phenylamine enabled VOPO<sub>4</sub> with apparent layer expansion (interlayer distance: 7.4 vs. 14.2 Å). The large interlayer distance of PA-VOPO<sub>4</sub> reduced the electrostatic interaction between the intercalating Mg<sup>2+</sup> and VOPO<sub>4</sub>. Meanwhile, the interlayer expansion also boosted the charge-storage kinetics of VOPO<sub>4</sub> by promoting the intercalation of MgCl<sup>+</sup> (Fig. 14b–d).<sup>153,154</sup> Impressively, PA-VOPO<sub>4</sub> kept 87% of the initial specific capacity after 500 cycles at 100 mA g<sup>-1</sup>, which was superior to that of VOPO<sub>4</sub>·2H<sub>2</sub>O (40% after 150 cycles). Moreover, PA-VOPO<sub>4</sub> showed a decent rate performance with high

specific capacities of 275 and 109 mA h g<sup>-1</sup> at 50 and 2000 mA g<sup>-1</sup>, respectively (Fig. 14e). The excellent cycling stability of PA-VOPO<sub>4</sub> is rather unique, given the APC electrolyte is known to be incompatible with oxides. Recently, Hu *et al.*<sup>155</sup> suggested that the incorporated PA molecules could improve the stability of VOPO<sub>4</sub> in aqueous ZMBs due to the increased hydrophobicity of PA-VOPO<sub>4</sub>. It is highly desirable to understand the stability of PA-VOPO<sub>4</sub> in the APC electrolyte with future efforts. In addition, the low charge/discharge voltages and the higher specific capacities of PA-VOPO<sub>4</sub> than the theoretical value should be further clarified.

### 3.2 Transition metal dichalcogenides

Transition metal dichalcogenides, sharing the formula MX<sub>2</sub>, are made of transition metal (M = Ti, V, Nb, Mo, W, *etc.*) and chalcogen (X = S, Se, and Te) atoms. The TMD layer has a three-atom-thick configuration of X–M–X. Stacked layers are connected by weak vdW interactions, allowing the exfoliation of bulk TMD into single-layer and few-layer TMD nanoflakes.<sup>42</sup> TMDs have three polytypes, namely, trigonal prismatic, octahedral, and distorted octahedral, which differ in the metal atom coordination configuration and stacking orders. The electronic properties of TMDs (metallic, semiconducting, and insulating) are determined by the different polytypes and chalcogen types.<sup>41,156</sup> The weaker electrostatic interactions between chalcogenide anions and the intercalating cations account for the better multivalent metal ion-intercalation kinetics of TMD cathodes than that of TMO cathodes.<sup>157</sup> Generally, TMDs exhibit the intercalation mechanism at potentials above ~1.0 V vs. Li<sup>+</sup>/Li. Under a low cut-off voltage (below ~1.0 V vs. Li<sup>+</sup>/Li), the specific capacities of TMDs are substantially enhanced due to the involved conversion reactions.

**3.2.1 Ti-based TMDs.** Titanium disulphide (TiS<sub>2</sub>) and titanium diselenide (TiSe<sub>2</sub>) show tetragonal symmetry and metallic properties, exhibiting layer spacings of 5.65 Å and 6.00 Å, respectively. TiS<sub>2</sub> depicts a theoretical specific capacity of 239 mA h g<sup>-1</sup> for the one-electron Ti<sup>3+</sup>/Ti<sup>4+</sup> reaction, as shown in eqn (9). Compared with TiS<sub>2</sub>, TiSe<sub>2</sub> has a lower theoretical specific capacity of 130 mA h g<sup>-1</sup>, but better cation-intercalation kinetics.<sup>157</sup> The superior cation-intercalation kinetics of TiSe<sub>2</sub> originates from the unique hybridization between Ti 3d orbitals and Se 4p orbitals, which boosts the electron delocalization and reduces the electrostatic interactions between the intercalating cations and TiSe<sub>2</sub> (Fig. 15a and b).<sup>157,158</sup> In addition, TiSe<sub>2</sub> displays the lowest charge rehybridization upon Mg<sup>2+</sup> intercalation in comparison with TiS<sub>2</sub> and TiO<sub>2</sub>, further implying the lowest Mg<sup>2+</sup>-diffusion barrier of TiSe<sub>2</sub> (Fig. 15c).<sup>157</sup>



Several strategies were applied to improve the Mg<sup>2+</sup>-intercalation performance of Ti-based TMDs, such as particle size optimization, temperature increase, and interlayer expansion. Tao *et al.*<sup>159</sup> studied the Mg<sup>2+</sup>-intercalation behaviours of the TiS<sub>2</sub> nanotubes and large-flake TiS<sub>2</sub> (20 μm). TiS<sub>2</sub> nanotubes

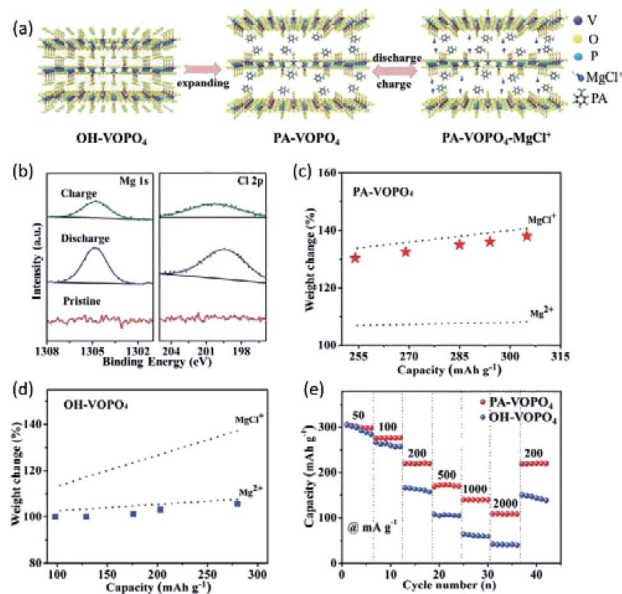
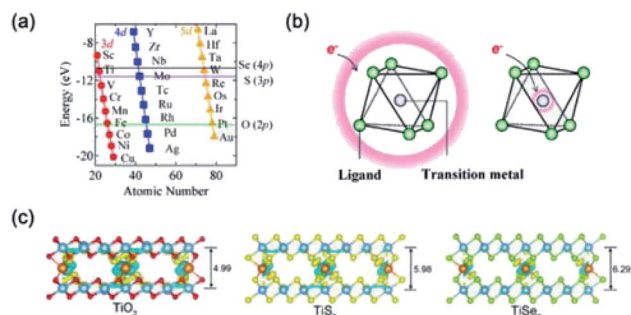
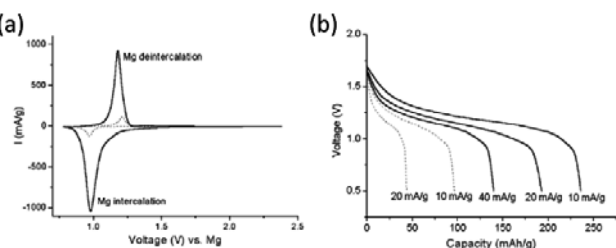


Fig. 14 (a) Schematic illustration of the experimental approach and proposed mechanism of PA-VOPO<sub>4</sub> nanosheets as the Mg-storage material. (b) Mg 1s and Cl 2p XPS spectra of PA-VOPO<sub>4</sub> nanosheets at the fully charged/discharged states. Mass change of the electrodes upon discharge when (c) PA-VOPO<sub>4</sub> nanosheets and (d) VOPO<sub>4</sub>·2H<sub>2</sub>O bulk served as cathode materials. (e) Rate capability of VOPO<sub>4</sub>·2H<sub>2</sub>O bulk and PA-VOPO<sub>4</sub> nanosheets. Reprinted with permission from ref. 153. Copyright 2018 Wiley-VCH Verlag GmbH & Co. KGaA, Weinheim.



**Fig. 15** (a) Energy diagram of atomic orbitals. Red circles, blue squares and orange triangles represent the energy levels of 3d-, 4d- and 5d-orbitals of each transition metal, respectively. The horizontal lines display the energy level position of O 2p-orbital, S 3p-orbital and Se 4p-orbital, respectively. (b) A schematic illustration of charge distribution in the electronic state with strong d–p hybridization. Electrons are accommodated in the delocalized state, which extends over transition metal and ligand atoms as schematically shown by the red framework. Reprinted with permission from ref. 158. Copyright 2015, Springer Nature. (c) Charge rehybridization upon the diffusion of  $\text{Mg}^{2+}$  between layers of  $\text{TiO}_2$ ,  $\text{TiS}_2$ , and  $\text{TiSe}_2$  with layer spacing (unit Å). Charge accumulation is shown in yellow, while depletion is shown in blue. Oxygen atoms are shown as small red spheres, sulfur as small yellow spheres, selenium as small kelly spheres, Ti as large sapphire spheres, and Mg at the center as an orange sphere. The isovalue number used for displaying the differential charge density is 0.003. Reprinted with permission from ref. 157. Copyright 2019 American Chemical Society.

( $234 \text{ mA h g}^{-1}$ ) delivered more than double the capacity of the large-flake  $\text{TiS}_2$  ( $96 \text{ mA h g}^{-1}$ ) at  $10 \text{ mA g}^{-1}$  (Fig. 16). In addition to the particle size, the  $\text{Mg}^{2+}$ -intercalation kinetics of  $\text{TiS}_2$  was shown to be highly temperature-dependent. For example, Sun *et al.*<sup>160</sup> demonstrated efficient  $\text{Mg}^{2+}$  intercalation into  $\text{TiS}_2$  using the APC electrolyte at  $60^\circ\text{C}$ . The  $\text{TiS}_2$  electrode at  $60^\circ\text{C}$  exhibited the initial specific capacity of  $270 \text{ mA h g}^{-1}$  at  $12 \text{ mA g}^{-1}$  and a reversible capacity of  $160 \text{ mA h g}^{-1}$  in the following cycles. Interestingly, a fast decay of the specific capacity (to  $\sim 110 \text{ mA h g}^{-1}$  after 40 cycles) suggested that neither  $\text{TiS}_2$  nor the Mg anode was stable during cycling at high temperatures. To understand the  $\text{Mg}^{2+}$ -intercalation mechanism of  $\text{TiS}_2$ , *in situ* XRD revealed the appearance of several new phases during the discharge process of  $\text{TiS}_2$ . At the initial



**Fig. 16** (a) Cyclic voltammograms at  $0.5 \text{ mV s}^{-1}$  of  $\text{TiS}_2$  nanotube (solid) and polycrystalline powder (dots) electrodes at  $20^\circ\text{C}$ . (b) Discharge curves of  $\text{TiS}_2$  nanotubes (solid) and polycrystalline  $\text{TiS}_2$  (dots) at various current densities and  $20^\circ\text{C}$ . Reproduced from ref. 159 with permission from The Royal Society of Chemistry.

discharge stage, partially irreversible interlayer expansion ( $c$  parameter increase) occurred, followed by the reversible increase in the  $a$  parameter. The increase in the  $c$  parameter was explained by  $\text{Mg}^{2+}$  intercalation into the octahedral sites of  $\text{TiS}_2$ , while the change in the  $a$  parameter indicated  $\text{Mg}^{2+}$  intercalation into the tetrahedral sites.

Yoo *et al.*,<sup>154</sup> reported the electrochemical intercalation of organic  $\text{Py}_{14}^+$  cations into  $\text{TiS}_2$  interlayers, which remarkably improved the  $\text{Mg}^{2+}$ -intercalation kinetics and promoted  $\text{Mg-Cl}^+$  intercalation. In this case,  $\text{Py}_{14}\text{Cl}$  ionic liquid was added to the APC electrolyte.  $\text{Py}_{14}^+$  cations were intercalated into  $\text{TiS}_2$  at a low rate ( $5 \text{ mA g}^{-1}$ ), causing the irreversible interlayer expansion of  $\text{TiS}_2$  (Fig. 17a). As a result, the specific capacity of  $\text{TiS}_2$  was remarkably increased from  $\sim 25 \text{ mA h g}^{-1}$  to  $239 \text{ mA h g}^{-1}$  at  $24 \text{ mA g}^{-1}$  (Fig. 17b). Moreover, the specific capacity of  $239 \text{ mA h g}^{-1}$  was boosted to  $400 \text{ mA h g}^{-1}$  at a high temperature of  $60^\circ\text{C}$ , corresponding to the intercalation of two  $\text{Mg-Cl}^+$  species per Ti atom. N 1s XPS spectra revealed that only  $\text{Py}_{14}^+$  cations were intercalated into  $\text{TiS}_2$  at the beginning of the first discharge. Cl 2p and Mg 2s XPS signals appeared at a later stage of the discharge, which indicated the intercalation of  $\text{MgCl}^+$  after the expansion of the interlayer distance by  $\text{Py}_{14}^+$ . Besides, Mg K-edge NEXAFS of  $\text{Mg}^{2+}$ -intercalated  $\text{TiS}_2$  displayed a similar onset energy with tetra-coordinated  $[\text{Mg}_2\text{Cl}_2 \cdot 4\text{THF}]^{2+}$ , implying that the intercalated  $\text{Mg}^{2+}$  was tetra-coordinated with one Cl atom and three S atoms.  $\text{MgCl}^+$  acting as charge carriers improved the intercalation kinetics due to its lower charge density than that of  $\text{Mg}^{2+}$ . Additionally,  $\text{MgCl}^+$  avoided the Mg-Cl dissociation step, and exhibited weaker binding to S than  $\text{Mg}^{2+}$  (Fig. 17c and d).

Besides, the  $\text{Al}^{3+}$  intercalation kinetics into  $\text{TiS}_2$  shows a strong dependency on the temperature and the particle size of  $\text{TiS}_2$ . Geng *et al.*<sup>106</sup> compared the  $\text{Al}^{3+}$  intercalation into  $\text{TiS}_2$  at room temperature and  $50^\circ\text{C}$ . As revealed, the specific capacity of  $\text{TiS}_2$  at room temperature achieved  $50 \text{ mA h g}^{-1}$  in the initial cycle and decayed to  $30 \text{ mA h g}^{-1}$  after 50 cycles at  $5 \text{ mA g}^{-1}$ . By contrast, the specific capacity of  $\text{TiS}_2$  at  $50^\circ\text{C}$  reached  $45 \text{ mA h g}^{-1}$  and increased to  $70 \text{ mA h g}^{-1}$  after 50 cycles. The authors claimed that cycling at high temperatures altered the crystal structure of  $\text{TiS}_2$ , thus facilitating  $\text{Al}^{3+}$  intercalation. Hawkins *et al.*<sup>161</sup> showed that  $\text{TiS}_2$  nanobelts, cycled at  $50^\circ\text{C}$ , displayed a superior specific capacity of  $150 \text{ mA h g}^{-1}$  even at a high current density of  $240 \text{ mA g}^{-1}$ . It was suggested that both  $\text{Al}^{3+}$  and  $\text{AlCl}_4^-$  could be intercalated into  $\text{TiS}_2$  nanobelts, which also accounted for the improved intercalation kinetics.<sup>30,108,162–164</sup>

**3.2.2 V-based TMDs.** Vanadium disulphide ( $\text{VS}_2$ ) and vanadium diselenide ( $\text{VSe}_2$ ) exhibit metallic properties, tetragonal symmetry, and layer spacings of  $5.74 \text{ \AA}$  and  $6.10 \text{ \AA}$ , respectively.<sup>165</sup> The one-electron  $\text{V}^{4+}/\text{V}^{3+}$  redox reaction enables  $\text{VS}_2$  and  $\text{VSe}_2$  with theoretical specific capacities of  $233 \text{ mA h g}^{-1}$  and  $128 \text{ mA h g}^{-1}$ , respectively. Nevertheless, the strong orbital hybridization in  $\text{VSe}_2$  accounts for the superior cation-intercalation kinetics of  $\text{VSe}_2$  to that of  $\text{VS}_2$ . Therefore, pristine  $\text{VSe}_2$  exhibited higher specific capacity than pristine  $\text{VS}_2$  (Fig. 18).<sup>157</sup> Apart from intercalation, reversible conversion mechanism was also observed for  $\text{VS}_2$  and  $\text{VSe}_2$  in alkali metal-

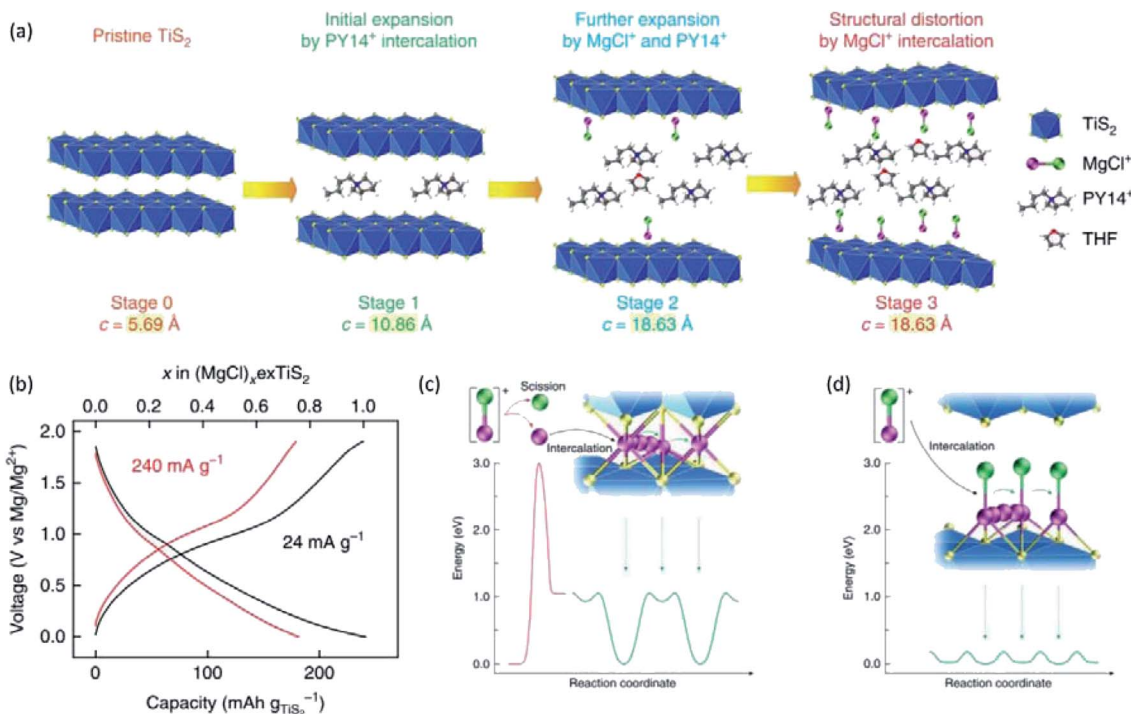


Fig. 17 (a) A schematic illustrating the structural evolution of  $\text{TiS}_2$  at different stages of intercalation. (b) Galvanostatic voltage profiles of the exfoliated  $\text{TiS}_2$  electrode at 24 and  $240 \text{ mA g}^{-1}$  at  $25^\circ\text{C}$ . The number of  $\text{MgCl}^+$  intercalation per exfoliated  $\text{TiS}_2$  is also shown in the top axis. (c and d) Energy diagrams for the intercalation and diffusion of  $\text{Mg}^{2+}$  and  $\text{MgCl}^+$ . (c) Typical intercalation of  $\text{Mg}^{2+}$  involves the scission of  $\text{MgCl}^+$  ions into  $\text{Mg}^{2+}$  and  $\text{Cl}^-$ , which requires substantial activation energy of 3 eV at least. Subsequent diffusion of divalent  $\text{Mg}^{2+}$  also has a high-migration energy barrier of 1.06 eV, which results in the limited level of intercalation at room temperature. (d) Intercalation of  $\text{MgCl}^+$  bypasses the sluggish scission of the  $\text{Mg}-\text{Cl}$  bond at the electrolyte–cathode interface. Afterwards,  $\text{MgCl}^+$  diffuses fast in the expanded interlayers due to the fairly low-migration energy barrier of 0.18 eV. Mg and Cl atoms are shown as purple and green spheres, respectively. Reprinted with permission from ref. 154. Copyright 2017, Springer Nature.

ion batteries, empowering them with high specific capacities ( $>700 \text{ mA h g}^{-1}$ ).<sup>41,166</sup>

To improve the  $\text{Mg}^{2+}$ -intercalation kinetics of  $\text{VS}_2$ , several interlayer expansion strategies were developed for  $\text{VS}_2$ . For example, Xue *et al.*<sup>167</sup> synthesized  $\text{VS}_2$  through a solvothermal reaction employing 2-ethylhexylamine as the solvent. Consequently, 2-ethylhexylamine molecules were incorporated into the  $\text{VS}_2$  structure during the synthesis, obtaining interlayer-expanded  $\text{VS}_2$  nanoflowers (Fig. 19a). The single-step preparation of the expanded  $\text{VS}_2$  is vital for practical application, as the industry could not rely on elaborated post-synthesis steps. The combined XRD and Fourier transform infrared results verified

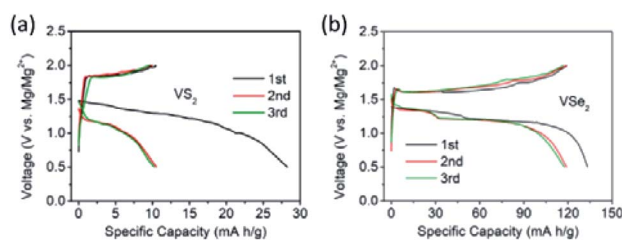
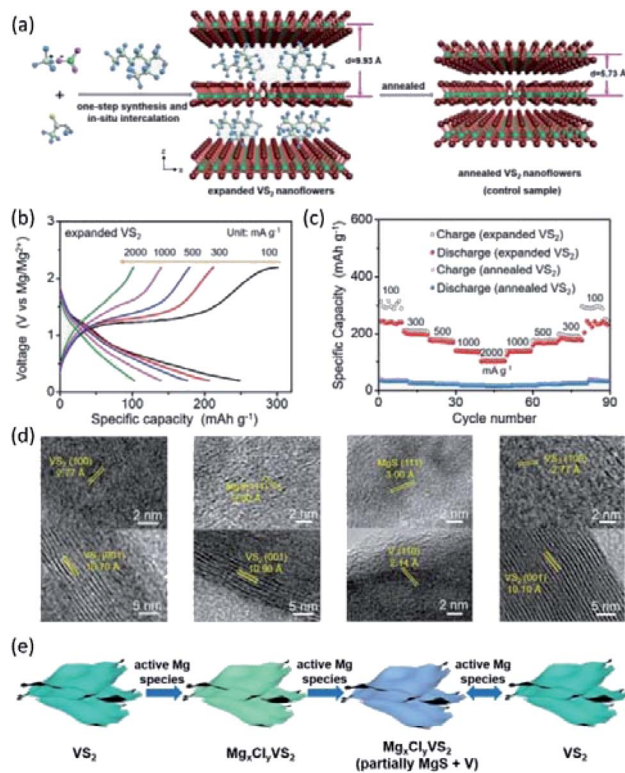


Fig. 18  $\text{Mg}^{2+}$  intercalation into (a) pristine  $\text{VS}_2$  and (b) pristine  $\text{VSe}_2$  at  $5 \text{ mA g}^{-1}$ . Reprinted with permission from ref. 157. Copyright 2019 American Chemical Society.

that 2-ethylhexylamine molecules were located between  $\text{VS}_2$  interlayers, rather than on the surface of  $\text{VS}_2$ . Impressively, the fabricated  $\text{VS}_2$  exhibited a large interlayer spacing of  $9.93 \text{ \AA}$ , which contrasted with the small interlayer distance of the annealed  $\text{VS}_2$  ( $5.73 \text{ \AA}$ ). The expanded  $\text{VS}_2$  showed superior electrochemical performance with a high specific capacity of  $245 \text{ mA h g}^{-1}$  at  $100 \text{ mA g}^{-1}$  and 77% capacity retention after 100 cycles. Moreover, an excellent rate capability of the expanded  $\text{VS}_2$  was evidenced by the high specific capacities of 140 and  $102 \text{ mA h g}^{-1}$  at current densities of 1 and  $2 \text{ A g}^{-1}$ , respectively (Fig. 19b and c). XPS spectra of the expanded  $\text{VS}_2$  electrode at different discharge stages presented both Mg 2s and Cl 2p signals with an Mg : Cl ratio  $>1$ , implying both  $\text{Mg}^{2+}$  and  $\text{MgCl}^+$  intercalation. The diffusion coefficient of  $\text{Mg}^{2+}/\text{MgCl}^+$  in the expanded  $\text{VS}_2$  was calculated to be in the range of  $7.58 \times 10^{-11}$  to  $6.03 \times 10^{-13} \text{ cm}^2 \text{ s}^{-1}$ , which was substantially higher than the  $\text{Mg}^{2+}$ -diffusion coefficient of pristine  $\text{VS}_2$  ( $4.20 \times 10^{-23} \text{ cm}^2 \text{ s}^{-1}$ ). The *ex situ* XRD and HRTEM measurements showed that a conversion reaction occurred at a low voltage range ( $<0.4 \text{ V vs. Mg}^{2+}/\text{Mg}$ ), forming  $\text{MgS}$  and  $\text{V}$  (Fig. 19d and e).  $\text{MgS}$  and  $\text{V}$  were not observed when the expanded  $\text{VS}_2$  was charged back to 2.2 V, indicating the good reversibility of the conversion reaction.

Another method to increase the interlayer distance of  $\text{VS}_2$  relies on the irreversible electrochemical intercalation of ionic





**Fig. 19** (a) Schematic illustration of the one-step synthesis and *in situ* intercalation process of the expanded VS<sub>2</sub> nanoflowers and annealed VS<sub>2</sub> nanoflowers. (b) Galvanostatic discharge/charge profiles at various current densities. (c) Rate capabilities of the expanded VS<sub>2</sub> and annealed VS<sub>2</sub> electrodes at the current densities from 100 to 2000 mA g<sup>-1</sup>. (d) HRTEM images of the expanded VS<sub>2</sub> nanoflowers at different discharge/charge states (from left to right): discharged to 0.6 V, discharged to 0.4 V, fully discharged to 0.2 V, and fully charged to 2.2 V. (e) Schematic of the reversible storage mechanism of active Mg species in the expanded VS<sub>2</sub> nanoflowers. Reprinted with permission from ref. 167. Copyright 2019 Wiley-VCH Verlag GmbH & Co. KGaA, Weinheim.

liquid cations.<sup>80,154</sup> Recently, Zhao *et al.*<sup>80</sup> used PP<sub>14</sub>Cl as an electrolyte additive to enable PP<sub>14</sub><sup>+</sup> intercalation between VS<sub>2</sub> layers. During the electrochemical activation at 20 mA g<sup>-1</sup>, PP<sub>14</sub><sup>+</sup> was intercalated between VS<sub>2</sub> nanosheets. *Ex situ* XPS analysis of the VS<sub>2</sub> electrode showed no change in the N 1s signal after the first discharge, indicating the irreversibility of PP<sub>14</sub><sup>+</sup> intercalation. After the activation, VS<sub>2</sub> nanosheets exhibited high specific capacities of 299 and 214 mA h g<sup>-1</sup> at 50 and 2000 mA g<sup>-1</sup>, respectively. Moreover, a high energy density of 152 W h kg<sup>-1</sup> at a power density of 1600 W kg<sup>-1</sup> was achieved by VS<sub>2</sub> nanosheets. It should be pointed out that a significant amount of capacity was detected at the low voltage range (*e.g.*, 150 mA h g<sup>-1</sup> between 0.5–0.01 V at 20 mA g<sup>-1</sup>). The contribution of the capacity at the low voltage range was considerably low, and the low voltage was shown to affect the cyclability of TMDs in alkali metal batteries due to the occurring conversion reaction.<sup>168,169</sup>

Compared to Mg<sup>2+</sup> intercalation, Li<sup>+</sup> intercalation generally shows higher kinetics owing to the low charge density.<sup>157,165</sup> In

this regard, Sun *et al.*<sup>170</sup> reported hybrid devices combining Mg stripping/plating anodes and Li<sup>+</sup>-intercalation VS<sub>2</sub> cathodes. Such Mg–Li hybrid device exploited both the stable Mg stripping/plating on the anode, and the efficient Li<sup>+</sup>-intercalation into VS<sub>2</sub> cathode. Impressively, the specific capacity of the VS<sub>2</sub> cathode was increased by 10 folds (from <25 to 250 mA h g<sup>-1</sup> at 0.5C) by adding LiCl to the APC electrolyte. EDS mapping of VS<sub>2</sub> nanosheets after discharge showed no Mg signal, confirming the negligible intercalation of Mg<sup>2+</sup> into VS<sub>2</sub>. The galvanostatic intermittent titration technique (GITT) verified that the diffusion coefficient of Li<sup>+</sup> in VS<sub>2</sub> was around 10<sup>-13</sup> cm s<sup>-1</sup> even at a high Li content (*e.g.*, Li<sub>2</sub>VS<sub>2</sub>). By contrast, the diffusion coefficient of Mg<sup>2+</sup> in VS<sub>2</sub> dropped from 10<sup>-14</sup> to 10<sup>-15</sup> cm s<sup>-1</sup> along with the slight change of Mg<sup>2+</sup> content from Mg<sub>0.025</sub>VS<sub>2</sub> to Mg<sub>0.04</sub>VS<sub>2</sub>. Thereby, the specific capacity improvement was thus ascribed to the higher diffusivity of Li<sup>+</sup> in VS<sub>2</sub> than that of Mg<sup>2+</sup>. This study opens up an interesting direction for Mg–alkali metal hybrid batteries, which can be extended to constructing other energy storage systems, such as Mg–Na, Mg–K hybrid batteries. Still, alkali ions were consumed during the discharge process of VS<sub>2</sub>. Such a fact requires the use of a large volume of electrolyte to assemble the device, consequently reducing the overall device performance.

V-based TMDs were also used as cathode materials for Al<sup>3+</sup> intercalation. Wu *et al.*<sup>171</sup> investigated the use of VS<sub>2</sub> and graphene-composited VS<sub>2</sub> (G-VS<sub>2</sub>) as cathodes for AMBs. VS<sub>2</sub> was prepared using a hydrothermal method, and G-VS<sub>2</sub> was prepared by sonicating graphene together with VS<sub>2</sub>. The G-VS<sub>2</sub> and VS<sub>2</sub> electrodes achieved specific capacities of 186 and 145 mA h g<sup>-1</sup> in the initial cycle at 100 mA g<sup>-1</sup>, and maintained 50 and 25 mA h g<sup>-1</sup> after 50 cycles, respectively. The reversible Al<sup>3+</sup> intercalation was identified by the *in situ* XRD analysis of G-VS<sub>2</sub>, in which the intensity of VS<sub>2</sub> peaks decreased and increased reversibly during discharge and charge. The improved performance of the G-VS<sub>2</sub> cathode was associated with the reduced charge transfer resistance of G-VS<sub>2</sub> in comparison with VS<sub>2</sub>. Furthermore, Lei *et al.*<sup>172</sup> investigated single-crystal VSe<sub>2</sub> as the cathodes for AMBs. The XPS analysis indicated that AlCl<sub>4</sub><sup>-</sup> served as the dominant charge carrier for VSe<sub>2</sub>. The VSe<sub>2</sub> cathode exhibited the initial capacity of 650 mA h g<sup>-1</sup> at 100 mA g<sup>-1</sup>, which decayed to 50 mA h g<sup>-1</sup> after 100 cycles. The rapid decay in the specific capacity of VS<sub>2</sub> and VSe<sub>2</sub> needs to be further clarified in the future.

**3.2.3 Mo-based TMDs.** Both molybdenum disulphide (MoS<sub>2</sub>) and molybdenum diselenide (MoSe<sub>2</sub>) show the hexagonal symmetry with two possible stacking configurations, namely, the 2H and 3R phases. The interlayer distances of the 2H phases are 6.15 and 6.7 Å for MoS<sub>2</sub> and MoSe<sub>2</sub>, respectively. The 3R MoS<sub>2</sub> and MoSe<sub>2</sub> phases exhibit larger interlayer distances of 6.12 and 6.7 Å, respectively. In addition, the most common monolayer polytypes are semiconducting trigonal prismatic (2H) and metallic octahedral (1T). The 2H phase is thermodynamically favourable, and phase transition from 2H to 1T can occur during the electrochemical/chemical processes, such as intercalation and exfoliation.<sup>173,174</sup> The theoretical capacities associated with the Mo<sup>3+</sup>/Mo<sup>4+</sup> transition are 168 and 106 mA h g<sup>-1</sup> for MoS<sub>2</sub> and MoSe<sub>2</sub>, respectively.<sup>175</sup> Nevertheless,

below  $\sim 1.1$  V vs.  $\text{Li}^+/\text{Li}$ , both  $\text{MoS}_2$  and  $\text{MoSe}_2$  can undergo reversible conversion reactions, allowing high specific capacities of  $>700$   $\text{mA h g}^{-1}$ .

Due to the large interlayer spacing,  $\text{MoS}_2$  can enable efficient  $\text{Mg}^{2+}$  intercalation. Liang *et al.*<sup>176</sup> assembled devices composed of Mg nanoparticles as the anodes and highly exfoliated graphene-like  $\text{MoS}_2$  (G- $\text{MoS}_2$ ) as the cathodes. G- $\text{MoS}_2$  exhibited an enlarged interlayer spacing of 6.5–7 Å in comparison with bulk  $\text{MoS}_2$  (B- $\text{MoS}_2$ , 6.3 Å). The reduced particle size, together with the enlarged lattice spacing, increased the  $\text{Mg}^{2+}$ -intercalation kinetics of G- $\text{MoS}_2$ . As a result, G- $\text{MoS}_2$  exhibited a superior specific capacity of 170  $\text{mA h g}^{-1}$  at 20  $\text{mA g}^{-1}$ , which was significantly higher than the specific capacity of B- $\text{MoS}_2$  (71  $\text{mA h g}^{-1}$ , Fig. 20a) and comparable with the calculated theoretical specific capacity of 223.2  $\text{mA h g}^{-1}$  (Fig. 20b). Interestingly, the excellent specific capacity highly depended on the anode configuration as well. In specific, with the bulk Mg anode, the specific capacity of the G- $\text{MoS}_2$  cathode was two-time lower (90  $\text{mA h g}^{-1}$ ) than the specific capacity of G- $\text{MoS}_2$  with the Mg nanoparticle anode (170  $\text{mA h g}^{-1}$ ). The authors proposed that the formation of a thin passivation layer on the Mg nanoparticle anode promoted the  $\text{Mg}^{2+}$  diffusion across the particle surface. Yet, no experimental evidence was provided to identify the formation of the passivation film and the amount of electrolyte that is consumed during the film formation. In addition, the formation of passivation layers is usually avoided in the chlorine-containing electrolyte.

To improve the cyclability of the  $\text{MoS}_2$  cathodes for MMBs, polyvinylpyrrolidone (PVP) was incorporated between  $\text{MoS}_2$  layers during the hydrothermal synthesis of  $\text{MoS}_2$ .<sup>177</sup> The interlayer spacings of the expanded  $\text{MoS}_2$  with and without PVP were determined to be 9.7 Å and 9.4 Å, respectively. Additionally, PVP-incorporated  $\text{MoS}_2$  exhibited a new XRD peak at 18.4°, implying the new lamellar phase constructed from PVP and  $\text{MoS}_2$  monolayers, with an interlayer spacing of 4.8 Å. An initial specific capacity of 143.3  $\text{mA h g}^{-1}$  at the first discharge and 92% capacity retention after 100 cycles were reached by PVP-incorporated  $\text{MoS}_2$ . In contrast, expanded  $\text{MoS}_2$  without PVP

delivered a specific capacity of 131.9  $\text{mA h g}^{-1}$ , but retained only 52% of the initial capacity after 100 cycles.

In addition to the interlayer expansion, altering the Mg-cation intercalating species was used to improve the electrochemical performance of  $\text{MoS}_2$ . Li *et al.*<sup>174</sup> showed that  $[\text{Mg}(\text{DME})_3]^{2+}$  intercalation into porous 2H- $\text{MoS}_2$ @C exhibited superior kinetics to the  $\text{Mg}^{2+}$ -intercalation kinetics. The mixture of  $\text{Mg}(\text{BH}_4)_2$  and hexafluoroisopropanol in DME was employed as the electrolyte (denoted MgBOR/DME), in which  $[\text{Mg}(\text{DME})_3]^{2+}$  cations acted as the charge carrier ion.  $[\text{Mg}(\text{DME})_3]^{2+}$  intercalation was confirmed using the STEM-EDS analysis, which uncovered similar distribution of O and Mg in the outer layer of 2H- $\text{MoS}_2$ @C. Moreover, the XPS peak analysis revealed that 2H- $\text{MoS}_2$  underwent a phase transition to 1T- $\text{MoS}_2$  during the initial activation process (20 cycles at 20  $\text{mA g}^{-1}$ ). HRTEM image of the 2H- $\text{MoS}_2$ @C cathode after 30th discharge cycles showed an amorphous outer layer, which indicated the fragmentation and structural distortion of  $\text{MoS}_2$  during extended  $[\text{Mg}(\text{DME})_3]^{2+}$  intercalation/de-intercalation. Fig. 21 illustrates the charge storage process of 2H- $\text{MoS}_2$ @C, including the intercalation of large  $[\text{Mg}(\text{DME})_3]^{2+}$  ions, 2H–1T phase transition, and the fragmentation and structural distortion. The effect of  $[\text{Mg}(\text{DME})_3]^{2+}$  on the electrochemical performance of 2H- $\text{MoS}_2$ @C was assessed in different Mg electrolytes, such as MgBOR/DME, APC, and  $\text{Mg}(\text{HMDS})_2/\text{MgCl}_2/\text{AlCl}_3$ . The MgBOR/DME electrolyte enabled 2H- $\text{MoS}_2$ @C with the highest specific capacity of 95  $\text{mA h g}^{-1}$  at 50  $\text{mA g}^{-1}$ , in comparison with the APC (85  $\text{mA h g}^{-1}$ ) and  $\text{Mg}(\text{HMDS})_2/\text{MgCl}_2/\text{AlCl}_3$  (45  $\text{mA h g}^{-1}$ ) electrolytes. This work highlighted a new electrochemical method for boosting the efficient  $\text{Mg}^{2+}$  intercalation in  $\text{MoS}_2$ .

Several studies explored  $\text{MoS}_2$  as cathodes for AMBs, where  $\text{Al}^{3+}$  served as the intercalating species with the  $\text{AlCl}_3/\text{EMIMCl}$  electrolyte.<sup>111,178,179</sup> For example, Li *et al.*<sup>111</sup> reported that  $\text{MoS}_2$  spheres delivered a high specific capacity of 254  $\text{mA h g}^{-1}$  at 20  $\text{mA g}^{-1}$  in the initial cycle, but exhibited poor cyclability with

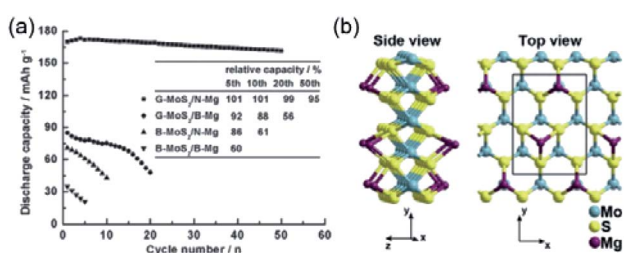


Fig. 20 (a) Typical cycling behaviour of the cells fabricated with B- $\text{MoS}_2$  or G- $\text{MoS}_2$  cathodes and bulk- or nanoparticles-Mg anodes with a discharge rate of 20  $\text{mA g}^{-1}$ . In the inset table, the relative capacity at a certain cycle refers to the ratio of the discharge capacity of the cells at the corresponding cycle to that at the first cycle. (b) Graphical illustrations of theoretically modelled Mg adsorption on  $\text{MoS}_2$  single-layered nanoribbon. Reprinted with permission from ref. 176. Copyright 2010 Wiley-VCH Verlag GmbH & Co. KGaA, Weinheim.

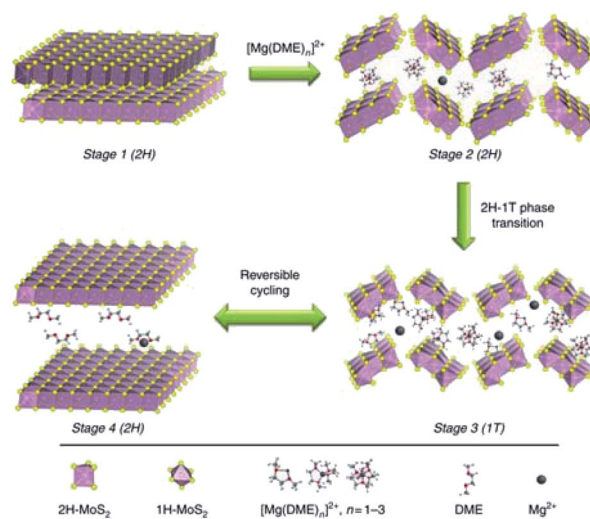


Fig. 21 Schematic illustration of the  $[\text{Mg}(\text{DME})_3]^{2+}$  storage mechanism in  $\text{MoS}_2$  structures with the MgBOR/DME electrolyte. Reprinted with permission from ref. 174. Copyright 2018, Springer Nature.

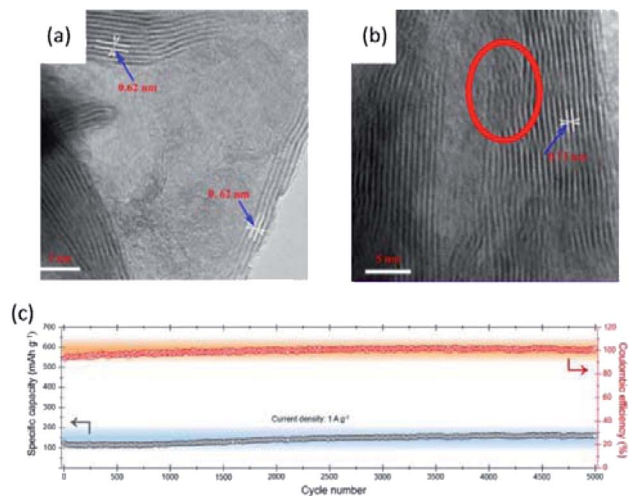


Fig. 22 TEM images of MoS<sub>2</sub> microspheres (a) before and (b) after cycling. Reprinted with permission from ref. 111. Copyright 2018 American Chemical Society. (c) The cycling performance and corresponding coulombic efficiency of MoSe<sub>2</sub>@C at 1 A g<sup>-1</sup>. Reprinted with permission from ref. 180. Copyright 2019 American Chemical Society.

67 mA h g<sup>-1</sup> retained after 100 cycles at 40 mA g<sup>-1</sup>. XRD spectra revealed that the intercalation of Al<sup>3+</sup> into MoS<sub>2</sub> spheres resulted in apparent interlayer expansion from 6.2 Å to 7.3 Å and obvious lattice stripe distortion (Fig. 22a and b). The XPS analysis showed that partial Al<sup>3+</sup> intercalation into the MoS<sub>2</sub> spheres was irreversible, which also accounted for the inferior cycling performance.

To further improve the electrochemical performance, MoS<sub>2</sub> and MoSe<sub>2</sub> were hybridized with carbon materials.<sup>178,180</sup> Yang *et al.*<sup>178</sup> fabricated MoS<sub>2</sub> nanostructure-incorporated free-standing carbon fibres through an electrospinning method. The highly conductive carbon fibres provided efficient encapsulation for MoS<sub>2</sub> nanostructures. The specific capacity of the carbon fiber-MoS<sub>2</sub> electrode achieved 293 mA h g<sup>-1</sup> in the initial cycle, and maintained 125 mA h g<sup>-1</sup> after 200 cycles at 100 mA g<sup>-1</sup>. Moreover, Zhao *et al.*<sup>180</sup> prepared MoSe<sub>2</sub>@C using a multistep synthetic route. First, dopamine hydrochloride as the carbon precursor was mixed with ammonium molybdate to create a homogenous mixture. Afterwards, the mixture was calcinated and selenized to obtain MoSe<sub>2</sub>@C. The MoSe<sub>2</sub>@C cathode for AMBs showed a high specific capacity of 267 mA h g<sup>-1</sup> at 100 mA g<sup>-1</sup> with no noticeable capacity fading for up to 5000 cycles at 1 A g<sup>-1</sup> (Fig. 22c). Interestingly, the specific capacities of both MoS<sub>2</sub> and MoSe<sub>2</sub> were higher than the theoretical value based on the intercalation mechanism. This phenomenon suggested that the conversion mechanism was involved in the charge-storage process.

### 3.3 Graphite-based materials

Graphite-based cathode materials are appealing due to the abundant resource, low cost, and environmental friendliness. The unique redox amphoteric feature allows graphite to host both cations (*e.g.*, Li<sup>+</sup>, K<sup>+</sup>, and Py<sub>14</sub><sup>+</sup>) and anions (*e.g.*, Br<sup>-</sup>, Cl<sup>-</sup>, BF<sub>4</sub><sup>-</sup>, FSI<sup>-</sup>, PF<sub>6</sub><sup>-</sup>, TFSI<sup>-</sup>, TOF<sup>-</sup>, and AlCl<sub>4</sub><sup>-</sup>). In particular, anion

intercalation into graphite occurs at a high potential (~1.75 V vs. SHE), which is beneficial for the construction of high-voltage energy storage devices.<sup>44,45,181</sup> Anion intercalation of graphite-based materials is based on a staging mechanism. The stage number represents the number of graphite layers between intercalating anions (Fig. 23).<sup>182</sup> Different intercalation stages can be detected by distinctive voltage plateau during charge/discharge and the spectroscopy analysis (*e.g.*, XRD and Raman). For example, the intercalation stage can be extracted from the peak position ratio of the two most dominant peaks, (00*n* + 1) and (00*n* + 2). Anion-intercalation graphite-based materials are widely employed to construct dual-ion MVMBs. During charging, metal cations are deposited on the anodes, and anions are intercalated into the graphite-based cathodes. Owing to the consumption of electrolyte ions, dual-ion batteries with graphite cathodes generally require the use of large-amount or high-concentration electrolytes.<sup>50</sup>

In contrast to ZMBs constructed with commonly used cathodes (*e.g.*, V<sub>2</sub>O<sub>5</sub> and MnO<sub>2</sub>), ZMBs based on the graphite cathodes (denoted graphite-ZMBs) can depict high average voltages of above 2 V. However, most organic electrolytes of ZMBs (*e.g.*, Zn(TfO)<sub>2</sub> and Zn(TFSI)<sub>2</sub> in ionic liquid) have low anodic stable potential windows (<2.6 V vs. Zn<sup>2+</sup>/Zn), which cannot fulfil the high potential requirement of anion intercalation into graphite.<sup>23,24,68,183</sup> For example, graphite-ZMBs charged to a cut-off voltage of 2.6 V vs. Zn<sup>2+</sup>/Zn only demonstrated a specific capacity of 50 mA h g<sup>-1</sup>.<sup>68</sup> Recently, Wang *et al.*<sup>24</sup> showed that adding LiPF<sub>6</sub> into the Zn electrolyte composed of Zn(TFSI)<sub>2</sub> in AN can greatly enhance the anodic stability. It was shown that 1 M Zn(TFSI)<sub>2</sub> in AN started to decompose at ~2.3 V vs. Zn<sup>2+</sup>/Zn. The presence of LiPF<sub>6</sub> efficiently suppressed the anodic dissolution and the decomposition of Zn(TFSI)<sub>2</sub> electrolyte. The mixed electrolyte (0.5 M Zn(TFSI)<sub>2</sub> + 2 M LiPF<sub>6</sub>) depicted a high stable potential of more than 4 V vs. Zn<sup>2+</sup>/Zn (Fig. 24a). The floating test at 3 V exhibited negligible leakage currents (<10<sup>-3</sup> mA cm<sup>-2</sup>), which contrasted with the high leakage currents of the 1 M Zn(TFSI)<sub>2</sub> electrolyte (>30 mA cm<sup>-2</sup>, Fig. 24b).<sup>19</sup> F NMR identified the co-intercalation of PF<sub>6</sub><sup>-</sup> and TFSI<sup>-</sup> into graphite during charging. Density functional theory (DFT) calculations

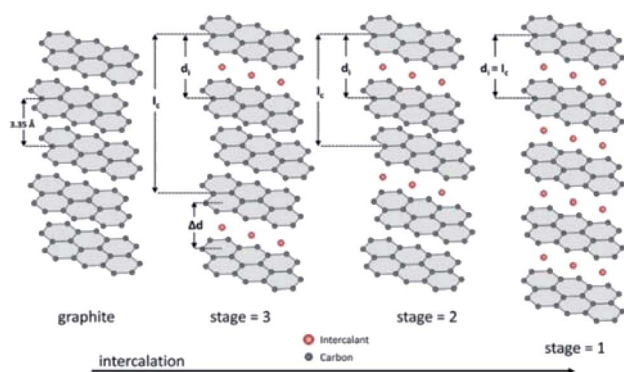


Fig. 23 Schematic illustration of the staging mechanism of intercalant guest species into graphite:  $l_c$  = periodic repeat distance;  $d_i$  = intercalant gallery height;  $\Delta d$  = gallery expansion. Reprinted with permission from ref. 182. Copyright 2013 Elsevier.



showed that  $\text{PF}_6^-$  had a lower diffusion energy barrier than  $\text{TFSI}^-$ , thus suggesting the higher diffusion rate of  $\text{PF}_6^-$  (Fig. 24c and d). Graphite-ZMB with the  $\text{LiPF}_6$  additive could be charged to a high voltage of 2.8 V vs.  $\text{Zn}^{2+}/\text{Zn}$ , depicting large specific capacities of 105 and 97  $\text{mA h g}^{-1}$  at 100 and 2000  $\text{mA g}^{-1}$ , respectively (Fig. 24e). In addition, the superior cyclability of graphite-ZMB was demonstrated with nearly 100% retention after 2000 cycles at 1000  $\text{mA g}^{-1}$ . Recently, Wang *et al.*<sup>23</sup> demonstrated that Zn metal would react with  $\text{PF}_6^-$ , forming dissolved  $\text{Zn}^{2+}$  in the electrolyte. The reaction between  $\text{PF}_6^-$  and Zn also led to the formation of a solid electrolyte interface on Zn, which was composed of  $\text{ZnF}_2$  and  $\text{LiF}$ . With an electrolyte of 2.5 M  $\text{LiPF}_6$  in EMC, graphite-ZMB exhibited a high specific capacity of 95  $\text{mA h g}^{-1}$  at 200  $\text{mA g}^{-1}$ . It is highly desirable to find alternative metal- $\text{PF}_6$  salts and avoid the use of Li salts.

AMBs are the most studied battery system with anion-intercalation graphite cathodes. Although the Al stripping and plating electrochemistry in the ionic liquid mixture containing  $\text{Al}_2\text{Cl}_7^-$  anions has been well known for several decades,<sup>99</sup> Dai *et al.*<sup>21</sup> was the first to show AMBs constructed with the  $\text{AlCl}_4^-$  intercalation graphite cathodes in 2015. The optimal AMBs were assembled in the electrolyte with an  $\text{AlCl}_4^-/\text{Al}_2\text{Cl}_7^-$  ratio of  $\sim 2.33$ , which was prepared by mixing  $\text{AlCl}_3$  and EMIMCl in a molar ratio of 1.3. The  $\text{AlCl}_4^-$ -intercalation chemistry allowed pyrolytic graphite with a specific capacity of 60  $\text{mA h g}^{-1}$  at 66  $\text{mA g}^{-1}$  and an average cell voltage of 2 V. However, the large size of  $\text{AlCl}_4^-$  anions led to the unsatisfactory rate capability (only 20  $\text{mA h g}^{-1}$  retained at 264  $\text{mA g}^{-1}$ ) of the pyrolytic graphite cathode. To address these issues, the graphitic foam was used to replace pyrolytic graphite, delivering a specific capacity of 60  $\text{mA h g}^{-1}$  at a high current density of 5  $\text{A g}^{-1}$ . More impressively, the pouch-cell batteries assembled with the graphitic foam cathodes achieved high capacity retention of 100% after 7500 cycles with high coulombic efficiencies ( $>97\%$ ).

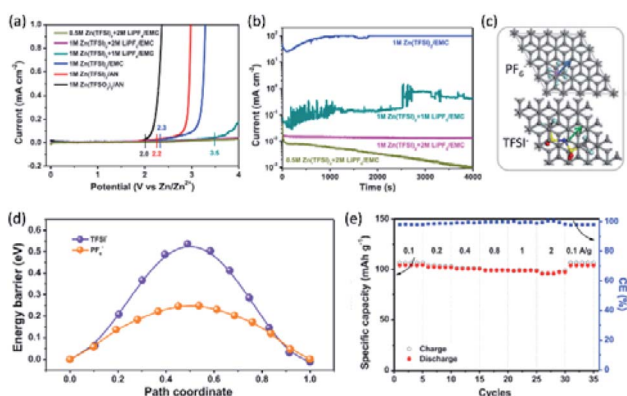


Fig. 24 (a) Linear sweep voltammetry curves at 2  $\text{mV s}^{-1}$  of different electrolytes on stainless steel electrode within Zn//stainless steel cells. (b) Floating test of electrolytes at 3 V. Sensitivity is 0.01  $\text{A V}^{-1}$ . (c) The optimized anion diffusion path in the graphite layers. (d) The optimized anion diffusion energy barriers in the graphite layers. (e) Rate performance of Zn//graphite dual-ion battery. Reprinted with permission from ref. 24. Copyright 2019 WILEY-VCH Verlag GmbH & Co. KGaA, Weinheim.

*Ex situ* XRD measurements provided significant insights into the  $\text{AlCl}_4^-$ -intercalation mechanism of graphite. In detail, the (002) peak of graphite vanished in the fully charged cathode, while two new peaks, assigned to lattice spacings of 3.15 and 3.77 Å, appeared. In the fully discharged cathode, the graphite (002) peak reappeared with a broad shoulder, which was indicative of an irreversible change in the stacking of graphite layers.  $\text{AlCl}_4^-$  intercalation into graphite was determined to be a stage-4 process. Besides, the same group also found that free-standing natural graphite film employed as the AMB cathode depicted superior cyclability ( $\sim 100\%$  retention after 6000 cycles), good coulombic efficiencies ( $\sim 98\%$ ), and importantly considerably enhanced specific capacity (110  $\text{mA h g}^{-1}$  at 99  $\text{mA g}^{-1}$ ).<sup>113</sup>

To further improve the rate performance,  $\text{AlCl}_4^-$ -intercalated graphite was subjected to rapid thermal expansion at 1000 °C and subsequently transferred to water for electrolysis.<sup>112</sup> The electrolysis process produced massive amounts of hydrogen gas, which further introduced large porosity into the expanded graphite. The obtained porous graphite was comprised of microparticles ( $\sim 1 \mu\text{m}$ ) with 4–5 graphene layers, presenting superior rate performance with a specific capacity of 60  $\text{mA h g}^{-1}$  at 12  $\text{A g}^{-1}$  (18 seconds charge). Moreover, Zhang *et al.*<sup>184</sup> studied the  $\text{AlCl}_4^-$ -intercalation behaviours of four different graphitic materials, namely, large-size graphite (L-graphite) and graphene (L-graphene), small-size graphite (S-graphite) and graphene (S-graphene). At a low current density of 60  $\text{mA g}^{-1}$ , the specific capacities of L-graphite and L-graphene were both  $\sim 85 \text{ mA h g}^{-1}$  with two apparent voltage plateaus. In contrast, S-graphite and S-graphene showed a relatively low specific capacity of  $\sim 72 \text{ mA h g}^{-1}$  without distinctive voltage plateaus. In addition, L-graphene showed the best rate capability among four samples, retaining 90% of the initial capacity at a large current density of 4.8  $\text{A g}^{-1}$  (Fig. 25a). The excellent rate capability originated from both the high conductivity and structural flexibility of L-graphene, which could well endure the structural stress during the repeat  $\text{AlCl}_4^-$  intercalation/deintercalation (Fig. 25b). Interestingly, the good crystallinity of graphitic materials contributed to the high specific capacity of L-graphite. The carboxyl and hydroxyl groups on the edge of S-graphene caused the repulsive interaction with the intercalating  $\text{AlCl}_4^-$ , thus imposing a specific

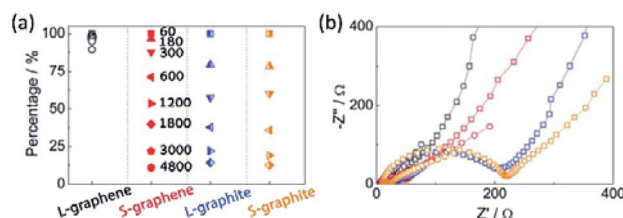


Fig. 25 (a) Rate capability from 60 to 4800  $\text{mA h g}^{-1}$  of L-graphene (black), S-graphene (red), L-graphite (blue), and S-graphite (orange). (b) Electrochemical impedance spectra (circle represents high voltage and square represents low voltage). Reprinted with permission from ref. 184. Copyright 2017 WILEY-VCH Verlag GmbH & Co. KGaA, Weinheim.

activation energy for  $\text{AlCl}_4^-$ -intercalation.<sup>184,185</sup> In addition, slight performance degradation was detected for L-graphene during the continuous charge/discharge cycles, which significantly contrasted with the notable performance degradation of S-graphene caused by the apparent structural change.<sup>184</sup>

High-performance cathodes relying on simple and robust preparation methods are highly pursued for practical applications. In this regard, Hu *et al.*<sup>186</sup> reported a simple acid treatment strategy, which greatly improved the rate performance of commercial carbon nanofibers (CNFs). The acid treatment cleaved the outer graphitic layer of CNFs, creating edge-rich graphitic nanoribbons interconnected by the nanofiber core (Fig. 26a). In the original CNFs, the intercalation of  $\text{AlCl}_4^-$  was blocked due to the dense outer wrapping graphite layer. By contrast, the inner graphitic carbon was sufficiently exposed after the cleavage of the outer layer, enabling the superior  $\text{AlCl}_4^-$ -intercalation kinetics (Fig. 26b). In addition, the cleaved nanoribbons increased the charge-transport capability of the

electrode by serving as conductive ties to link the stacked nanofibers. Raman spectra confirmed that the graphitic structure of the cleaved nanoribbons was not destroyed by the acid treatment. Additionally, the acid treatment increased the specific surface area from  $23.2 \text{ m}^2 \text{ g}^{-1}$  for the pristine CNFs to  $55.3 \text{ m}^2 \text{ g}^{-1}$  for the cleaved CNFs. DFT calculations suggested that the edge-rich graphene structure (2.45 eV) had a stronger binding with  $\text{AlCl}_4^-$  than the edge-less graphene structure (2.21 eV). Furthermore, the  $\text{AlCl}_4^-$  binding energies in the bilayer structures are  $-3.14 \text{ eV}$ ,  $-1.66 \text{ eV}$ , and  $-1.17 \text{ eV}$  for the edge-less graphene, the centre of edge-rich graphene, and the edge of edge-rich graphene, respectively (Fig. 26c–h). These calculation results supported that the intercalation of  $\text{AlCl}_4^-$  was preferred with edge-rich graphene. This conclusion was also consistent with a recent study,<sup>187</sup> disclosing that the voids in few-layers graphene promoted the stage-2 and stage-1  $\text{AlCl}_4^-$  intercalation. After the acid treatment, the cleaved CNFs presented a high specific capacity of  $126 \text{ mA h g}^{-1}$  at  $1 \text{ A g}^{-1}$ , which significantly contrasted with the pristine CNFs ( $15 \text{ mA h g}^{-1}$ ). Besides, excellent rate performance and cyclability were demonstrated for the cleaved CNFs with high specific capacities of  $95 \text{ mA h g}^{-1}$  at  $50 \text{ A g}^{-1}$  and  $105 \text{ mA h g}^{-1}$  ( $\sim 100\%$  retention) after 5000 cycles at  $10 \text{ A g}^{-1}$  (Fig. 26i and j).

As discussed earlier, low-cost amides or amines can be used to replace the ionic liquid in the AMB electrolytes. For example, mixing  $\text{AlCl}_3$  with urea,<sup>105</sup> triethylamine hydrochloride ( $\text{Et}_3\text{NCl}$ ),<sup>188</sup> or acetamide<sup>104</sup> can form  $\text{AlCl}_4^-$ ,  $\text{AlCl}_2^+$ , and  $\text{Al}_2\text{Cl}_7^-$  in electrolytes. The charge/discharge electrode reaction in the  $\text{AlCl}_3$ /urea electrolyte is the same as in the  $\text{AlCl}_3$ /EMIMCl electrolyte, involving the  $\text{Al}_2\text{Cl}_7^-$  reaction (eqn (3)) at the anode side and  $\text{AlCl}_4^-$  intercalation at the cathode side.<sup>104</sup> However, the high viscosity of  $\text{AlCl}_3$ /urea led the graphite cathode in the  $\text{AlCl}_3$ /urea electrolyte to exhibit poor performance.<sup>105</sup> The specific capacity decreased from  $73 \text{ mA h g}^{-1}$  at  $100 \text{ mA g}^{-1}$  to  $50 \text{ mA h g}^{-1}$  at  $200 \text{ mA g}^{-1}$ . In addition, the average discharge voltage of graphite in the  $\text{AlCl}_3$ /urea electrolyte was  $1.73 \text{ V}$ , which was  $0.27 \text{ V}$  lower than the graphite cathode in the  $\text{AlCl}_3$ /EMIMCl electrolyte. To overcome the viscosity issue, Xu *et al.*<sup>188</sup> showed a device combining the  $\text{Et}_3\text{NAlCl}_4$  electrolyte and the graphene aerogel cathode. The cathode was fabricated through freeze-drying and subsequent annealing of graphene oxide. In spite of the high viscosity of the electrolyte, the favourable porosity of the graphene aerogel cathode enabled an excellent rate performance. A specific capacity of nearly  $110 \text{ mA h g}^{-1}$  was reached at a current density of  $5 \text{ A g}^{-1}$ . Besides, the graphene aerogel was charged to a high voltage due to the high cut-off voltage of the  $\text{Et}_3\text{NAlCl}_4$  electrolyte ( $2.62 \text{ V}$ ). Charging the graphene aerogel to  $2.51 \text{ V}$  resulted in a high energy density of  $\sim 260 \text{ W h kg}^{-1}$  at a power density of  $3 \text{ kW kg}^{-1}$ . Nevertheless, Al-based dual-ion batteries require further electrolyte development to improve the anodic stability, as no commercial current collector can be used for the cathodes.

Anion intercalation provides a good strategy to avoid the drawback associated with the intercalation of multivalent  $\text{Zn}^{2+}$ ,  $\text{Mg}^{2+}$ , and  $\text{Al}^{3+}$ . In addition, the anion-intercalation chemistry has been extensively studied in  $\text{Li}^+$ -based systems, which accumulate insightful experience for constructing MVMB devices. In

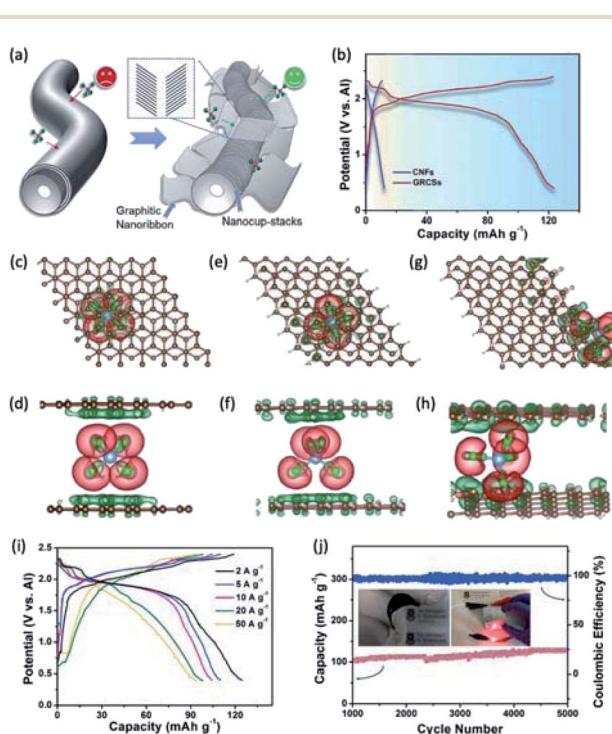


Fig. 26 (a) Schematic comparison of anion intercalation/deintercalation in commercial CNFs and cleaved CNFs. (b) Representative charge/discharge curves of CNFs and cleaved CNFs. (c–h) Calculated charge density differences of the  $\text{AlCl}_4^-$  in different graphene structures: the (c) top and (d) side views of the bilayer edge-less graphene with one  $\text{AlCl}_4^-$  ion placed between the two layers; the (e) top and (f) side views of the bilayer edge-rich graphene with one  $\text{AlCl}_4^-$  ion placed in the middle area; and the (g) top and (h) side views of bilayer edge-rich graphene with one  $\text{AlCl}_4^-$  ion placed near the edge, between two layers. An isosurface level of  $0.0007 \text{ e}\text{\AA}^{-3}$  has been used in all images. (i) Charge/discharge curves of cleaved-CNFs at current densities from 2 to  $50 \text{ A g}^{-1}$ . (j) Long-term stability of cleaved-CNFs with coulombic efficiency and discharge specific capacity versus the cycle number at a current density of  $10 \text{ A g}^{-1}$ . The inset in d shows a flexible cleaved-CNFs electrode and a flexible AIB lighting a light emitting diode. Reproduced from ref. 186 with permission from The Royal Society of Chemistry.

this direction, the development of suitable electrolytes with wide stable potential windows and efficient metal stripping and plating will be highly desired for MVMBs.

### 3.4 Two-dimensional covalent organic frameworks

Two-dimensional covalent organic frameworks are a class of crystalline and porous 2D polymers, which are constructed with dynamic covalent bonds in the layer and stacked by non-covalent aromatic  $\pi$ -interactions. Interestingly, 2D COFs are equipped with one-dimensional channels along the  $c$ -crystallographic direction, allowing efficient mass transport through the material. Recently, 2D COFs have attracted intensive research attention as a group of multifunctional materials.<sup>189–192</sup> Importantly, the regular porosity, large specific surface area, and the tailorable chemistries/topologies empower 2D COFs with versatile opportunities for energy storage by periodically organizing redox-active sites into porous frameworks.<sup>193</sup> According to the redox potentials, many organic groups are potentially suitable for constructing redox-active 2D COFs, such as quinone,<sup>194–200</sup> phenazine,<sup>201,202</sup> triphenylamine,<sup>203,204</sup> cyano,<sup>205,206</sup> bipyridine,<sup>114,207</sup> pyridinic nitrogen,<sup>208</sup> and phenanthrenequinone.<sup>20,110,209</sup> At present, the energy-storage investigation on 2D COFs is still at the primary stage, and basic electrochemistry understanding is accumulating with dominant efforts devoted to the exploration of 2D COFs for LIBs. It should be noted that the electrochemical behaviours of organic groups are expected to be quite different for the applications of LIBs and MVMBs due to the change of charge carrier ions. For example, hexaazatriphenylene was demonstrated to exhibit a high specific capacity of  $\sim 400$  mA h  $g^{-1}$  for  $Li^+$  storage based on the accommodation of two  $Li^+$  ions in each bipyridine site. In the case of  $Mg^{2+}$  storage, two bipyridine sites would accommodate only one  $Mg^{2+}$ , displaying inferior capacity and rate performance.<sup>114</sup>

Recently, some pioneering studies attempted to demonstrate the application of 2D COFs in MVMBs. Distinct from inorganic

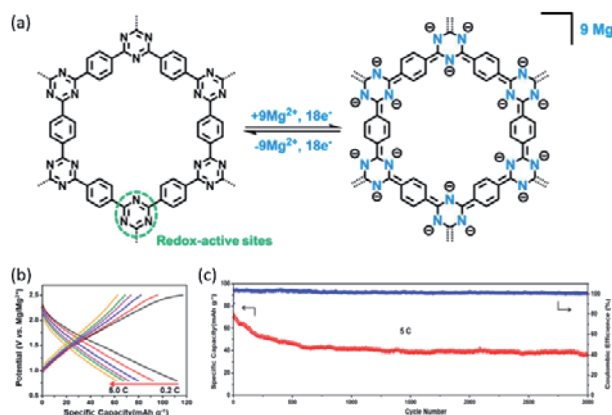


Fig. 27 (a) Chemical structure and possible electrochemical redox mechanism of the triazine-based COF. (b) Discharge/charge curves of electrodes at different rates. (c) Long-term cycling performance of the 2D COF at 5C. Reprinted with permission from ref. 208. Copyright 2019 American Chemical Society.

cathodes for MVMBs, 2D COFs provide flexible  $Mg^{2+}$  diffusion pathways and superior electrochemical reaction kinetics. Recently, Sun *et al.*<sup>208</sup> synthesized a triazine-based 2D COF for  $Mg^{2+}$  storage (Fig. 27a). The 2D COF was synthesized through the polymerization of 1,4-dicyanobenzene by annealing with  $ZnCl_2$  at 400 °C. An impressive rate performance was exemplified with a specific capacity of 110 mA h  $g^{-1}$  and more than 50% capacity retention when the current density was increased from 50 to 1300 mA  $g^{-1}$  (Fig. 27b). In addition, the 2D COF presented impressive cyclability, retaining a specific capacity of  $\sim 40$  mA h  $g^{-1}$  after 5000 cycles at 1300 mA  $g^{-1}$  (Fig. 27c). Based on the proposed structure in Fig. 27a, the high density of active triazine sites enabled the 2D COF with a high theoretical specific capacity of 419 mA h  $g^{-1}$ , considerably higher than the measured value (110 mA h  $g^{-1}$ ). XPS measurements detected changes in the signal of pyridinic-N in triazine during charge/discharge, indicating that charge storage occurred through interaction between  $Mg^{2+}$  and  $-C=N-$  in triazine rings. However, pyrrolic-N and graphitic-N could not contribute to the charge storage, which explained the low specific capacity.

Apart from cation-storage 2D COFs, anion-storage 2D COFs were also demonstrated for MVMBs, which delivered high voltage and large specific capacity. Lu *et al.*<sup>210</sup> synthesized a bipyridine-containing COF (denoted TpBpy-COF) through the reaction between 5,5'-diamino-2,2'-bipyridine and triformylphloroglucinol (Fig. 28a). Importantly, TpBpy-COF exhibited a high crystallinity with a large specific surface area of 1794  $m^2 g^{-1}$  and regular porosity with pore sizes of  $\sim 2.1$  nm. The TpBpy-COF cathode for AMBs exhibited an exceptionally high specific capacity of 307 mA h  $g^{-1}$  at 125 mA  $g^{-1}$  (Fig. 28b), close to its theoretical value of 369.7 mA h  $g^{-1}$ . Additionally, a high specific capacity of 150 mA h  $g^{-1}$  was retained after 13 000 cycles at a high current density of 2 A  $g^{-1}$ . *Ex situ* XRD reflected that TpBpy-COF well retained its crystalline structure during repeat

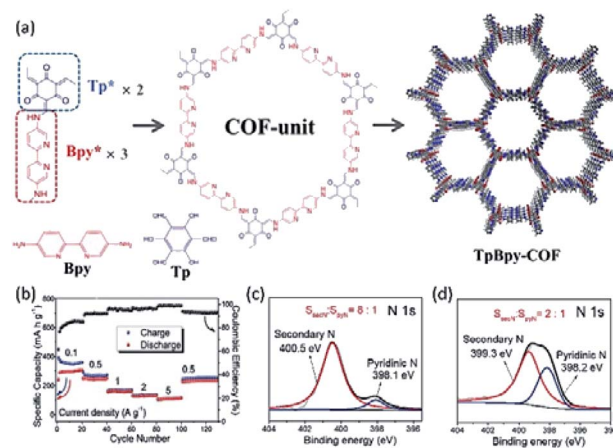


Fig. 28 (a) Synthetic reaction and structure illustration of 2D COF fabricated from 5,5'-diamino-2,2'-bipyridine and triformylphloroglucinol. (b) Galvanostatic discharge/charge curves under different current densities in the potential range 0.01–2.3 V. 1 s XPS spectra of electrodes (c) charged to 2.3 V and (d) discharged to 0.1 V at 2 A  $g^{-1}$ . Reprinted with permission from ref. 210. Copyright 2020 WILEY-VCH Verlag GmbH & Co. KGaA, Weinheim.



Table 2 Summary of layered cathode materials for non-aqueous ZMBs<sup>a</sup>

Material	Electrolyte	Specific capacity	Average discharge voltage	Energy density based on the cathode	Cyclability	Ref.
Bilayered hydrated V <sub>2</sub> O <sub>5</sub>	0.5 M Zn(TFSI) <sub>2</sub> in AN	196 mA h g <sup>-1</sup> at 14.4 mA g <sup>-1</sup>	0.9 V	176 W h kg <sup>-1</sup>	170 mA h g <sup>-1</sup> after 120 cycles at 14.4 mA g <sup>-1</sup>	65
V <sub>3</sub> O <sub>7</sub> ·H <sub>2</sub> O nanofibers	0.25 M Zn(OTf) <sub>2</sub> in AN	175 mA h g <sup>-1</sup> at 5 mA g <sup>-1</sup>	0.75 V	131 W h kg <sup>-1</sup>	175 mA h g <sup>-1</sup> after 50 cycles at 5 mA g <sup>-1</sup>	61
δ-MnO <sub>2</sub> nanoflorets	0.5 M Zn(TFSI) <sub>2</sub> in AN with 10% water	123 mA h g <sup>-1</sup> at 12.3 mA g <sup>-1</sup>	1.37 V	169 W h kg <sup>-1</sup>	55 mA h g <sup>-1</sup> after 125 cycles at 12.3 mA g <sup>-1</sup>	66
PPy-intercalated VOPO <sub>4</sub>	1 M Zn(OTf) <sub>2</sub> in AN	67 mA h g <sup>-1</sup> at 30 mA g <sup>-1</sup>	1.3 V	87 W h kg <sup>-1</sup>	60 mA h g <sup>-1</sup> after 350 cycles at 100 mA g <sup>-1</sup>	59
Natural graphite	0.2 M Zn(OTf) <sub>2</sub> in EMImOTf	33.7 mA h g <sup>-1</sup> at 200 mA g <sup>-1</sup>	2.0 V	65.1 W h kg <sup>-1</sup>	20 mA h g <sup>-1</sup> after 100 cycles at 200 mA g <sup>-1</sup>	183
Graphite powder	2 M LiPF <sub>6</sub> + 0.5 M Zn(TFSI) <sub>2</sub> in EMC	105 mA h g <sup>-1</sup> at 100 mA g <sup>-1</sup>	2.2 V	231 W h kg <sup>-1</sup>	96 mA h g <sup>-1</sup> after 2000 cycles at 1 A g <sup>-1</sup>	24
Natural graphite	2.5 M LiPF <sub>6</sub> in EMC/TMS (4 : 1)	98 mA h g <sup>-1</sup> at 100 mA g <sup>-1</sup>	2.2 V	216 W h kg <sup>-1</sup>	82 mA h g <sup>-1</sup> after 1200 cycles at 300 mA g <sup>-1</sup>	23

<sup>a</sup> TMS – tetramethylene sulfone.

charge/discharge cycles, accounting for the excellent cyclability. Furthermore, Fourier-transform infrared measurements suggested that AlCl<sub>4</sub><sup>-</sup> storage altered the environment of nitrogen atoms ( $\nu_{\text{C}=\text{N}}$  and  $\nu_{\text{C}-\text{N}}$  signals) in TpBpy-COF upon charging. N 1s peak related to the secondary N (-NH-) shifted from 399.2 eV to higher binding energy of 400.5 eV upon the charge, and shifted back to 399.3 eV after the discharge. Meanwhile, the ratio between secondary N and pyridinic N changed from 1 : 1 to 8 : 1 upon the charge and recovered to 2 : 1 after the discharge (Fig. 28c and d). These XPS results indicated that the C-N and C=N groups were involved in the p-type oxidation with AlCl<sub>4</sub><sup>-</sup>.<sup>210</sup>

## 4. Summary and outlook

To sum up, MVMBs, using highly available multivalent metal as anodes, have emerged as promising alternatives for LIBs, particularly in large-scale and stationary energy storage applications. Currently, MVMBs are still at the preliminary research stage, and the whole community focuses on exploiting suitable “anode–electrolyte–cathode” systems for potential practical applications. In this review, we briefly introduced the cell configuration and the so-far developed “anode–electrolyte” chemistries for non-aqueous MVMBs, including ZMBs, MMBs, and AMBs. Particularly, we put the emphasis on discussing the recent progress in the development of layered cathode materials (including layered TMOs, TMDs, graphite, and 2D COFs) for non-aqueous MVMBs (also summarized in Tables 2–4). It should be noted that Ca-metal batteries are also promising alternative MVMBs. However, the development of Ca metal-compatible electrolytes is still the main challenge of Ca-metal batteries, resulting in rare studies on the Ca<sup>2+</sup> intercalation of layered materials.<sup>211</sup> Therefore, Ca-metal batteries are not discussed in this review. Among layered materials, layered TMOs (e.g., MnO<sub>2</sub> and V<sub>2</sub>O<sub>5</sub>) demonstrate auspicious specific capacities and redox potentials, but display sluggish multivalent

metal ion-storage kinetics (e.g., Zn<sup>2+</sup> and Al<sup>3+</sup>) and compatibility issues with MVMB electrolytes (e.g., MMB electrolytes). In comparison with TMOs, TMDs show good electrolyte compatibility with efficient cation intercalation and superior rate capabilities. Nevertheless, inferior discharge voltages lead to the low energy densities of MVMBs constructed with TMD cathodes. Graphite-based materials with the anion-intercalation chemistry exhibit high redox potentials (e.g., ~1.75 V vs. SHE), avoiding the drawbacks related to multivalent metal ion intercalation. However, graphite-based materials are limited by the low theoretical capacity, as well as the insufficient electrolyte studies for ZMBs and MMBs. In addition, 2D COFs provide a unique material platform for exceptional active site engineering at the molecular level, providing many opportunities for both cation and anion storage. Fig. 29 compares the average discharge voltages and specific capacities of recently developed layered cathodes for ZMBs, MMBs, and AMBs. It provides an unambiguous picture about the advantages and limitations of different layered materials for different MVMBs. In light of the unique vdW interaction between layers, the structure of layered materials can be easily engineered *via* versatile strategies to tailor their intrinsic properties and ion-storage kinetics. In this sense, interlayer expansion strategies represent the most employed one to facilitate the efficient ion diffusion and promote the intercalation of new charge carrier species (e.g., MgCl<sup>+</sup> in MMBs). Besides, guest species incorporation strategies can enhance the intrinsic conductivity and structural stability of layered materials, while imposing a shielding effect on the interaction of charge carrier ions and cathodes. Given the remarkable progress achieved in this research direction, there are many challenges to be addressed in the near future, which are highlighted below.

Although many material engineering strategies have been reported to modify the structures of layered materials, their side effects on the electrochemical performance were not adequately addressed in the previous studies. For example, guest species

Table 3 Summary of layered cathode materials for MMBs<sup>a</sup>

Material	Electrolyte	Specific capacity	Average discharge voltage	Energy density based on the cathode	Cyclability	Ref.
V <sub>2</sub> O <sub>5</sub> on CNFs	1 M Mg(ClO <sub>4</sub> ) <sub>2</sub> in AN	160 mA h g <sup>-1</sup> at 20 mA g <sup>-1</sup>	0.6 V	96 W h kg <sup>-1</sup>	120 mA h g <sup>-1</sup> after 50 cycles at 30 mA g <sup>-1</sup>	136
α-V <sub>2</sub> O <sub>5</sub>	0.5 M Mg(TFSI) <sub>2</sub> in PY <sub>14</sub> TFSI	295 mA h g <sup>-1</sup> at 15 mA g <sup>-1</sup> (110 °C)	0.0 V vs. AC (2.0 V vs. Mg <sup>2+</sup> /Mg)	N/A	200 mA h g <sup>-1</sup> after 50 cycles at 59 mA g <sup>-1</sup> (110 °C)	93
V <sub>2</sub> O <sub>5</sub> -PEO nanocomposites	0.5 M Mg(ClO <sub>4</sub> ) <sub>2</sub> in AN	100 mA h g <sup>-1</sup> at 10 mA g <sup>-1</sup>	~1.4 V	~140 W h kg <sup>-1</sup>	90 mA h g <sup>-1</sup> after 35 cycles at 10 mA g <sup>-1</sup>	141
Graphene-decorated V <sub>2</sub> O <sub>5</sub>	0.5 M Mg(TFSI) <sub>2</sub> in AN	320 mA h g <sup>-1</sup> at 50 mA g <sup>-1</sup>	-0.4 V vs. AC (2.0 V vs. Mg <sup>2+</sup> /Mg)	N/A	95 mA h g <sup>-1</sup> after 200 cycles at 1 A g <sup>-1</sup>	132
V <sub>3</sub> O <sub>7</sub> ·H <sub>2</sub> O NWs	0.5 M Mg(ClO <sub>4</sub> ) <sub>2</sub> in AN	231 mA h g <sup>-1</sup> at 10 mA g <sup>-1</sup> (at 60 °C)	-0.75 V vs. AC (1.75 V vs. Mg <sup>2+</sup> /Mg)	N/A	132 mA h g <sup>-1</sup> after 100 cycles at 40 mA g <sup>-1</sup> (60 °C)	142
NH <sub>4</sub> V <sub>4</sub> O <sub>10</sub>	0.5 M Mg(ClO <sub>4</sub> ) <sub>2</sub> in AN	174.8 mA h g <sup>-1</sup> at 42 mA g <sup>-1</sup>	-0.19 V vs. AC (2.19 V vs. Mg <sup>2+</sup> /Mg)	N/A	36.8 mA h g <sup>-1</sup> after 100 cycles at 210 mA g <sup>-1</sup>	140
Mn <sub>0.04</sub> V <sub>2</sub> O <sub>5</sub> ·1.17H <sub>2</sub> O NBs	0.3 M Mg(TFSI) <sub>2</sub> in AN	140 mA h g <sup>-1</sup> at 50 mA g <sup>-1</sup>	-0.2 V vs. AC (2.2 V vs. Mg <sup>2+</sup> /Mg)	N/A	70 mA h g <sup>-1</sup> after 10 000 cycles at 2 A g <sup>-1</sup>	138
Mg <sub>0.3</sub> V <sub>2</sub> O <sub>5</sub> ·1.1H <sub>2</sub> O NWs	0.3 M Mg(TFSI) <sub>2</sub> in AN	162 mA h g <sup>-1</sup> at 100 mA g <sup>-1</sup>	-0.25 V vs. AC (2.25 V vs. Mg <sup>2+</sup> /Mg)	N/A	108 mA h g <sup>-1</sup> after 10 000 cycles at 1 A g <sup>-1</sup>	135
Mg <sub>x</sub> V <sub>5</sub> O <sub>12</sub> ·nH <sub>2</sub> O NFs	0.3 M Mg(TFSI) <sub>2</sub> in AN	160 mA h g <sup>-1</sup> at 50 mA g <sup>-1</sup>	0.0 V vs. AC (2.0 V vs. Mg <sup>2+</sup> /Mg)	N/A	68 mA h g <sup>-1</sup> after 10 000 cycles at 2 A g <sup>-1</sup>	137
Na <sub>2</sub> V <sub>6</sub> O <sub>16</sub> ·1.63H <sub>2</sub> O NWs	0.5 M Mg(TFSI) <sub>2</sub> in DME	175 mA h g <sup>-1</sup> at 50 mA g <sup>-1</sup>	-0.4 V vs. AC (2.0 V vs. Mg <sup>2+</sup> /Mg)	N/A	46 mA h g <sup>-1</sup> after 450 cycles at 200 mA g <sup>-1</sup>	139
Free-standing MnO <sub>2</sub> NWs film	0.1 M Mg(ClO <sub>4</sub> ) <sub>2</sub> in PC	120 mA h g <sup>-1</sup> at 246 mA g <sup>-1</sup>	N/A	N/A	92 mA h g <sup>-1</sup> after 100 cycles at 246 mA g <sup>-1</sup>	128
MnO <sub>2</sub>	0.25 M Mg(TFSI) <sub>2</sub> in diglyme	135 mA h g <sup>-1</sup> at 25 mA g <sup>-1</sup>	1.4 V	N/A	90 mA h g <sup>-1</sup> after 100 cycles at 125 mA g <sup>-1</sup>	95
MoO <sub>3</sub>	0.5 M Mg(ClO <sub>4</sub> ) <sub>2</sub> in AN	220 mA h g <sup>-1</sup> at N/A	1.8 V	N/A	N/A	221
PA-VOPO <sub>4</sub>	APC in THF	275 mA h g <sup>-1</sup> at 100 mA g <sup>-1</sup>	1 V	275 W h kg <sup>-1</sup>	192 mA h g <sup>-1</sup> after 500 cycles at 100 mA g <sup>-1</sup>	153
VOPO <sub>4</sub> ·2H <sub>2</sub> O	0.1 M Mg(ClO <sub>4</sub> ) <sub>2</sub> ·6H <sub>2</sub> O in PC	91.7 mA h g <sup>-1</sup> at 5 mA g <sup>-1</sup>	0.1 V vs. Ag/AgCl (2.7 V vs. Mg <sup>2+</sup> /Mg)	N/A	N/A	152
TiS <sub>2</sub> nanotubes	1 M Mg(ClO <sub>4</sub> ) <sub>2</sub> in AN	236 mA h g <sup>-1</sup> at 10 mA g <sup>-1</sup>	1.2 V	N/A	184 mA h g <sup>-1</sup> after 80 cycles at 10 mA g <sup>-1</sup>	159
TiSe <sub>2</sub> nanocrystal	0.25 M Mg(AlCl <sub>2</sub> EtBu) <sub>2</sub> in THF	110 mA h g <sup>-1</sup> at 5 mA g <sup>-1</sup>	0.9 V	99 W h kg <sup>-1</sup>	~100 mA h g <sup>-1</sup> after 50 cycles at 5 mA g <sup>-1</sup>	158
TiS <sub>2</sub>	APC in tetraglyme	160 mA h g <sup>-1</sup> at 12.5 mA g <sup>-1</sup> (60 °C)	~0.7 V	~112 W h kg <sup>-1</sup>	~115 mA h g <sup>-1</sup> after 40 cycles at 25 mA g <sup>-1</sup> (60 °C)	160
Layer-expanded TiS <sub>2</sub>	APC in THF with 0.25 M Py <sub>14</sub> Cl	239 mA h g <sup>-1</sup> at 24 mA g <sup>-1</sup>	0.7 V	176 W h kg <sup>-1</sup>	120 mA h g <sup>-1</sup> after 500 cycles at 240 mA g <sup>-1</sup>	154
Pristine TiSe <sub>2</sub>	APC in THF	127 mA h g <sup>-1</sup> at 5 mA g <sup>-1</sup>	1.25 V	159 W h kg <sup>-1</sup>	80 mA h g <sup>-1</sup> after 40 cycles at 5 mA g <sup>-1</sup>	157
Pristine VSe <sub>2</sub>	APC in THF	115 mA h g <sup>-1</sup> at 5 mA g <sup>-1</sup>	1.2 V	138 W h kg <sup>-1</sup>	86 mA h g <sup>-1</sup> after 40 cycles at 5 mA g <sup>-1</sup>	157
2-Ethylhexylamine pillared VS <sub>2</sub> nanoflowers	Mg(HMDS) <sub>2</sub> -4MgCl <sub>2</sub> in THF with PP <sub>14</sub> TFSI	249 mA h g <sup>-1</sup> at 100 mA g <sup>-1</sup>	0.7 V	174 W h kg <sup>-1</sup>	90 mA h g <sup>-1</sup> after 600 cycles at 1 A g <sup>-1</sup>	167
VS <sub>2</sub> NSs	APC in THF with 0.2 M PP <sub>14</sub> Cl	348 mA h g <sup>-1</sup> at 100 mA g <sup>-1</sup>	0.7 V	244 W h kg <sup>-1</sup>	200 mA h g <sup>-1</sup> after 300 cycles at 1 A g <sup>-1</sup>	80
Graphene-like MoS <sub>2</sub>	Mg(AlCl <sub>3</sub> Bu) <sub>2</sub> in THF	170 mA h g <sup>-1</sup> at 20 mA g <sup>-1</sup>	1.9 V	323 W h kg <sup>-1</sup>	162 mA h g <sup>-1</sup> after 50 cycles at 20 mA g <sup>-1</sup>	176
MoS <sub>2</sub> @C porous NRs	Fluorinated Mg alkoxyborate	120 mA h g <sup>-1</sup> at 10 mA g <sup>-1</sup>	0.65 V	80 W h kg <sup>-1</sup>	56 mA h g <sup>-1</sup> after 200 cycles at 100 mA g <sup>-1</sup>	174
PVP-incorporated MoS <sub>2</sub>	APC in THF	143.4 mA h g <sup>-1</sup> at 20 mA g <sup>-1</sup>	~0.75 V	~108 W h kg <sup>-1</sup>	131.9 mA h g <sup>-1</sup> after 100 cycles at 20 mA g <sup>-1</sup>	177
Expanded graphite	0.5 M Mg(TFSI) <sub>2</sub> in Py <sub>14</sub> TFSI	93 mA h g <sup>-1</sup> at 100 mA g <sup>-1</sup>	1.83 V	174 W h kg <sup>-1</sup>	62 mA h g <sup>-1</sup> after 500 cycles at 300 mA g <sup>-1</sup>	212
Triazine-based porous COF	0.5 M Mg(TFSI) <sub>2</sub> in DME	102 mA h g <sup>-1</sup> at 57 mA g <sup>-1</sup>	1.45 V	146 W h kg <sup>-1</sup>	30 mA h g <sup>-1</sup> after 3000 cycles at 570 mA g <sup>-1</sup>	208

<sup>a</sup> NFs – nanofibers, NW – nanowire, AC – active carbon, NB – nanobelts, NS – nanosheet, NR – nanorod.

Table 4 Summary of layered cathode materials for AMBs<sup>a</sup>

Material	Electrolyte	Specific capacity	Average discharge voltage	Energy density based on the cathode	Cyclability	Ref.
V <sub>2</sub> O <sub>5</sub> NWs	AlCl <sub>3</sub> : [EMIm]Cl molar ratio 1.1 : 1	305 mA h g <sup>-1</sup> at 125 mA g <sup>-1</sup>	0.55 V	168 W h kg <sup>-1</sup>	273 mA h g <sup>-1</sup> after 20 cycles at 125 mA g <sup>-1</sup>	143
Binder-free V <sub>2</sub> O <sub>5</sub>	AlCl <sub>3</sub> : [BMIm]Cl molar ratio 1.1 : 1	239 mA h g <sup>-1</sup> at 44.2 mA g <sup>-1</sup>	0.6 V	143 W h kg <sup>-1</sup>	N/A	213
V <sub>2</sub> O <sub>5</sub> NWs	AlCl <sub>3</sub> : [BMIm]Cl molar ratio 1.1 : 1	107 mA h g <sup>-1</sup> at N/A	0.5 V	54 W h kg <sup>-1</sup>	40 mA h g <sup>-1</sup> after 10 cycles	108
α-MoO <sub>3</sub>	AlCl <sub>3</sub> : [EMIm]Cl molar ratio 1.1 : 1	100 mA h g <sup>-1</sup> at 3 mA g <sup>-1</sup>	0.9 V	90 W h kg <sup>-1</sup>	12.5 mA h g <sup>-1</sup> after 25 cycles at 10 mA g <sup>-1</sup>	214
TiS <sub>2</sub>	AlCl <sub>3</sub> : [BMIm]Cl molar ratio 1.5 : 1	70 mA h g <sup>-1</sup> at 5 mA g <sup>-1</sup> (50 °C)	0.75 V	53 W h kg <sup>-1</sup>	70 mA h g <sup>-1</sup> after 50 cycles at 5 mA g <sup>-1</sup> (50 °C)	106
TiS <sub>2</sub> NB	AlCl <sub>3</sub> : [EMIm]Cl molar ratio 1.5 : 1	200 mA h g <sup>-1</sup> at 240 mA g <sup>-1</sup> (at 50 °C)	0.4 V	80 W h kg <sup>-1</sup>	150 mA h g <sup>-1</sup> after 90 cycles at 240 mA g <sup>-1</sup>	161
Graphene-VS <sub>2</sub> NS	AlCl <sub>3</sub> : [EMIm]Cl molar ratio 1.3 : 1	186 mA h g <sup>-1</sup> at 100 mA g <sup>-1</sup>	0.6 V	112 W h kg <sup>-1</sup>	50 mA h g <sup>-1</sup> after 50 cycles at 100 mA g <sup>-1</sup>	171
VSe <sub>2</sub>	AlCl <sub>3</sub> : [EMIm]Cl	419 mA h g <sup>-1</sup> at 100 mA g <sup>-1</sup>	1.2 V	503 W h kg <sup>-1</sup>	50 mA h g <sup>-1</sup> after 100 cycles at 100 mA g <sup>-1</sup>	172
MoS <sub>2</sub> microspheres	AlCl <sub>3</sub> : [EMIm]Cl molar ratio 1.3 : 1	253.6 mA h g <sup>-1</sup> at 20 mA g <sup>-1</sup>	0.6 V	152 W h kg <sup>-1</sup>	66.7 mA h g <sup>-1</sup> after 100 cycles at 40 mA g <sup>-1</sup>	111
Free-standing MoS <sub>2</sub> /carbon NF	AlCl <sub>3</sub> : [EMIm]Cl molar ratio 1.3 : 1	293.2 mA h g <sup>-1</sup> at 100 mA g <sup>-1</sup>	~0.5 V	~147 W h kg <sup>-1</sup>	127 mA h g <sup>-1</sup> after 200 cycles at 100 mA g <sup>-1</sup>	178
Flower-like MoS <sub>2</sub> microspheres	AlCl <sub>3</sub> : [EMIm]Cl molar ratio 1.3 : 1	154 mA h g <sup>-1</sup> at 50 mA g <sup>-1</sup>	~0.4 V	~61 W h kg <sup>-1</sup>	112 mA h g <sup>-1</sup> after 100 cycles at 50 mA g <sup>-1</sup>	179
Carbon paper	AlCl <sub>3</sub> : [EMIm]Cl molar ratio 1.3 : 1	90 mA h g <sup>-1</sup> at 50 mA g <sup>-1</sup>	1.8 V	162 W h kg <sup>-1</sup>	70 mA h g <sup>-1</sup> after 100 cycles at 100 mA g <sup>-1</sup>	215
Graphitic foam	AlCl <sub>3</sub> : [EMIm]Cl molar ratio 1.3 : 1	60 mA h g <sup>-1</sup> at 5 A g <sup>-1</sup>	1.8 V	108 W h kg <sup>-1</sup>	60 mA h g <sup>-1</sup> after 7500 cycles at 4 A g <sup>-1</sup>	21
Aligned graphene sheets	AlCl <sub>3</sub> : [EMIm]Cl molar ratio 1.3 : 1	60 mA h g <sup>-1</sup> at 12 A g <sup>-1</sup>	1.8 V	108 W h kg <sup>-1</sup>	60 mA h g <sup>-1</sup> after 4000 cycles at 12 A g <sup>-1</sup>	112
Few-layer graphene	AlCl <sub>3</sub> : [EMIm]Cl molar ratio 1.3 : 1	110 mA h g <sup>-1</sup> at 100 mA g <sup>-1</sup>	2 V	220 W h kg <sup>-1</sup>	75 mA h g <sup>-1</sup> after 1000 cycles at 3 A g <sup>-1</sup>	216
Natural graphite	AlCl <sub>3</sub> : [EMIm]Cl molar ratio 1.3 : 1	132 mA h g <sup>-1</sup> at 100 mA g <sup>-1</sup>	2 V	264 W h kg <sup>-1</sup>	132 mA h g <sup>-1</sup> after 100 cycles at 100 mA g <sup>-1</sup>	217
Graphite powder	AlCl <sub>3</sub> : urea molar ratio 1.3 : 1	73 mA h g <sup>-1</sup> at 100 mA g <sup>-1</sup>	1.73 V	126 W h kg <sup>-1</sup>	~73 mA h g <sup>-1</sup> after 200 cycles at 100 mA g <sup>-1</sup>	105
Natural graphite	AlCl <sub>3</sub> : [EMIm]Cl molar ratio 1.3 : 1	110 mA h g <sup>-1</sup> at 99 mA g <sup>-1</sup>	~1.9 V	209 W h kg <sup>-1</sup>	60 mA h g <sup>-1</sup> after 6000 cycles at 600 mA g <sup>-1</sup>	113
Large-size few-layer graphene	AlCl <sub>3</sub> : [PMIm]Cl molar ratio 1.3 : 1	85 mA h g <sup>-1</sup> at 60 mA g <sup>-1</sup>	1.8 V	153 W h kg <sup>-1</sup>	80 mA h g <sup>-1</sup> after 200 cycles at 60 mA g <sup>-1</sup>	184
Carbon nanoscrolls	AlCl <sub>3</sub> : [EMIm]Cl molar ratio 1.3 : 1	104 mA h g <sup>-1</sup> at 1 A g <sup>-1</sup>	1.5 V	156 W h kg <sup>-1</sup>	101 mA h g <sup>-1</sup> after 55 000 cycles at 50 A g <sup>-1</sup>	218
Graphite powder	AlCl <sub>3</sub> : [EMIm]Cl molar ratio 1.7 : 1	~110 mA h g <sup>-1</sup> at 50 mA g <sup>-1</sup> (at -10 °C)	~2 V (-10 °C)	~220 W h kg <sup>-1</sup> (at -10 °C)	85 mA h g <sup>-1</sup> after 1200 cycles at 100 mA g <sup>-1</sup> (-20 °C)	219
Edge-rich graphene	AlCl <sub>3</sub> : [EMIm]Cl molar ratio 1.3 : 1	128 mA h g <sup>-1</sup> at 2 A g <sup>-1</sup>	1.8 V	230 W h kg <sup>-1</sup>	90 mA h g <sup>-1</sup> after 20 000 cycles at 8 A g <sup>-1</sup>	220
Graphene aerogel	AlCl <sub>3</sub> /Et <sub>3</sub> NHCl molar ratio 1.5 : 1	112 mA h g <sup>-1</sup> at 5 A g <sup>-1</sup>	~1.7 V	190 W h kg <sup>-1</sup>	109 mA h g <sup>-1</sup> after 30 000 cycles at 5 A g <sup>-1</sup>	188
Edge-rich graphitic nanoribbons	AlCl <sub>3</sub> : [EMIm]Cl molar ratio 1.3 : 1	126 mA h g <sup>-1</sup> at 1 A g <sup>-1</sup>	1.91 V	241 W h kg <sup>-1</sup>	105 mA h g <sup>-1</sup> after 20 000 cycles at 10 A g <sup>-1</sup>	186
Surface-perforated graphene	AlCl <sub>3</sub> : [EMIm]Cl molar ratio 1.3 : 1	197 mA h g <sup>-1</sup> at 2 A g <sup>-1</sup>	~1.75 V	~345 W h kg <sup>-1</sup>	147 mA h g <sup>-1</sup> after 1000 cycles at 5 A g <sup>-1</sup>	187
TpBpy-COF	AlCl <sub>3</sub> : [EMIm]Cl molar ratio 1.3 : 1	307 mA h g <sup>-1</sup> at 100 mA g <sup>-1</sup>	~1.15 V	~353 W h kg <sup>-1</sup>	150 mA h g <sup>-1</sup> after 13 000 cycles at 2 A g <sup>-1</sup>	210

<sup>a</sup> NFs – nanofibers, TMS – tetramethylene sulfone, NW – nanowire, AC – active carbon, NB – nanobelts, NS – nanosheet, NR – nanorod, BMIM – 1-butyl-3-methylimidazolium, PMIM – 1-methyl-3-propylimidazolium chlorides, TpBpy – 1,3,5-triformylphloroglucinol + 2,2'-bipyridine-5,5'-diamine.

incorporation would bring the extraction of molecules (e.g., water) into the electrolyte, inducing the formation of the passivation layer on metal anodes. The incorporated molecules

would also induce the partial reduction of active sites, thus lessening the theoretical specific capacity. Moreover, interlayer expansion strategies would also lead to low discharge voltages



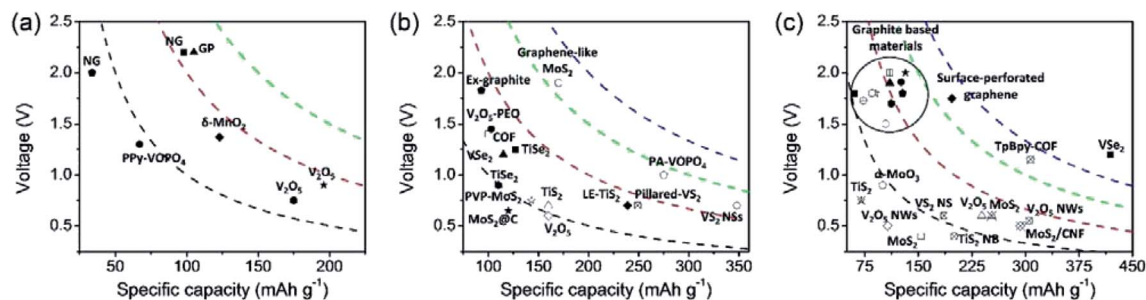


Fig. 29 Average discharge voltage vs. specific capacity of recently developed layered cathodes for (a) ZMBs,<sup>23,24,59,61,65,66,183</sup> (b) MMBs,<sup>80,136,141,153,154,157,158,160,167,174,176,177,208,212</sup> and (c) AMBs.<sup>21,105,106,108,111–113,143,161,171,172,178,179,184,186–188,210,213–220</sup> The black (100 mA h g<sup>-1</sup>), red (200 mA h g<sup>-1</sup>), green (300 mA h g<sup>-1</sup>), and blue (400 mA h g<sup>-1</sup>) dash lines correspond to energy density at the same values.

compared with the theoretical values for pristine materials. New material structure engineering strategies at the molecule level are highly desired. In this sense, many approaches, which have been well demonstrated in alkali metal ion batteries (*e.g.*, defect engineering, artifice electrode/electrolyte interface construction), could be considered in future researches.

The sluggish charge-storage kinetics of MVMB cathodes associated with the multivalent metal ions as charge carriers represents one of the dominant factors restricting the performance. To this end, employing anion-storage cathodes (*e.g.*, graphite and p-type organic redox compounds) for MVMBs represents a feasible way to avoid the kinetics issue, because the low-charge-density anion-storage (*e.g.*, PF<sub>6</sub><sup>-</sup>, TFSI<sup>-</sup>, and AlCl<sub>4</sub><sup>-</sup>) chemistry allows cathode with high rate capability and high redox potentials. Anion-storage chemistries have been extensively explored in AMBs and preliminarily demonstrated in ZMBs. More future efforts are desired to further expand anion-storage chemistries to more MVMB devices, which will require the development of high-capacity anion-storage sites and wide-potential-window electrolytes. Besides, rationally constructing 2D COFs with dense p-type organic redox groups could be an effective approach to obtain superior anion-storage cathodes.

Furthermore, the dominant motivation to develop MVMBs comes from the advantages brought by the direct use of multivalent metal anodes (*e.g.*, superior volumetric capacity and dendrite-free stripping/plating). However, in many studies, the developed cathodes were evaluated in electrolytes that are incompatible with the metal anode chemistry (*e.g.*, the Mg(ClO<sub>4</sub>)<sub>2</sub> in AN electrolyte for MMBs). In this regard, the acquired electrochemical data would not be the suitable reference for assembling MVMBs. In addition, various device parameters (*e.g.*, mass loading, electrode preparation method, and electrolyte) for the performance assessment of cathodes could significantly affect the electrochemical performance. Therefore, the comparison between cathodes evaluated in different device systems is somehow unjustified. Additionally, the cathode analysis focused primarily on the specific capacity and rate capability. Important parameters, such as energy density, energy efficiency, and power density, are often overlooked. Especially, in some cases, the specific capacities were measured at very low voltages, resulting in the negligible contribution to the energy. Therefore, it is essential for the

community to push forwards the standardization of electrode evaluation for MVMBs, which take under consideration the important parameters measured at agreed conditions.

Although the research on MVMBs is still at the primary research stage, commercialization is always the ultimate goal for new battery chemistries. Thus, we summarize some promising research directions of non-aqueous MVMBs in views of practical application as below. Zn metal stability in aqueous electrolytes is restricted by the severe dendrite growth, thus motivating the development of non-aqueous ZMBs with reversible and efficient anode electrochemistry. However, the intercalation kinetics of Zn<sup>2+</sup> into layered TMO cathodes is sluggish in non-aqueous electrolytes. Learned from aqueous ZMBs, trace water additive holds the promise to greatly improve the performance of TMO cathodes for non-aqueous ZMBs. In this sense, additional efforts are required to explore the effect of the water additive on the Zn anode and fine-tune the amount of the water additive in organic solvents. As Mg has the lowest stripping/plating potential among the presented multivalent metals, it has great potential for constructing batteries with high energy and power densities. Among the possible cathode materials for MMBs, TMOs exhibit the most promising performance with large theoretical capacities, high redox potentials, and thus large theoretical energy densities. In addition, the demonstration of effective Mg<sup>2+</sup> intercalation into TMOs and decent cyclability imply their potential as promising cathodes for MMBs. However, before the implementation of TMOs-based MMB devices can be made, considerable efforts should be devoted to developing compatible electrolytes for both the TMO cathodes and the Mg metal anode. Unlike TMOs, TMDs are fully compatible with currently developed Mg electrolytes. Nevertheless, large amounts of their capacities are at the low operation voltage range (<0.5 V), which is not feasible for practical applications. For AMBs, the intercalation of Al<sup>3+</sup> causes the fast capacity degradation of most layered cathodes. Recent studies suggest other Al species, such as AlCl<sub>2</sub><sup>+</sup>, AlCl<sub>2</sub><sup>2+</sup>, and AlCl<sub>4</sub><sup>-</sup>, to be promising charge carriers for AMB cathodes. In this regard, carbon-based/carbon-rich materials, such as graphite, 2D COFs, and 2D conjugated metal-organic frameworks, are considered as the potential alternative cathodes for AMBs, as they enable new electrochemistries, high specific capacities, long-term

cyclability, and high operation voltage that other layered materials are lacking (e.g., TMOs and TMDs).

Finally, the assessment of the cathode performance alone could not promote the transition from research to practical application. Most reported studies focus only on evaluating cathodes with flood electrolytes and much over-capacity metal anodes, and the full-device demonstration for MVMBs is often missing in previous studies. When assembling full devices, the anode–electrolyte–cathode ratios could have a prominent effect on the performance. In addition, some MVMB electrolytes (e.g., APC for MMBs and  $\text{AlCl}_3/\text{EMIMCl}$  for AMBs) used in previous studies are not compatible with the commonly used current collectors (e.g., Al, Cu, and stainless steel) due to the strong corrosive effect. In this sense, the fabrication of promising cathodes should go side-by-side with the development of suitable electrolytes. Furthermore, effort should also be directed to the development of simple procedures for cathodes material synthesis. Since most pristine layered materials display inefficient multivalent metal ion storage, post structure engineering (e.g., layer expansion) is commonly required to promote the ion-storage kinetics. However, such structure engineering steps could hinder their commercialization due to the high material processing cost.

## Conflicts of interest

There are no conflicts to declare.

## Acknowledgements

This work was financially supported by European Union's Horizon 2020 research and innovation programme (GrapheneCore3 881603), M-ERA.NET and Sächsisches Staatsministerium für Wissenschaft und Kunst (HYSUCAP 100478697), German Research Foundation (DFG) within the Cluster of Excellence, CRC 1415 (grant no. 417590517), and Polymer-based Batteries (SPP 2248, RACOF-MMIS). The authors appreciate the helpful discussion with Prof. Xinliang Feng at TU Dresden.

## References

- 1 S. C. Pryor and R. J. Barthelme, *Nat. Energy*, 2021, **6**, 268–276.
- 2 C. Mitchell, *Nat. Energy*, 2016, **1**, 15030.
- 3 M. Yu and X. Feng, *Joule*, 2019, **3**, 338–360.
- 4 P. Zhang, F. Wang, S. Yang, G. Wang, M. Yu and X. Feng, *Energy Storage Mater.*, 2020, **28**, 160–187.
- 5 M. Wang, R. Dong and X. Feng, *Chem. Soc. Rev.*, 2021, **50**, 2764–2793.
- 6 J. Jaguemont, L. Boulon and Y. Dubé, *Appl. Energy*, 2016, **164**, 99–114.
- 7 Y. Wang, B. Liu, Q. Li, S. Cartmell, S. Ferrara, Z. D. Deng and J. Xiao, *J. Power Sources*, 2015, **286**, 330–345.
- 8 J. Muldoon, C. B. Bucur and T. Gregory, *Chem. Rev.*, 2014, **114**, 11683–11720.
- 9 M. Mao, T. Gao, S. Hou and C. Wang, *Chem. Soc. Rev.*, 2018, **47**, 8804–8841.
- 10 M. M. Huie, D. C. Bock, E. S. Takeuchi, A. C. Marschilok and K. J. Takeuchi, *Coord. Chem. Rev.*, 2015, **287**, 15–27.
- 11 A. Ponrouch, J. Bitenc, R. Dominko, N. Lindahl, P. Johansson and M. R. Palacin, *Energy Storage Mater.*, 2019, **20**, 253–262.
- 12 J. Xie and Q. Zhang, *Small*, 2019, **15**, 1805061.
- 13 R. Dominko, J. Bitenc, R. Berthelot, M. Gauthier, G. Pagot and V. Di Noto, *J. Power Sources*, 2020, **478**, 229027.
- 14 H. Li, L. Ma, C. Han, Z. Wang, Z. Liu, Z. Tang and C. Zhi, *Nano Energy*, 2019, **62**, 550–587.
- 15 A. Ponrouch, J. Bitenc, R. Dominko, N. Lindahl, P. Johansson and M. R. R. Palacin, *Energy Storage Mater.*, 2019, **20**, 253–262.
- 16 Z. Hu, H. Zhang, H. Wang, F. Zhang, Q. Li and H. Li, *ACS Mater. Lett.*, 2020, **2**, 887–904.
- 17 Y. Liu, G. He, H. Jiang, I. P. Parkin, P. R. Shearing and D. J. L. Brett, *Adv. Funct. Mater.*, 2021, **31**, 2010445.
- 18 C. Wu, H. Tan, W. Huang, C. Liu, W. Wei, L. Chen and Q. Yan, *Mater. Today Energy*, 2021, **19**, 100595.
- 19 T. Watkins, A. Kumar and D. A. Buttry, *J. Am. Chem. Soc.*, 2016, **138**, 641–650.
- 20 H. Dong, O. Tutusaus, Y. Liang, Y. Zhang, Z. Lebens-Higgins, W. Yang, R. Mohtadi and Y. Yao, *Nat. Energy*, 2020, **5**, 1043–1050.
- 21 M. C. Lin, M. Gong, B. Lu, Y. Wu, D. Y. Wang, M. Guan, M. Angell, C. Chen, J. Yang, B. J. Hwang and H. Dai, *Nature*, 2015, **520**, 324–328.
- 22 J. Zheng, D. C. Bock, T. Tang, Q. Zhao, J. Yin, K. R. Tallman, G. Wheeler, X. Liu, Y. Deng, S. Jin, A. C. Marschilok, E. S. Takeuchi, K. J. Takeuchi and L. A. Archer, *Nat. Energy*, 2021, **6**, 398–406.
- 23 Y. Wang, L. Zhang, F. Zhang, X. Ding, K. Shin and Y. Tang, *J. Energy Chem.*, 2021, **58**, 602–609.
- 24 G. Wang, B. Kohn, U. Scheler, F. Wang, S. Oswald, M. Löffler, D. Tan, P. Zhang, J. Zhang and X. Feng, *Adv. Mater.*, 2020, **32**, 1905681.
- 25 W. Chen, X. Zhan, B. Luo, Z. Ou, P. C. Shih, L. Yao, S. Pidaparthy, A. Patra, H. An, P. V. Braun, R. M. Stephens, H. Yang, J.-M. Zuo and Q. Chen, *Nano Lett.*, 2019, **19**, 4712–4720.
- 26 R. D. Bayliss, B. Key, G. Sai Gautam, P. Canepa, B. J. Kwon, S. H. Lapidus, F. Dogan, A. A. Adil, A. S. Lipton, P. J. Baker, G. Ceder, J. T. Vaughey and J. Cabana, *Chem. Mater.*, 2020, **32**, 663–670.
- 27 C. Kim, P. J. Phillips, B. Key, T. Yi, D. Nordlund, Y. S. Yu, R. D. Bayliss, S. D. Han, M. He, Z. Zhang, A. K. Burrell, R. F. Klie and J. Cabana, *Adv. Mater.*, 2015, **27**, 3377–3384.
- 28 Q. D. Truong, M. Kempaiah Devaraju, P. D. Tran, Y. Gambe, K. Nayuki, Y. Sasaki and I. Honma, *Chem. Mater.*, 2017, **29**, 6245–6251.
- 29 T. Koketsu, J. Ma, B. J. Morgan, M. Body, C. Legein, W. Dachraoui, M. Giannini, A. Demortière, M. Salanne, F. Dardoize, H. Groult, O. J. Borkiewicz, K. W. Chapman, P. Strasser and D. Dambournet, *Nat. Mater.*, 2017, **16**, 1142–1148.
- 30 C. Legein, B. J. Morgan, F. Fayon, T. Koketsu, J. Ma, M. Body, V. Sarou-Kanian, X. Wei, M. Heggen,

- O. J. Borkiewicz, P. Strasser and D. Dambournet, *Angew. Chem., Int. Ed.*, 2020, **59**, 19247–19253.
- 31 T. D. Gregory, R. J. Hoffman and R. C. Winterton, *J. Electrochem. Soc.*, 1990, **137**, 775–780.
- 32 K. Kalantar-zadeh, J. Z. Ou, T. Daeneke, A. Mitchell, T. Sasaki and M. S. Fuhrer, *Appl. Mater. Today*, 2016, **5**, 73–89.
- 33 G. Fiori, F. Bonaccorso, G. Iannaccone, T. Palacios, D. Neumaier, A. Seabaugh, S. K. Banerjee and L. Colombo, *Nat. Nanotechnol.*, 2014, **9**, 768–779.
- 34 A. B. Kaul, *J. Mater. Res.*, 2014, **29**, 348–361.
- 35 D. L. Duong, S. J. Yun and Y. H. Lee, *ACS Nano*, 2017, **11**, 11803–11830.
- 36 A. Manthiram, *ACS Cent. Sci.*, 2017, **3**, 1063–1069.
- 37 C. Liu, Z. G. Neale and G. Cao, *Mater. Today*, 2016, **19**, 109–123.
- 38 F. Wei, Q. Zhang, P. Zhang, W. Tian, K. Dai, L. Zhang, J. Mao and G. Shao, *J. Electrochem. Soc.*, 2021, **168**, 050524.
- 39 Y. Xiao, N. M. Abbasi, Y. Zhu, S. Li, S. Tan, W. Ling, L. Peng, T. Yang, L. Wang, X. Guo, Y. Yin, H. Zhang and Y. Guo, *Adv. Funct. Mater.*, 2020, **30**, 2001334.
- 40 Q. Liu, Z. Hu, M. Chen, C. Zou, H. Jin, S. Wang, S. Chou, Y. Liu and S. Dou, *Adv. Funct. Mater.*, 2020, **30**, 1909530.
- 41 B. Chen, D. Chao, E. Liu, M. Jaroniec, N. Zhao and S. Z. Qiao, *Energy Environ. Sci.*, 2020, **13**, 1096–1131.
- 42 W. S. V. Lee, T. Xiong, X. Wang and J. Xue, *Small Methods*, 2021, **5**, 2000815.
- 43 S. Manzeli, D. Ovchinnikov, D. Pasquier, O. V. Yazyev and A. Kis, *Nat. Rev. Mater.*, 2017, **2**, 17033.
- 44 G. Wang, M. Yu and X. Feng, *Chem. Soc. Rev.*, 2021, **50**, 2388–2443.
- 45 Y. Li, Y. Lu, P. Adelhelm, M. M. Titirici and Y. S. Hu, *Chem. Soc. Rev.*, 2019, **48**, 4655–4687.
- 46 M. Yu, R. Dong and X. Feng, *J. Am. Chem. Soc.*, 2020, **142**, 12903–12915.
- 47 Y. Cao, Y. Lin, J. Wu, X. Huang, Z. Pei, J. Zhou and G. Wang, *ChemSusChem*, 2020, **13**, 1392–1408.
- 48 Y. Shen, Y. Wang, Y. Miao, M. Yang, X. Zhao and X. Shen, *Adv. Mater.*, 2020, **32**, 1905524.
- 49 Y. Liang, H. Dong, D. Aurbach and Y. Yao, *Nat. Energy*, 2020, **5**, 646–656.
- 50 T. Placke, A. Heckmann, R. Schmuck, P. Meister, K. Beltrop and M. Winter, *Joule*, 2018, **2**, 2528–2550.
- 51 Z. Yi, G. Chen, F. Hou, L. Wang and J. Liang, *Adv. Energy Mater.*, 2021, **11**, 2003065.
- 52 B. Tang, L. Shan, S. Liang and J. Zhou, *Energy Environ. Sci.*, 2019, **12**, 3288–3304.
- 53 M. Song, H. Tan, D. Chao and H. J. Fan, *Adv. Funct. Mater.*, 2018, **28**, 1802564.
- 54 D. Selvakumaran, A. Pan, S. Liang and G. Cao, *J. Mater. Chem. A*, 2019, **7**, 18209–18236.
- 55 S. Huang, J. Zhu, J. Tian and Z. Niu, *Chem.–Eur. J.*, 2019, **25**, 14480–14494.
- 56 N. Zhang, X. Chen, M. Yu, Z. Niu, F. Cheng and J. Chen, *Chem. Soc. Rev.*, 2020, **49**, 4203–4219.
- 57 P. Yu, Y. Zeng, H. Zhang, M. Yu, Y. Tong and X. Lu, *Small*, 2019, **15**, 1804760.
- 58 H. Pan, Y. Shao, P. Yan, Y. Cheng, K. S. Han, Z. Nie, C. Wang, J. Yang, X. Li, P. Bhattacharya, K. T. Mueller and J. Liu, *Nat. Energy*, 2016, **1**, 16039.
- 59 V. Verma, S. Kumar, W. Manalastas, J. Zhao, R. Chua, S. Meng, P. Kidkhunthod and M. Srinivasan, *ACS Appl. Energy Mater.*, 2019, **2**, 8667–8674.
- 60 Q. Yang, Q. Li, Z. Liu, D. Wang, Y. Guo, X. Li, Y. Tang, H. Li, B. Dong and C. Zhi, *Adv. Mater.*, 2020, **32**, 2001854.
- 61 D. Kundu, S. Hosseini Vajargah, L. Wan, B. Adams, D. Prendergast and L. F. Nazar, *Energy Environ. Sci.*, 2018, **11**, 881–892.
- 62 C. Pan, R. Zhang, R. G. Nuzzo and A. A. Gewirth, *Adv. Energy Mater.*, 2018, **8**, 1800589.
- 63 A. Guerfi, J. Trottier, I. Boyano, I. De Meatza, J. A. Blazquez, S. Brewer, K. S. Ryder, A. Vijh and K. Zaghbi, *J. Power Sources*, 2014, **248**, 1099–1104.
- 64 S. D. Han, N. N. Rajput, X. Qu, B. Pan, M. He, M. S. Ferrandon, C. Liao, K. A. Persson and A. K. Burrell, *ACS Appl. Mater. Interfaces*, 2016, **8**, 3021–3031.
- 65 P. Senguttuvan, S. D. Han, S. Kim, A. L. Lipson, S. Tepavcevic, T. T. Fister, I. D. Bloom, A. K. Burrell and C. S. Johnson, *Adv. Energy Mater.*, 2016, **6**, 1600826.
- 66 S. D. Han, S. Kim, D. Li, V. Petkov, H. D. Yoo, P. J. Phillips, H. Wang, J. J. Kim, K. L. More, B. Key, R. F. Klie, J. Cabana, V. R. Stamenkovic, T. T. Fister, N. M. Markovic, A. K. Burrell, S. Tepavcevic and J. T. Vaughan, *Chem. Mater.*, 2017, **29**, 4874–4884.
- 67 Z. Chen, F. Mo, T. Wang, Q. Yang, Z. Huang, D. Wang, G. Liang, A. Chen, Q. Li, Y. Guo, X. Li, J. Fan and C. Zhi, *Energy Environ. Sci.*, 2021, **14**, 2441–2450.
- 68 B. Ji, W. Yao and Y. Tang, *Sustainable Energy Fuels*, 2020, **4**, 101–107.
- 69 M. J. Park and A. Manthiram, *ACS Appl. Energy Mater.*, 2020, **3**, 5015–5023.
- 70 Z. Lu, A. Schechter, M. Moshkovich and D. Aurbach, *J. Electroanal. Chem.*, 1999, **466**, 203–217.
- 71 L. W. Gaddum and H. E. French, *J. Am. Chem. Soc.*, 1927, **49**, 1295–1299.
- 72 C. Liebenow, *J. Appl. Electrochem.*, 1997, **27**, 221–225.
- 73 T. D. Gregory, R. J. Hoffman and R. C. Winterton, *J. Electrochem. Soc.*, 1990, **137**, 775–780.
- 74 D. Aurbach, Z. Lu, A. Schechter, Y. Gofer, H. Gizbar, R. Turgeman, Y. Cohen, M. Moshkovich and E. Levi, *Nature*, 2000, **407**, 724–727.
- 75 S. Sakamoto, T. Imamoto and K. Yamaguchi, *Org. Lett.*, 2001, **3**, 1793–1795.
- 76 H. S. Kim, T. S. Arthur, G. D. Allred, J. Zajicek, J. G. Newman, A. E. Rodnyansky, A. G. Oliver, W. C. Boggess and J. Muldoon, *Nat. Commun.*, 2011, **2**, 427.
- 77 A. K. Lautar, J. Bitenc, R. Dominko and J. S. Filhol, *ACS Appl. Mater. Interfaces*, 2021, **13**, 8263–8273.
- 78 Z. Zhao-Karger, J. E. Mueller, X. Zhao, O. Fuhr, T. Jacob and M. Fichtner, *RSC Adv.*, 2014, **4**, 26924–26927.
- 79 N. Pour, Y. Gofer, D. T. Major and D. Aurbach, *J. Am. Chem. Soc.*, 2011, **133**, 6270–6278.
- 80 Y. Zhao, D. Wang, D. Yang, L. Wei, B. Liu, X. Wang, G. Chen and Y. Wei, *Energy Storage Mater.*, 2019, **23**, 749–756.



- 81 R. E. Doe, R. Han, J. Hwang, A. J. Gmitter, I. Shterenberg, H. D. Yoo, N. Pour and D. Aurbach, *Chem. Commun.*, 2014, **50**, 243–245.
- 82 S. He, J. Luo and T. L. Liu, *J. Mater. Chem. A*, 2017, **5**, 12718–12722.
- 83 T. Liu, Y. Shao, G. Li, M. Gu, J. Hu, S. Xu, Z. Nie, X. Chen, C. Wang and J. Liu, *J. Mater. Chem. A*, 2014, **2**, 3430–3438.
- 84 G. Bieker, M. Salama, M. Kolek, Y. Gofer, P. Bieker, D. Aurbach and M. Winter, *ACS Appl. Mater. Interfaces*, 2019, **11**, 24057–24066.
- 85 S. J. Kang, H. Kim, S. Hwang, M. Jo, M. Jang, C. Park, S. T. Hong and H. Lee, *ACS Appl. Mater. Interfaces*, 2019, **11**, 517–524.
- 86 Y. He, Q. Li, L. Yang, C. Yang and D. Xu, *Angew. Chem., Int. Ed.*, 2019, **58**, 7615–7619.
- 87 J. Bitenc, K. Pirnat, E. Žagar, A. Randon-Vitanova and R. Dominko, *J. Power Sources*, 2019, **430**, 90–94.
- 88 C. Liao, N. Sa, B. Key, A. K. Burrell, L. Cheng, L. A. Curtiss, J. T. Vaughey, J. J. Woo, L. Hu, B. Pan and Z. Zhang, *J. Mater. Chem. A*, 2015, **3**, 6082–6087.
- 89 J. Luo, Y. Bi, L. Zhang, X. Zhang and T. L. Liu, *Angew. Chem., Int. Ed.*, 2019, **58**, 6967–6971.
- 90 R. Mohtadi, M. Matsui, T. S. Arthur and S. J. Hwang, *Angew. Chem., Int. Ed.*, 2012, **51**, 9780–9783.
- 91 O. Tutusaus, R. Mohtadi, T. S. Arthur, F. Mizuno, E. G. Nelson and Y. V. Sevryugina, *Angew. Chem., Int. Ed.*, 2015, **54**, 7900–7904.
- 92 L. F. Wan, B. R. Perdue, C. A. Appleby and D. Prendergast, *Chem. Mater.*, 2015, **27**, 5932–5940.
- 93 H. D. Yoo, J. R. Jokisaari, Y. S. Yu, B. J. Kwon, L. Hu, S. Kim, S. D. Han, M. Lopez, S. H. Lapidus, G. M. Nolis, B. J. Ingram, I. Bolotin, S. Ahmed, R. F. Klie, J. T. Vaughey, T. T. Fister and J. Cabana, *ACS Energy Lett.*, 2019, **4**, 1528–1534.
- 94 L. Hu, J. R. Jokisaari, B. J. Kwon, L. Yin, S. Kim, H. Park, S. H. Lapidus, R. F. Klie, B. Key, P. Zapol, B. J. Ingram, J. T. Vaughey and J. Cabana, *ACS Energy Lett.*, 2020, **5**, 2721–2727.
- 95 X. Sun, V. Duffort, B. L. Mehdi, N. D. Browning and L. F. Nazar, *Chem. Mater.*, 2016, **28**, 534–542.
- 96 B. J. Kwon, L. Yin, H. Park, P. Parajuli, K. Kumar, S. Kim, M. Yang, M. Murphy, P. Zapol, C. Liao, T. T. Fister, R. F. Klie, J. Cabana, J. T. Vaughey, S. H. Lapidus and B. Key, *Chem. Mater.*, 2020, **32**, 6577–6587.
- 97 H. Yang, H. Li, J. Li, Z. Sun, K. He, H. M. Cheng and F. Li, *Angew. Chem., Int. Ed.*, 2019, **58**, 11978–11996.
- 98 L. D. Reed, A. Arteaga and E. J. Menke, *J. Phys. Chem. B*, 2015, **119**, 12677–12681.
- 99 T. J. Melton, J. Joyce, J. T. Maloy, J. A. Boon and J. S. Wilkes, *J. Electrochem. Soc.*, 1990, **137**, 3865–3869.
- 100 M. Jafarian, M. G. Mahjani, F. Gobal and I. Danaee, *J. Electroanal. Chem.*, 2006, **588**, 190–196.
- 101 P. Rolland and G. Mamantov, *J. Electrochem. Soc.*, 1976, **123**, 1299–1303.
- 102 T. Tsuda, I. Kokubo, M. Kawabata, M. Yamagata, M. Ishikawa, S. Kusumoto, A. Imanishi and S. Kuwabata, *J. Electrochem. Soc.*, 2014, **161**, A908–A914.
- 103 K. V. Kravchyk and M. V. Kovalenko, *Commun. Chem.*, 2020, **3**, 120.
- 104 W. Chu, X. Zhang, J. Wang, S. Zhao, S. Liu and H. Yu, *Energy Storage Mater.*, 2019, **22**, 418–423.
- 105 M. Angell, C. J. Pan, Y. Rong, C. Yuan, M. C. Lin, B. Hwang and H. Dai, *Proc. Natl. Acad. Sci. U. S. A.*, 2017, **114**, 834–839.
- 106 L. Geng, J. P. Scheifers, C. Fu, J. Zhang, B. P. T. Fokwa and J. Guo, *ACS Appl. Mater. Interfaces*, 2017, **9**, 21251–21257.
- 107 Z. Hu, K. Zhi, Q. Li, Z. Zhao, H. Liang, X. Liu, J. Huang, C. Zhang, H. Li and X. Guo, *J. Power Sources*, 2019, **440**, 227147.
- 108 S. Gu, H. Wang, C. Wu, Y. Bai, H. Li and F. Wu, *Energy Storage Mater.*, 2017, **6**, 9–17.
- 109 H. Yang, L. Yin, J. Liang, Z. Sun, Y. Wang, H. Li, K. He, L. Ma, Z. Peng, S. Qiu, C. Sun, H. M. Cheng and F. Li, *Angew. Chem., Int. Ed.*, 2018, **57**, 1898–1902.
- 110 D. J. Kim, D. J. Yoo, M. T. Otle, A. Prokofjevs, C. Pezzato, M. Owczarek, S. J. Lee, J. W. Choi and J. F. Stoddart, *Nat. Energy*, 2019, **4**, 51–59.
- 111 Z. Li, B. Niu, J. Liu, J. Li and F. Kang, *ACS Appl. Mater. Interfaces*, 2018, **10**, 9451–9459.
- 112 Y. Wu, M. Gong, M. C. Lin, C. Yuan, M. Angell, L. Huang, D. Y. Wang, X. Zhang, J. Yang, B. J. Hwang and H. Dai, *Adv. Mater.*, 2016, **28**, 9218–9222.
- 113 D.-Y. Wang, C. Y. Wei, M. C. Lin, C. J. Pan, H. L. Chou, H. A. Chen, M. Gong, Y. Wu, C. Yuan, M. Angell, Y. J. Hsieh, Y. H. Chen, C. Y. Wen, C. W. Chen, B. J. Hwang, C. C. Chen and H. Dai, *Nat. Commun.*, 2017, **8**, 14283.
- 114 M. Mao, C. Luo, T. P. Pollard, S. Hou, T. Gao, X. Fan, C. Cui, J. Yue, Y. Tong, G. Yang, T. Deng, M. Zhang, J. Ma, L. Suo, O. Borodin and C. Wang, *Angew. Chem., Int. Ed.*, 2019, **58**, 17820–17826.
- 115 S. Wang, S. Huang, M. Yao, Y. Zhang and Z. Niu, *Angew. Chem.*, 2020, **132**, 11898–11905.
- 116 Y. Zhang, E. H. Ang, Y. Yang, M. Ye, W. Du and C. C. Li, *Adv. Funct. Mater.*, 2021, **31**, 2007358.
- 117 A. Chakraborty, S. Kunnikuruvan, S. Kumar, B. Markovsky, D. Aurbach, M. Dixit and D. T. Major, *Chem. Mater.*, 2020, **32**, 915–952.
- 118 G. M. Kanyolo, T. Masese, N. Matsubara, C. Y. Chen, J. Rizell, Z. D. Huang, Y. Sassa, M. Månsson, H. Senoh and H. Matsumoto, *Chem. Soc. Rev.*, 2021, **50**, 3990–4030.
- 119 K. Kubota, *Electrochemistry*, 2020, **88**, 507–514.
- 120 J. Zhou, X. Lu and M. Yu, *Mater. Chem. Front.*, 2021, **5**, 2996–3020.
- 121 J. S. Kim, W. S. Chang, R. H. Kim, D. Y. Kim, D. W. Han, K. H. Lee, S. S. Lee and S. G. Doo, *J. Power Sources*, 2015, **273**, 210–215.
- 122 W. Liu, P. Oh, X. Liu, M. J. Lee, W. Cho, S. Chae, Y. Kim and J. Cho, *Angew. Chem., Int. Ed.*, 2015, **54**, 4440–4457.
- 123 S. Komaba, N. Kumagai and S. Chiba, *Electrochim. Acta*, 2000, **46**, 31–37.
- 124 M. H. Alfaruqi, J. Gim, S. Kim, J. Song, D. T. Pham, J. Jo, Z. Xiu, V. Mathew and J. Kim, *Electrochem. Commun.*, 2015, **60**, 121–125.
- 125 J. E. Post, *Proc. Natl. Acad. Sci. U. S. A.*, 1999, **96**, 3447–3454.

- 126 S. Devaraj and N. Munichandraiah, *J. Phys. Chem. C*, 2008, **112**, 4406–4417.
- 127 C. H. Kim, Z. Akase, L. Zhang, A. H. Heuer, A. E. Newman and P. J. Hughes, *J. Solid State Chem.*, 2006, **179**, 753–774.
- 128 J. Song, M. Noked, E. Gillette, J. Duay, G. Rubloff and S. B. Lee, *Phys. Chem. Chem. Phys.*, 2015, **17**, 5256–5264.
- 129 A. Chakrabarti, K. Hermann, R. Druzinic, M. Witko, F. Wagner and M. Petersen, *Phys. Rev. B*, 1999, **59**, 10583–10590.
- 130 M. Hibino, in *Encyclopedia of Electrochemical Power Sources*, Elsevier, 2009, pp. 40–50.
- 131 Q. An, P. Zhang, Q. Wei, L. He, F. Xiong, J. Sheng, Q. Wang and L. Mai, *J. Mater. Chem. A*, 2014, **2**, 3297–3302.
- 132 Q. An, Y. Li, H. Deog Yoo, S. Chen, Q. Ru, L. Mai and Y. Yao, *Nano Energy*, 2015, **18**, 265–272.
- 133 P. Novák and J. Desilvestro, *J. Electrochem. Soc.*, 1993, **140**, 140–144.
- 134 J. Song, L. Wang, Y. Lu, J. Liu, B. Guo, P. Xiao, J.-J. Lee, X.-Q. Yang, G. Henkelman and J. B. Goodenough, *J. Am. Chem. Soc.*, 2015, **137**, 2658–2664.
- 135 Y. Xu, X. Deng, Q. Li, G. Zhang, F. Xiong, S. Tan, Q. Wei, J. Lu, J. Li, Q. An and L. Mai, *Chem*, 2019, **5**, 1194–1209.
- 136 S. Tepavcevic, Y. Liu, D. Zhou, B. Lai, J. Maser, X. Zuo, H. Chan, P. Král, C. S. Johnson, V. Stamenkovic, N. M. Markovic and T. Rajh, *ACS Nano*, 2015, **9**, 8194–8205.
- 137 Y. Zhu, G. Huang, J. Yin, Y. Lei, A. Emwas, X. Yu, O. F. Mohammed and H. N. Alshareef, *Adv. Energy Mater.*, 2020, **10**, 2002128.
- 138 X. Deng, Y. Xu, Q. An, F. Xiong, S. Tan, L. Wu and L. Mai, *J. Mater. Chem. A*, 2019, **7**, 10644–10650.
- 139 R. Sun, X. Ji, C. Luo, S. Hou, P. Hu, X. Pu, L. Cao, L. Mai and C. Wang, *Small*, 2020, **16**, 2000741.
- 140 E. A. Esparcia, M. S. Chae, J. D. Ocon and S. T. Hong, *Chem. Mater.*, 2018, **30**, 3690–3696.
- 141 S. D. Perera, R. B. Archer, C. A. Damin, R. Mendoza-Cruz and C. P. Rhodes, *J. Power Sources*, 2017, **343**, 580–591.
- 142 M. Rastgoo-Deylami, M. S. Chae and S. T. Hong, *Chem. Mater.*, 2018, **30**, 7464–7472.
- 143 N. Jayaprakash, S. K. Das and L. A. Archer, *Chem. Commun.*, 2011, **47**, 12610–12612.
- 144 L. D. Reed and E. Menke, *J. Electrochem. Soc.*, 2013, **160**, A915–A917.
- 145 M. Chiku, H. Takeda, S. Matsumura, E. Higuchi and H. Inoue, *ACS Appl. Mater. Interfaces*, 2015, **7**, 24385–24389.
- 146 L. Beneš, K. Melánová, J. Svoboda and V. Zima, *J. Inclusion Phenom. Macrocyclic Chem.*, 2012, **73**, 33–53.
- 147 R. Gautier, R. Gautier, O. Hernandez, N. Audebrand, T. Bataille, C. Roiland, E. Elkaïm, L. Le Pollès, E. Furet and E. Le Fur, *Dalton Trans.*, 2013, **42**, 8124–8131.
- 148 Y. Fang, Q. Liu, L. Xiao, Y. Rong, Y. Liu, Z. Chen, X. Ai, Y. Cao, H. Yang, J. Xie, C. Sun, X. Zhang, B. Aoun, X. Xing, X. Xiao and Y. Ren, *Chem*, 2018, **4**, 1167–1180.
- 149 G. He, W. H. Kan and A. Manthiram, *Chem. Mater.*, 2016, **28**, 682–688.
- 150 C. Wu, X. Lu, L. Peng, K. Xu, X. Peng, J. Huang, G. Yu and Y. Xie, *Nat. Commun.*, 2013, **4**, 2431.
- 151 F. Wang, W. Sun, Z. Shadike, E. Hu, X. Ji, T. Gao, X. Q. Yang, K. Xu and C. Wang, *Angew. Chem., Int. Ed.*, 2018, **57**, 11978–11981.
- 152 X. Ji, J. Chen, F. Wang, W. Sun, Y. Ruan, L. Miao, J. Jiang and C. Wang, *Nano Lett.*, 2018, **18**, 6441–6448.
- 153 L. Zhou, Q. Liu, Z. Zhang, K. Zhang, F. Xiong, S. Tan, Q. An, Y.-M. Kang, Z. Zhou and L. Mai, *Adv. Mater.*, 2018, **30**, 1801984.
- 154 H. D. Yoo, Y. Liang, H. Dong, J. Lin, H. Wang, Y. Liu, L. Ma, T. Wu, Y. Li, Q. Ru, Y. Jing, Q. An, W. Zhou, J. Guo, J. Lu, S. T. Pantelides, X. Qian and Y. Yao, *Nat. Commun.*, 2017, **8**, 339.
- 155 L. Hu, Z. Wu, C. Lu, F. Ye, Q. Liu and Z. Sun, *Energy Environ. Sci.*, DOI: 10.1039/D1EE01158H.
- 156 S. Niu, J. Cai and G. Wang, *Nano Res.*, 2021, **14**, 1985–2002.
- 157 M. Mao, X. Ji, S. Hou, T. Gao, F. Wang, L. Chen, X. Fan, J. Chen, J. Ma and C. Wang, *Chem. Mater.*, 2019, **31**, 3183–3191.
- 158 Y. Gu, Y. Katsura, T. Yoshino, H. Takagi and K. Taniguchi, *Sci. Rep.*, 2015, **5**, 12486.
- 159 Z. L. Tao, L. N. Xu, X. L. Gou, J. Chen and H. T. Yuan, *Chem. Commun.*, 2004, 2080–2081.
- 160 X. Sun, P. Bonnicksen and L. F. Nazar, *ACS Energy Lett.*, 2016, **1**, 297–301.
- 161 C. G. Hawkins, A. Verma, W. Horbinski, R. Weeks, P. P. Mukherjee and L. Whittaker-Brooks, *ACS Appl. Mater. Interfaces*, 2020, **12**, 21788–21798.
- 162 L. Geng, G. Lv, X. Xing and J. Guo, *Chem. Mater.*, 2015, **27**, 4926–4929.
- 163 Q. Yan, Y. Shen, Y. Miao, M. Wang, M. Yang and X. Zhao, *J. Alloys Compd.*, 2019, **806**, 1109–1115.
- 164 Z. Zhao, Z. Hu, Q. Li, H. Li, X. Zhang, Y. Zhuang, F. Wang and G. Yu, *Nano Today*, 2020, **32**, 100870.
- 165 Y. Jing, Z. Zhou, C. R. Cabrera and Z. Chen, *J. Phys. Chem. C*, 2013, **117**, 25409–25413.
- 166 J. Zhou, L. Wang, M. Yang, J. Wu, F. Chen, W. Huang, N. Han, H. Ye, F. Zhao, Y. Li and Y. Li, *Adv. Mater.*, 2017, **29**, 1702061.
- 167 X. Xue, R. Chen, C. Yan, P. Zhao, Y. Hu, W. Kong, H. Lin, L. Wang and Z. Jin, *Adv. Energy Mater.*, 2019, **9**, 1900145.
- 168 H. Tao, M. Zhou, R. Wang, K. Wang, S. Cheng and K. Jiang, *Adv. Sci.*, 2018, **5**, 1801021.
- 169 L. Zhang, D. Sun, J. Kang, H.-T. Wang, S.-H. Hsieh, W.-F. Pong, H. A. Bechtel, J. Feng, L.-W. Wang, E. J. Cairns and J. Guo, *Nano Lett.*, 2018, **18**, 4506–4515.
- 170 R. Sun, C. Pei, J. Sheng, D. Wang, L. Wu, S. Liu, Q. An and L. Mai, *Energy Storage Mater.*, 2018, **12**, 61–68.
- 171 L. Wu, R. Sun, F. Xiong, C. Pei, K. Han, C. Peng, Y. Fan, W. Yang, Q. An and L. Mai, *Phys. Chem. Chem. Phys.*, 2018, **20**, 22563–22568.
- 172 H. Lei, M. Wang, J. Tu and S. Jiao, *Sustainable Energy Fuels*, 2019, **3**, 2717–2724.
- 173 D. Voiry, A. Goswami, R. Kappera, C. D. C. C. E. Silva, D. Kaplan, T. Fujita, M. Chen, T. Asefa and M. Chhowalla, *Nat. Chem.*, 2015, **7**, 45–49.
- 174 Z. Li, X. Mu, Z. Zhao-Karger, T. Diemant, R. J. Behm, C. Kübel and M. Fichtner, *Nat. Commun.*, 2018, **9**, 5115.

- 175 T. Stephenson, Z. Li, B. Olsen and D. Mitlin, *Energy Environ. Sci.*, 2014, **7**, 209–231.
- 176 Y. Liang, R. Feng, S. Yang, H. Ma, J. Liang and J. Chen, *Adv. Mater.*, 2011, **23**, 640–643.
- 177 C. Wu, G. Zhao, S. Gong, N. Zhang and K. Sun, *J. Mater. Chem. A*, 2019, **7**, 4426–4430.
- 178 W. Yang, H. Lu, Y. Cao, B. Xu, Y. Deng and W. Cai, *ACS Sustainable Chem. Eng.*, 2019, **7**, 4861–4867.
- 179 J. Tu, X. Xiao, M. Wang and S. Jiao, *J. Phys. Chem. C*, 2019, **123**, 26794–26802.
- 180 Z. Zhao, Z. Hu, H. Liang, S. Li, H. Wang, F. Gao, X. Sang and H. Li, *ACS Appl. Mater. Interfaces*, 2019, **11**, 44333–44341.
- 181 X. Zhou, Q. Liu, C. Jiang, B. Ji, X. Ji, Y. Tang and H. M. Cheng, *Angew. Chem., Int. Ed.*, 2020, **59**, 3802–3832.
- 182 G. Schmuelling, T. Placke, R. Kloepsch, O. Fromm, H. W. Meyer, S. Passerini and M. Winter, *J. Power Sources*, 2013, **239**, 563–571.
- 183 J. Fan, Q. Xiao, Y. Fang, L. Li and W. Yuan, *Ionics*, 2019, **25**, 1303–1313.
- 184 L. Zhang, L. Chen, H. Luo, X. Zhou and Z. Liu, *Adv. Energy Mater.*, 2017, **7**, 1700034.
- 185 H. Huang, F. Zhou, X. Shi, J. Qin, Z. Zhang, X. Bao and Z. S. Wu, *Energy Storage Mater.*, 2019, **23**, 664–669.
- 186 Y. Hu, S. Debnath, H. Hu, B. Luo, X. Zhu, S. Wang, M. Hankel, D. J. Searles and L. Wang, *J. Mater. Chem. A*, 2019, **7**, 15123–15130.
- 187 Y. Kong, C. Tang, X. Huang, A. K. Nanjundan, J. Zou, A. Du and C. Yu, *Adv. Funct. Mater.*, 2021, **31**, 2010569.
- 188 H. Xu, T. Bai, H. Chen, F. Guo, J. Xi, T. Huang, S. Cai, X. Chu, J. Ling, W. Gao, Z. Xu and C. Gao, *Energy Storage Mater.*, 2019, **17**, 38–45.
- 189 G. Wang, N. Chandrasekhar, B. P. Biswal, D. Becker, S. Paasch, E. Brunner, M. Addicoat, M. Yu, R. Berger and X. Feng, *Adv. Mater.*, 2019, **31**, 1901478.
- 190 M. Yu, N. Chandrasekhar, R. K. M. Raghupathy, K. H. Ly, H. Zhang, E. Dmitrieva, C. Liang, X. Lu, T. D. Kühne, H. Mirhosseini, I. M. Weidinger and X. Feng, *J. Am. Chem. Soc.*, 2020, **142**, 19570–19578.
- 191 Z. Lei, Q. Yang, Y. Xu, S. Guo, W. Sun, H. Liu, L.-P. Lv, Y. Zhang and Y. Wang, *Nat. Commun.*, 2018, **9**, 576.
- 192 F. Wang, Z. Liu, C. Yang, H. Zhong, G. Nam, P. Zhang, R. Dong, Y. Wu, J. Cho, J. Zhang and X. Feng, *Adv. Mater.*, 2020, **32**, 1905361.
- 193 R. Shi, L. Liu, Y. Lu, C. Wang, Y. Li, L. Li, Z. Yan and J. Chen, *Nat. Commun.*, 2020, **11**, 178.
- 194 B. Pan, J. Huang, Z. Feng, L. Zeng, M. He, L. Zhang, J. T. Vaughey, M. J. Bedzyk, P. Fenter, Z. Zhang, A. K. Burrell and C. Liao, *Adv. Energy Mater.*, 2016, **6**, 1600140.
- 195 A. M. Khayum, M. Ghosh, V. Vijayakumar, A. Halder, M. Nurhuda, S. Kumar, M. Addicoat, S. Kurungot and R. Banerjee, *Chem. Sci.*, 2019, **10**, 8889–8894.
- 196 B. Pan, D. Zhou, J. Huang, L. Zhang, A. K. Burrell, J. T. Vaughey, Z. Zhang and C. Liao, *J. Electrochem. Soc.*, 2016, **163**, A580–A583.
- 197 J. Bitenc, N. Lindahl, A. Vizintin, M. E. Abdelhamid, R. Dominko and P. Johansson, *Energy Storage Mater.*, 2020, **24**, 379–383.
- 198 J. Bitenc, K. Pirnat, E. Žagar, A. Randon-Vitanova and R. Dominko, *J. Power Sources*, 2019, **430**, 90–94.
- 199 J. Bitenc, K. Pirnat, T. Bančič, M. Gaberšček, B. Genorio, A. Randon-Vitanova and R. Dominko, *ChemSusChem*, 2015, **8**, 4128–4132.
- 200 L. Ma, S. Chen, X. Li, A. Chen, B. Dong and C. Zhi, *Angew. Chem.*, 2020, **132**, 24044–24052.
- 201 Q. Wang, Y. Liu and P. Chen, *J. Power Sources*, 2020, **468**, 228401.
- 202 S. Zhang, S. Long, H. Li and Q. Xu, *Chem. Eng. J.*, 2020, **400**, 125898.
- 203 H. Glatz, E. Lizundia, F. Pacifico and D. Kundu, *ACS Appl. Energy Mater.*, 2019, **2**, 1288–1294.
- 204 D. Lu, H. Liu, T. Huang, Z. Xu, L. Ma, P. Yang, P. Qiang, F. Zhang and D. Wu, *J. Mater. Chem. A*, 2018, **6**, 17297–17302.
- 205 F. Guo, Z. Huang, M. Wang, W. L. Song, A. Lv, X. Han, J. Tu and S. Jiao, *Energy Storage Mater.*, 2020, **33**, 250–257.
- 206 Q. Wang, X. Xu, G. Yang, Y. Liu and X. Yao, *Chem. Commun.*, 2020, **56**, 11859–11862.
- 207 W. Wang, V. S. Kale, Z. Cao, S. Kandambeth, W. Zhang, J. Ming, P. T. Parvatkar, E. Abou-Hamad, O. Shekhah, L. Cavallo, M. Eddaoudi and H. N. Alshareef, *ACS Energy Lett.*, 2020, **5**, 2256–2264.
- 208 R. Sun, S. Hou, C. Luo, X. Ji, L. Wang, L. Mai and C. Wang, *Nano Lett.*, 2020, **20**, 3880–3888.
- 209 K. W. Nam, H. Kim, Y. Beldjoudi, T. Kwon, D. J. Kim and J. F. Stoddart, *J. Am. Chem. Soc.*, 2020, **142**, 2541–2548.
- 210 H. Lu, F. Ning, R. Jin, C. Teng, Y. Wang, K. Xi, D. Zhou and G. Xue, *ChemSusChem*, 2020, **13**, 3447–3454.
- 211 B. Ji, H. He, W. Yao and Y. Tang, *Adv. Mater.*, 2021, **33**, 2005501.
- 212 R. Yang, F. Zhang, X. Lei, Y. Zheng, G. Zhao, Y. Tang and C. S. Lee, *ACS Appl. Mater. Interfaces*, 2020, **12**, 47539–47547.
- 213 H. Wang, Y. Bai, S. Chen, X. Luo, C. Wu, F. Wu, J. Lu and K. Amine, *ACS Appl. Mater. Interfaces*, 2015, **7**, 80–84.
- 214 F. Nacimiento, M. Cabello, R. Alcántara, C. Pérez-Vicente, P. Lavela and J. L. Tirado, *J. Electrochem. Soc.*, 2018, **165**, A2994–A2999.
- 215 H. Sun, W. Wang, Z. Yu, Y. Yuan, S. Wang and S. Jiao, *Chem. Commun.*, 2015, **51**, 11892–11895.
- 216 A. S. Childress, P. Parajuli, J. Zhu, R. Podila and A. M. Rao, *Nano Energy*, 2017, **39**, 69–76.
- 217 K. V. Kravchyk, S. Wang, L. Piveteau and M. V. Kovalenko, *Chem. Mater.*, 2017, **29**, 4484–4492.
- 218 Z. Liu, J. Wang, H. Ding, S. Chen, X. Yu and B. Lu, *ACS Nano*, 2018, **12**, 8456–8466.
- 219 C. J. Pan, C. Yuan, G. Zhu, Q. Zhang, C. J. Huang, M. C. Lin, M. Angell, B. J. Hwang, P. Kaghazchi and H. Dai, *Proc. Natl. Acad. Sci. U. S. A.*, 2018, **115**, 5670–5675.
- 220 Q. Zhang, L. Wang, J. Wang, C. Xing, J. Ge, L. Fan, Z. Liu, X. Lu, M. Wu, X. Yu, H. Zhang and B. Lu, *Energy Storage Mater.*, 2018, **15**, 361–367.
- 221 G. Gershinsky, H. D. Yoo, Y. Gofer and D. Aurbach, *Langmuir*, 2013, **29**, 10964–10972.